Title: Analysis of neutral pions from νμ CC CNGS interactions in the ICARUS detector

Author: Izabela Kochanek

Analysis of neutral pions from ν_μ CC CNGS interactions in the ICARUS detector

Izabela Kochanek

Institute of Physics,
University of Silesia

A doctoral dissertation written under supervision
of Professor Jan Kisiel

Katowice, 2015

Abstract

The aim of the thesis is the study of the electromagnetic showers and neutral mesons in the ICARUS T600 Liquid Argon Time Projection Chamber. To accurately reconstruct energy of electromagnetic showers, different corrections to the collected charge are needed. In this thesis the author calibrated the energy reconstruction with a set of corrections, most of which are not present in the official ICARUS reconstruction software. For this goal, the simulation package FLUKA was extensively used in order to study the ionization quenching and the shower containment in the detector. As a result the reconstructed invariant π^0 masses are distributed compactly (σ = 12 MeV/c^2) with a best value equal to 134.5 $\pm$ 1.5 $\pm$ 4.2 MeV/c^2. Moreover, other results on low energy electromagnetic showers in Liquid Argon were found which include the longitudinal profile parametrization, the conversion distance measurement and the ionization losses for 1 and 2 m.i.p. particles. This latest point is interesting for the e^-/γ discrimination which is the key element in the ν_e CC events selection from ν_μ NC background.

Streszczenie

Celem pracy jest analiza kaskad elektromagnetycznych oraz mezonów neutralnych zarejestrowanych w Komorze Projekcji Czasowej detektora ICARUS T600. Aby dokładnie odtworzyć energię kaskad elektromagnetycznych, ładunek zebrany na drutach anodowych wymaga zastosowania pewnych korekcji. W niniejszej pracy, autor skalibrował rekonstrukcję energii wprowadzając zestaw poprawek, z których większość nie jest obecna w oficjalnym oprogramowaniu do rekonstrukcji eksperymentu ICARUS. W tym celu, pakiet symulacji FLUKA został szeroko zastosowany do zbadania osłabienia jonizacji (quenching) oraz zawartości kaskad w objętości czynnej detektora. W efekcie, rozkład zrekonstruowanych mas mezonów neutralnych π^0 jest zwarty (σ = 12 MeV/c^2) ze średnią wartością równą $134.5 \pm 1.5 \pm 4.2$ MeV/c^2. Co więcej, inne wyniki z analizy niskoenergetycznych kaskad elektromagnetycznych w ciekłym argonie zostały opisane, takie jak parametryzacja profilu podłużnego kaskady, pomiar drogi konwersji oraz straty na jonizację dla cząstek 1 i 2 m.i.p. Ten ostatni punkt jest interesujący ze względu na rozróżnianie e^-/γ, które jest kluczowym elementem podczas selekcji zdarzeń ν_e CC od tła pochodzącego od ν_μ NC.

Contents

Chapter 1

Introduction

Neutrino, as a hypothetical particle, was proposed by W. Pauli in 1930 to explain continuous electron spectrum in β decay and spin values of some nuclei. It took more than 20 years to discover electron antineutrino in the reactor neutrino experiment lead by Reines and Cowan [1]. They registered, in a liquid scintillator detector doped with $CdCl_2$, neutrons and positrons produced in the inverse β decay. The existence of second neutrino flavor, the muon neutrino, was established in 1962, in the accelerator neutrino experiment conducted by Lederman, Schwartz and Steinberger [2]. They used a few GeV proton beam reactions with a target leading to copious productions of pions, which decayed into muons and muon neutrinos. Thick iron shielding prevented muons to enter the spark chamber, whereas the rare muon neutrino interactions were observed there. Neutrinos are mainly detected by tracking their charge lepton partners. Therefore, the extremely short lifetime of the tau meson, together with extremely rare tau neutrino production, resulted in a very late tau neutrino discovery in 2001. The DONUT experiment (Fermilab E872), used 800 GeV protons from the Fermilab Tevatron, and identified kinks in the nuclear emulsion, being a signature of tau neutrino interactions, leading to the tau lepton production [3]. Nowadays we have direct evidence for all three neutrino flavors.

Due to the extremely low cross section of neutrino interactions, neutrino experiments are equipped with large active volume detectors working preferably underground, and they use intense neutrino beam or source. Moreover, conclusive results require very long time of data taking. Presently, three liquid based neutrino detection techniques, namely water Cerenkov, liquid scintillator and Liquid Argon Time Projection Chamber (LAr TPC) are used by neutrino experiments. In this thesis, the results obtained with the largest LAr TPC ever built i.e. ICARUS T600 detector, are presented. The muon neutrino

charge current interactions, leading to the production of neutral pions, were recorded during the measurements performed in the Gran Sasso (Italy) underground physics laboratory.

This thesis present the second attempt in the determination of the ICARUS T600 detector capabilities in electromagnetic showers reconstruction. The analysis of 212 hadronic interactions with subsequent production of π^0 mesons, collected during the 2001 Pavia test of the detector on Earth surface, resulted in the resolution of the reconstructed π^0 mass of $\sim$27% [4]. It has to be noticed, that the visual selection of electromagnetic showers in "Earth surface" events was very difficult, due to a crowded environment. Therefore, from the initial sample, events with tracks and interactions in the vicinity of electromagnetic showers, coming from π^0 decay, were removed. For the reduced, "clean" subsample of 97 events, the resolution of $\sim$16% of the reconstructed π^0 mass was found. In the present work, electromagnetic showers were selected from the CNGS ν_μ CC interactions collected by the ICARUS T600 detector, working in the underground Gran Sasso laboratory, what resulted in negligible background to the neutrino interactions. Therefore, the reconstruction of electromagnetic shower shape and energy, allowed for much more detailed studies of their properties.

The background reduction coming from π^0 mesons has essential importance for the future experiments investigating neutrino oscillations. Electrons created during the interactions of ν_e coming from muon neutrino oscillations are signal events

$$\nu_e + n \rightarrow e^- + p, \tag{1.1}$$

while π^0 mesons from NC ν_μ

$$\nu_\mu + n \rightarrow \nu_\mu + \pi^0 + hadrons, \tag{1.2}$$

are background, if π^0 will be misidentified as electron. π^0 produced in NC ν_μ interaction can be misidentified with an electron from CC ν_e interaction when (i) one photon from the decay is lost, when its energy is too small or when it stars showering outside the fiducial volume of the detector, (ii) the two showers overlap.

In a search of $\nu_\mu \rightarrow \nu_\tau$ oscillations, which is very important part of the CNGS program, π^0 meson wrongly identified as electron constitute a background for electrons coming from τ decays. τ leptons are products of ν_τ CC interactions, which in turn are created in ν_μ oscillations. The background reduction in interactions with neutral pions production need efficient algorithms that recognize electrons and π^0 mesons in neutrino interactions.

This thesis is a contribution to e^-/γ discrimination development in liquid argon detectors. The dissertation is also a kind of verification of the ICARUS T600 detector capabilities in e^-/γ discrimination.

The results of this thesis can be also considered in the context of the potential background from photons, with energy greater than 200 MeV, for ν_e searches by the LAr TPC detectors, taking data at very shallow FNAL depths, within the SBN proposal [5]. Photons are generated mainly by cosmic muons and in coincidence with the beam spill or with the data acquisition window, will be a source of background. The main background suppression in the ICARUS T600 detector will be done with the use of an external cosmic ray tagging (CRT) system. However, precise knowledge of photon showers properties implemented in the software tools, should help in additional to the CTR, reduction of gamma background.

The layout of this dissertation is following. The thesis starts with an overview of the ICARUS T600 detector in Chapter 2. The determination of LAr purity and CNGS beam are briefly described. Chapter 3 contains the description of physics program studied with T600 detector, from a search of $\nu_\mu \rightarrow \nu_\tau$ oscillations, through studies of atmospheric and sterile neutrinos, to rare events, as nucleon decay or supernovae neutrinos. In Chapter 4, the interactions of electrons and photons that creates electromagnetic showers, are described. Chapter 5 concerns the analysis and reconstruction tools used in electromagnetic showers and π^0 studies. An example of fully reconstructed CC CNGS event is also shown. Chapters 6 and 7 show the position and angle reconstruction results and describe ladder of corrections for collected energy. Chapter 7 explains the importance of electromagnetic showers containment in the analysis. In Chapter 8, results concerning electromagnetic showers analysis obtained from data collected by ICARUS T600 are shown. Chapter 9 contains analysis of π^0 candidates visually scanned by the author of this thesis from ν_μ CC CNGS events. In the last chapter (Summary and Conclusions), most important results obtained in this thesis are discussed.

The following activities were performed by the author of the thesis:

- participation in data taking in 2011-2013,
- "first scanning" of CNGS events collected by the ICARUS T600 - the goal of this activity was to classify events into specific categories, such as CC/NC neutrino interactions, rock muons, empty events,
- full reconstruction of the CNGS ν_μ beam events: measurement

of incoming neutrino energy, particles identification and three dimensional tracks reconstruction (see section 5.2),

- search for LSND anomaly - scanning of CNGS events for electron neutrino interactions: the search relay on electromagnetic showers starting from the primary vertex [6] and [7],
- scanning for neutrino velocity measurements - as it will be described in chapter 3, an excess of e^+e^- events would mean that neutrinos travel faster than light according to the process analogous to the Cerenkov radiation, no such evidence was found during the scanning,
- analysis of electromagnetic showers and π^0 in LAr and preparation of the data: manual scanning of π^0 candidates.

Chapter 2

The ICARUS T600 detector

The ICARUS T600 is the first large mass (760 tons) example of a new generation of detectors able to combine the imaging capabilities of the old "bubble chamber" with the excellent energy measurement of huge electronic detectors. The idea of Liquid Argon Time Projection Chamber (LAr-TPC) was conceived in 1977 by C.Rubbia [8]. LAr-TPC provide the calorimetric measurement of particle energy, together with 3-dimensional track reconstruction from the electrons drifting in an electric field, in sufficiently pure Liquid Argon. The ICARUS T600 was installed in the Hall B of Gran Sasso Underground Laboratory (LNGS) of Instituto Nazionale di Fisica Nucleare (INFN). The Gran Sasso Mountain with an average thickness of 1400 m of rock above the laboratory halls lead to a reduction of the muon flux, the most penetrating component of the cosmic rays, by a factor of about 10^6 compared with the Earth's surface. It offers thus a low-background environment. The ICARUS T600 addresses a wide physics program. It is simultaneously collecting a wide variety of "self-triggered" events of different nature, such as cosmic ray events and neutrino interactions associated with the CNGS neutrino beam, focusing on neutrino oscillation search.

2.1 Detector description

The ICARUS T600 detector is composed of a large cryostat split into two identical, adjacent half-modules (T300) with internal dimensions $3.6 \times 3.9 \times 19.6$ m^3 filled with about 760 tons of ultra-pure Liquid Argon [9]. Each half-module houses an inner detector made of two TPCs separated by a common cathode, the field-shaping system, monitors and probes, and of a system for the LAr scintillation light detection. The half-modules are externally surrounded by thermal insulation layers. Three parallel wire planes, 3 mm apart, oriented at

different angles ($0°, +60°, -60°$) with respect to the horizontal direction, are placed on the opposite sides of each TPC. By appropriate voltage biasing, the first two planes (Induction1 and Induction2) provide signals in a non-destructive way, whereas the ionization charge is collected by the last one (Collection). This provides three projective views of the same event simultaneously, allowing both spatial reconstruction and precise calorimetric measurement of the collected charges.

Some of the main features of the T600 inner detector are listed in the Table 2.1. A uniform electric field perpendicular to the wires is established in the LAr volume for each half module by means of a HV system. The system is composed of a cathode plane, parallel to the wire planes, placed in the center of each half-module at a distance of about 1.5 m from the wires of each side (Figure 2.1). This distance defines the maximum drift path.

The electronics are designed to allow continuous read-out, digitization and independent waveform recording of signals from each of the wires of the TPC. A 10-bit ADC digitization at 400 ns sampling provides a dynamic range of up to about 100 minimum ionizing particles. The average electronic noise is typically of about 1500 electrons r.m.s., to be compared with $\sim$ 15000 free electrons signal recorded for a 3 mm minimum ionizing particle. Therefore signal to noise ratio S/N is ~ 10.

Ionization in LAr is accompanied by scintillation light emission. A total of 74 photomultipliers (PMT) of 8" diameter sensitive to the 128 nm LAr UV-light, located behind the transparent wire planes, are used to detect the prompt scintillation light produced in LAr simultaneously with ionization [10]. They are used to trigger the presence of the neutrino signal within a CNGS related 60 μs gate, to detect atmospheric neutrinos and cosmic muons, and also define the precise location of an event along the drift direction. A PMT threshold, set at $\sim$90 phe[1] and 110 phe for the West and East half-modules, respectively, allows full detection efficiency for events with energy deposition (E_{dep}) as low as few tens of MeV.

2.2 Liquid Argon Purity Measurements

A fundamental requirement for the performance of the Liquid Argon TPC is the need of an extremely low residual electronegative impurity content in the liquid Argon. In order to transport the free electrons created by ionizing particles, very small attenuation along

[1] photoelectron

Inner length	19600 mm
Inner width	3600 mm
Inner height	3900 mm
Active length	17950 mm
Active width	3000 mm
Active height	3160 mm
Number of TPCs in T600	4
Number of wire planes per chamber	3
Distance between wire planes	3 mm
Wire orientation with respect to horizontal	$(0°, +60°, -60°)$
Wire diameter	$150\mu m$
Wire length	
Horizontal wires	9.42 m
Wires at $\pm 60°$	3.77 m
Wires at the corners ($\pm 60°$)	3.81 - 0.49 m
Wire pitch	3mm
Wire capacitance Ind1, Ind2, Coll	20, 21, 20 pF/m
Wire nominal tension	12 N (5 N for horizontal wires)
Number of wires per module	32
Number of wires per chamber	
Horizontal wires	2112
At $\pm 60°$	2×4640
At the corners ($\pm 60°$)	2×960
Total	13312
Total number of wires in T600	53248
Cathode HV (nominal)	75 kV
Cathode to Collection plane distance	1.5 m
Maximum drift length in LAr	1482 mm
Maximum drift time in LAR (nominal field)	$950\mu s$

Table 2.1: Main features of the T600 inner detector [9].

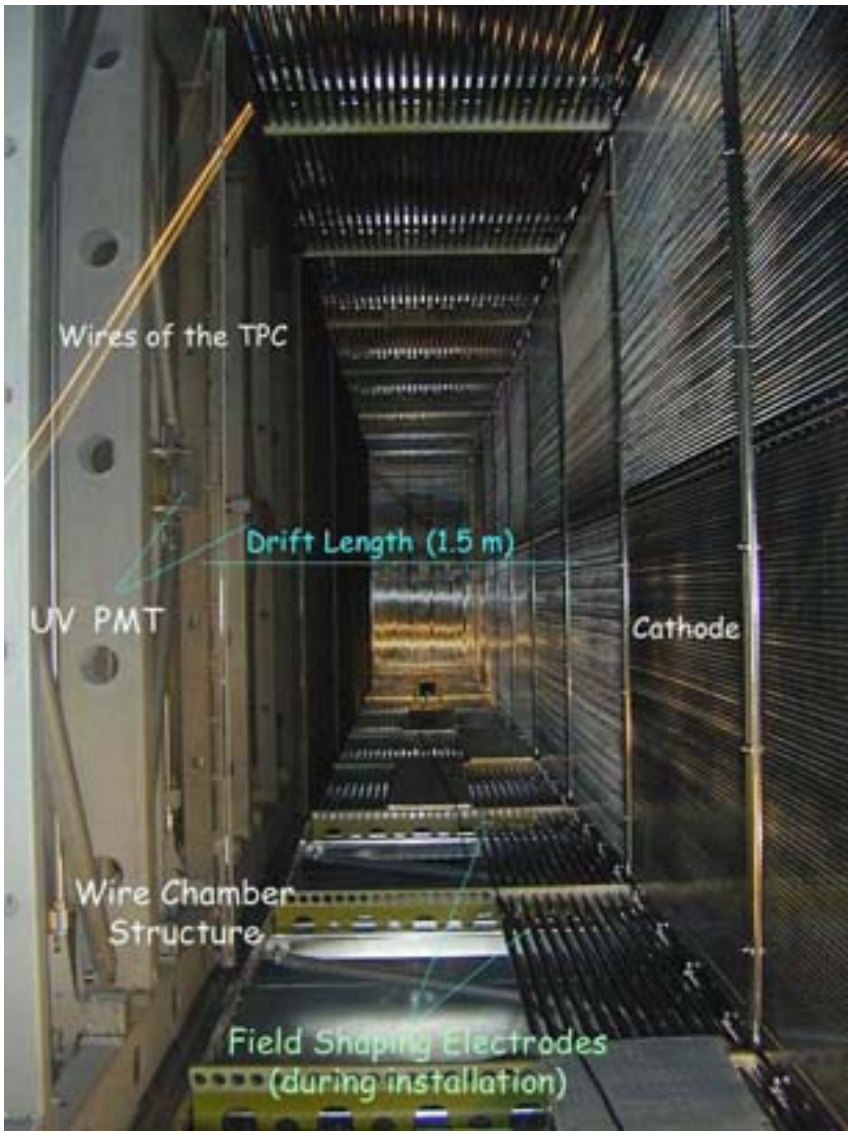

Figure 2.1: Picture of the internal detector layout inside one TPC chamber. The picture refers to the left TPC where wires, the mechanical structure of the TPC and some PMTs are visible [9].

the drift path is needed [11]. To keep the electronegative impurities (oxygen and/or fluorinated or chlorinated compounds) in LAr at a very low level, each module was equipped with gaseous Argon (GAr) and LAr recirculation/purification systems. GAr was continuously extracted from the cryostat ceiling and, re-condensed, dropped into Oxysorb^{TM} filters and returned to the LAr containers. LAr was re-circulated through an immersed, cryogenic pump and was purified through standard Hydrosorb^{TM}/Oxysorb^{TM} filters before being re-injected into the cryostat. Convective motions induced by heat loss from the module walls ensured a fast and almost complete LAr mixing, minimizing the fluctuations of the relevant parameters, such as LAr density, temperature and purity [12].

2.2.1 Determination of the free electron lifetime in LAr

The electron lifetime τ_e[2] in LAr-TPC has been measured through the attenuation of the charge signal of traversing cosmic-ray muon tracks as a function of the electron drift distance. An automatic procedure based on the recognition of the track pattern has been used to provide a first pre-selection of candidates for the purity measurements [13]. The ionization charge is measured by the area of the signal pulse above the local baseline level. To reliably fit the charge attenuation along each track, a Gaussian-like distributions are required. This can be achieved truncating the asymmetric Landau tail of the dE/dx depositions, what makes the distribution more symmetric around the most probable value [13].

2.2.2 Experimental measurement of the electron lifetime

The through going cosmic-rays collected at the rate of $\sim$ 3100 muons per day have been used to measure the free electron lifetime in the ICARUS T600 providing an almost ideal source of continuous detector calibration. The LAr purity trend in the T600 East and West modules (called with respect to the direction of CNGS beam coming from North) is shown in Figure 2.2. The red line indicates the minimum drift time at the nominal voltage of 75 kV (corresponding to an electric field of 500 V/cm and maximum drift length of 1.5 m). The analysis of the LAr purity demonstrates that the ICARUS detector

[2] τ_e: free electron lifetime is the average capture time of a free ionization electron by an electronegative impurity in LAr.

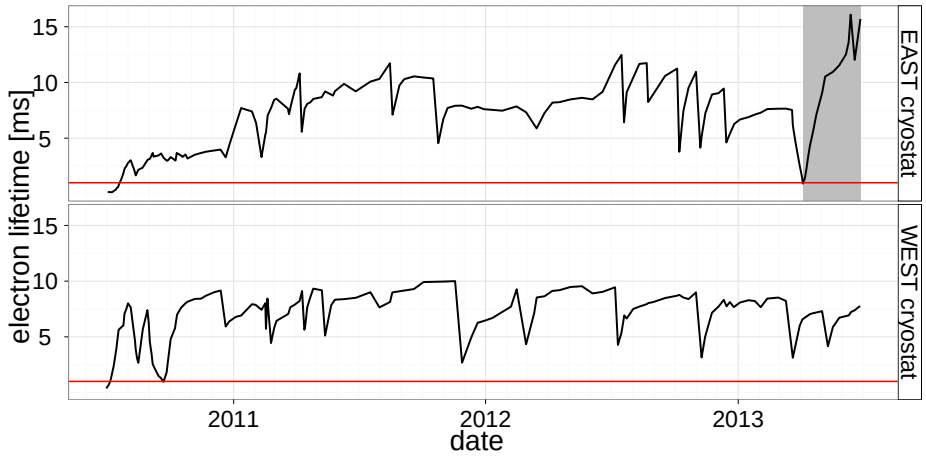

Figure 2.2: Free electron lifetime evolution in the West (bottom) and East (upper) cryostats as a function of the elapsed time from the full T600 live-time. Gray area in the East cryostat plot marks the operation of the new recirculation pump.

has operated flawlessly when both circulation systems were operational. The interruption of the liquid recirculation system for pump maintenance resulted in a rapid decrease of the electron lifetime that was restored promptly as the recirculation system was reactivated.

In April 2013 a major upgrade of the LAr recirculation system was performed in the East cryostat. The ACD CRYO pump was replaced with a new Barber Nichols BNCP-32C-000 with an external motor. During the two weeks stop of the LAr recirculation, τ_e rapidly decreased below 1 ms. After the new pump was switched on, the electron lifetime started increasing (gray area in Figure 2.2). At the end of ICARUS data taking the electron lifetime was still rising and the last measurement before the detector stop resulted to be $16.1^{+1.3}_{-1.1}$ ms corresponding to a maximum signal attenuation of 6% at 1.5 m drift distance [13].

In view of the very large dimensions of the detector, the uniformity of the observed lifetime over the volume is a crucial element. The level of accuracy achieved for the charge attenuation measurements along single muon tracks allow estimating the uniformity of the LAr purity in different regions along the 20 m detector length (see Figure 2.3).

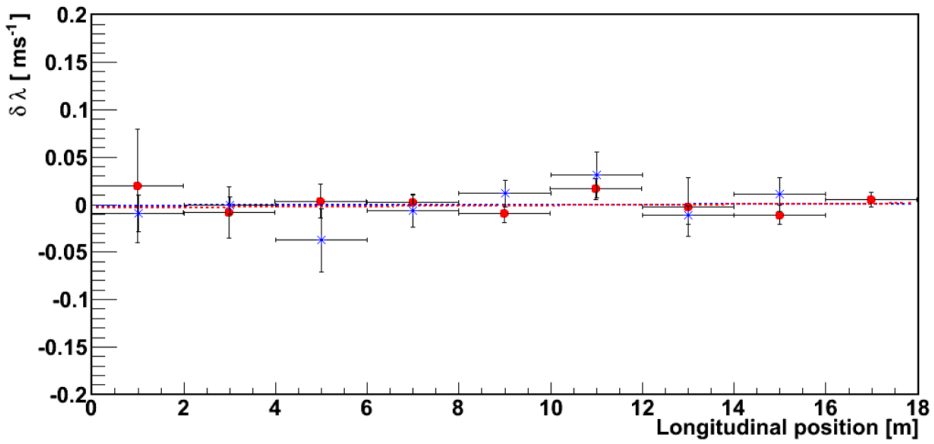

Figure 2.3: The measured variation of the level of impurities in the East cryostat along the longitudinal direction. Red circles refer to the left chamber, blue stars to the right one. The dashed lines are the linear fits in both chambers. The fit results are compatible with a uniform LAr purity across the length of the whole detector [13].

2.2.3 Independent verification of the results

Muons from neutrino events

The LAr purity measurement method was validated applying the attenuation $\lambda = 1/\tau_e$, measured with the cosmic muons, to an independent sample of muon tracks from CNGS neutrino interactions in the upstream rock, collected in the same period of time. The 254 selected CNGS muons, entering the T600 module and traveling almost parallel to the wire planes have been automatically reconstructed in 3D, and the dE/dx associated to each hit along the track has been estimated, as well as the related position along the drift. The average dE/dx of the analyzed CNGS tracks, corrected by the λ measurement, is independent from the drift coordinate within errors, demonstrating the reliability of the LAr purity estimation method [13].

Monte Carlo events

The above described method for the purity measurement has been also tested on a 9000 MC sample of muon tracks. Those muons were generated, with the energy spectrum and the angular distribution of cosmic rays measured at LNGS, by a dedicated Monte Carlo program based on the FLUKA code. The simulation includes the free electron longitudinal diffusion, the electronic response and the noise measured

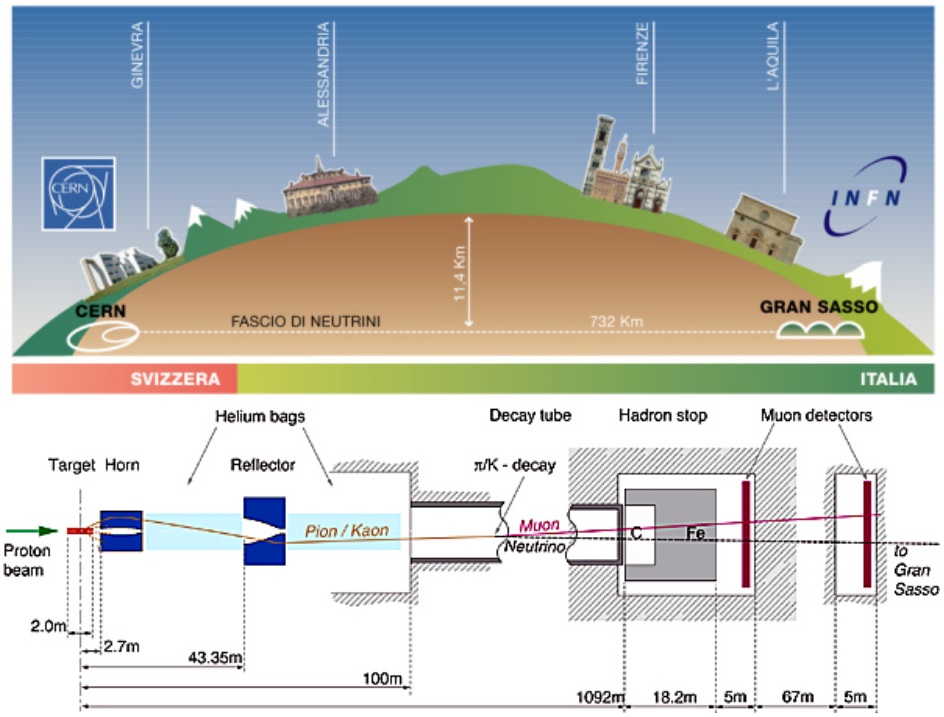

Figure 2.4: Schematic pathway of ν_μ from CERN to Gran Sasso (upper) and CNGS beam layout (bottom) [14].

in the detector, as well as the signal attenuation due to the impurities in LAr. The results established the measurement reliability in a large range of LAr purity values [13].

2.3 CNGS - Cern Neutrinos to Gran Sasso

The CNGS, CERN Neutrinos to Gran Sasso, project aimed at detecting $\nu_\mu \rightarrow \nu_\tau$ neutrino oscillation events. An intense muon-neutrino beam ($\sim 10^{17}\nu_\mu/day$) was generated at CERN and directed towards the Gran Sasso National Laboratory, 732 km away (Figure 2.4). In LNGS, large and complex detectors were designed to detect, in particular, the rare tau-neutrinos created by 'oscillation' from muon-neutrinos on their way between CERN and LNGS.

An overview of the CNGS neutrino beam facility at CERN is shown in Figure 2.4. Pions and kaons were produced (among many other particles) in the graphite target exposed on proton beam. The positively charged π/K were then selected and guided with two focusing lenses, i.e. horn and reflector, towards Gran Sasso. The decays

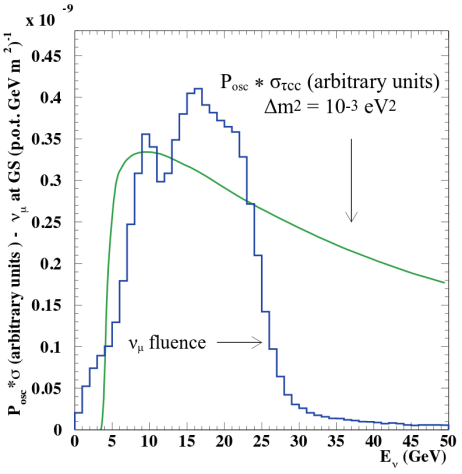

Figure 2.5: CNGS neutrino energy spectrum obtained from FLUKA simulations and oscillation probability multiplied by the ν_τ cross section [14].

of these particles into muon neutrinos and muons took place in the ∼1000 m long decay vacuum tube. The muons were afterwards measured in the muon detectors for the check on intensity of the produced neutrino beam and on the beam profile. The key feature for the experiments in Gran Sasso was the muon neutrino energy spectrum obtained from FLUKA simulations (Figure 2.5).

ICARUS T600 was taking data with CNGS beam, without major interruptions from October 2010 to December 2012. In this period it has been possible to collect an event statistics corresponding to 8.8×10^{19} pot[3] over the 9.2×10^{19} pot delivered by CERN, thanks to a detector live-time of ∼96% for CNGS exploitation (Figure 2.6).

2.3.1 ICARUS Trigger System

The ICARUS trigger system for CNGS events relied on the scintillation light signals provided by the internal PMTs and on the CNGS proton extraction time. The trigger set-up was based on a controller crate, hosting a FPGA-board for signals processing, interfaced to a PC in the Control Room for data communication and detector parameter setting. It handled different trigger sources such as signals from internal photomultipliers, CNGS proton extraction time and test pulses for electronic channel calibration. Moreover it provided the absolute time stamp for the recorded events and the opening of

[3]proton on target

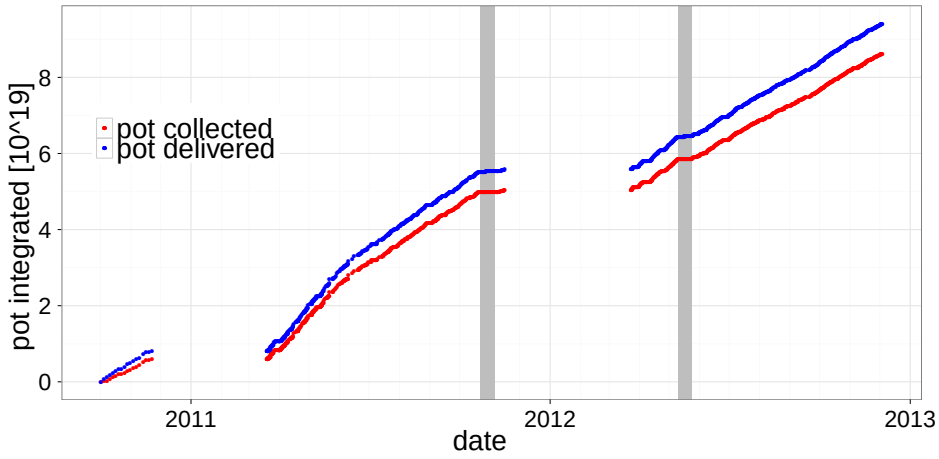

Figure 2.6: Integrated proton on target delivered to CNGS in the 2010-2012 campaigns (blue). The beam intensity recorded by T600 is also shown (red).

the CNGS proton spill gate. For every CNGS cycle two proton spills, lasting 10.5 μs each, separated by 50 ms, were extracted from the SPS machine. An "early warning" packet was sent from CERN to LNGS via Ethernet 80 ms before the first proton spill extraction, allowing to open two 50 μs gates in correspondence to the predicted extraction times [15].

The most accurate timing inside the controller was realized by a 40 MHz counter, reset every 1 ms by a synchronization signal containing absolute time information, that was generated by the master clock unit of the LNGS external Laboratories synchronized to CERN SPS accelerator clock. The discrimination thresholds for the PMT sum signals have been set at a threshold around 90 phe and 110 phe for the West and East half-module respectively, during a 60 μs spill gate in coincidence with each CNGS extraction. The CNGS-type trigger was generated when a signal from the internal PMTs of a TPC chamber was present within the CNGS gate. As a result, about 80 events per day were recorded with a trigger rate of about 1 mHz. The residual 2.4 ms delay was in agreement with the neutrino time of flight (2.44 ms) [15].

2.4 ICARUS T600 Future

The successful, continuous, long term operation of the ICARUS T600 detector in the underground laboratory, has demonstrated that

the LAr-TPC detection technique can be used in the future short and long baseline neutrino physics experiments. Decommissioning of the T600 detector took place during 2014. By the end of 2014 both TPCs were transported to CERN, where overhauling of T600 is going on, within the WA104/ICARUS, CERN-INFN project. The main objectives of overhauling, which will prepare the detector for its operation at shallow depths, are following:

- new cold vessels and purely passive insulation,
- refurbishing of the cryogenic and purification systems,
- installation of new cathode with better planarity,
- upgrade of the collection light system,
- upgrade of the read-out electronics,
- design and construction of the muon tagging system,
- further development of fully automatic tools for event reconstruction.

This two years program should be completed by the end of 2016. The upgraded T600 detector will be then transported to the Fermilab (USA), where will be one of three LAr TPC detectors within the Short Baseline Neutrino (SBN) experiment [5]. The aim of the SBN program is search for sterile neutrinos at the eV mass scale, with the use of the FNAL Booster Neutrino Beam, exploiting both appearance and disappearance channels. Three LAr TPC detectors, LAr1-ND (82 t of active mass), MicroBooNE (89 t) and ICARUS T600 (476 t), will be installed at 110 m, 470 m and 600 m from the proton target, respectively (see Figure 2.7). The neutrino anomalies, observed at: (1) accelerator neutrino, (2) reactor neutrino, and (3) radioactive Mega Curie sources in solar neutrino experiments, provide hints for possible existence of at least one, additional (i.e. fourth), non-standard, sterile neutrino state. The oscillations driven by this sterile state are characterized by large value of Δm^2_{new} of the order of $\sim$1 eV^2, and relatively small value of $sin^2(2\theta_{new})$. In three years of data taking, the SBN experiment will explore the $\nu_\mu \rightarrow \nu_e$ appearance signal with 5 σ sensitivity, in the 99% CL parameters region indicated by the LSND experiment. The ν_μ disappearance analysis, by profiting from the correlations between three LAr TPC detectors and high event rates, can extend the sensitivity by an order of magnitude beyond the present experimental limits.

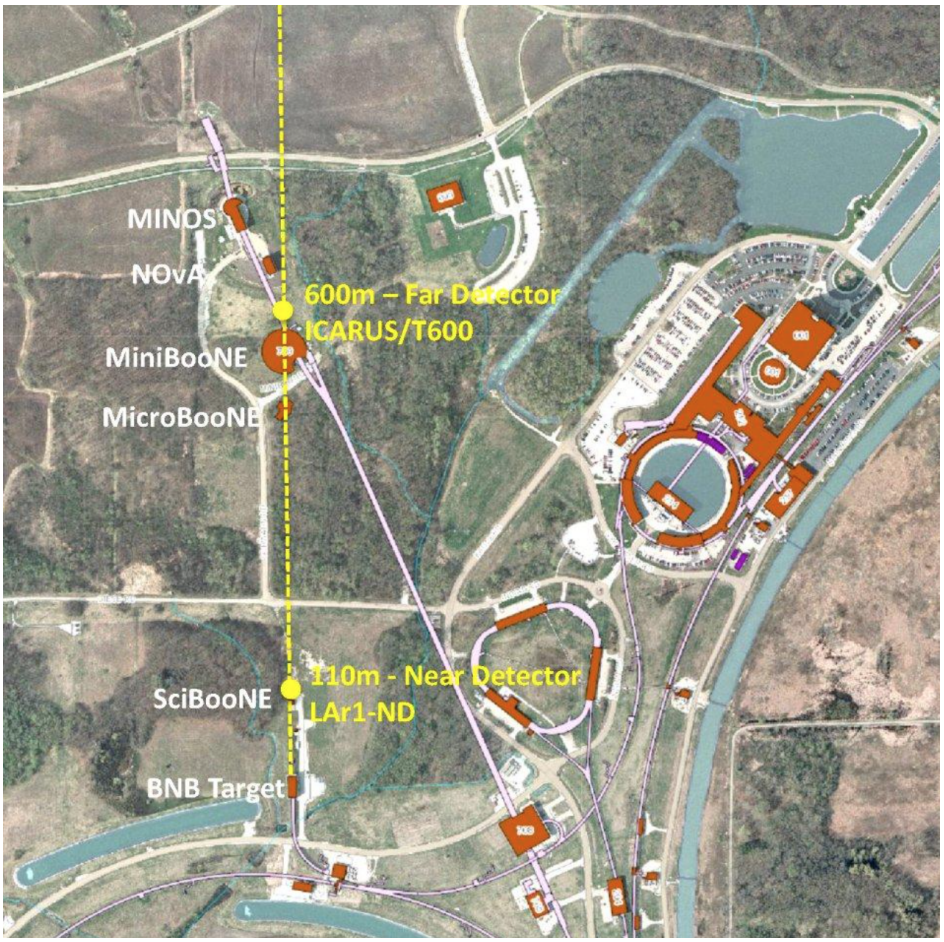

Figure 2.7: Map of the Fermilab neutrino beamline area showing the axis of the BNB (yellow dashed line) and approximate locations of the SBN detectors. The pink line indicates the axis of the NuMI neutrino beam for reference [5].

Chapter 3

Physics Program of the ICARUS T600 Experiment

Taking advantage of the LAr-TPC detection technique the ICARUS Collaboration proposed rich physics program which will be described in the following sections. Some of physics items have been fulfilled, some of them are still under investigation.

3.1 Search for $\nu_\mu \rightarrow \nu_\tau$ Oscillations

In 1958 B. Pontecorvo [16] raised the hypothesis that neutrino may oscillate. Since in that time, only electron neutrino was known, oscillations of $\nu_e \rightarrow \bar{\nu}_e$ were considered. The idea that neutrinos of different flavors may oscillate was proposed in 1962 by Maki, Nakagawa and Sakata [17]. Superposition of three mass eigenstates (ν_1, ν_2, ν_3) composes three neutrino flavors states $(\nu_e, \nu_\mu, \nu_\tau)$

$$\begin{pmatrix} \nu_e \\ \nu_\mu \\ \nu_\tau \end{pmatrix} = U^*_{PMNS} \begin{pmatrix} \nu_1 \\ \nu_2 \\ \nu_3 \end{pmatrix}, \tag{3.1}$$

where U_{PMNS} is an unitary matrix parametrized by three mixing angles $(\theta_{12}, \theta_{23}, \theta_{13})$ and complex δ_{CP} phase describing a possible CP violation in the leptonic sector

$$\begin{aligned} U_{PMNS} &= \begin{pmatrix} c_{12}c_{13} & s_{12}c_{13} & s_{13}e^{-i\delta_{CP}} \\ -s_{12}c_{23} - c_{12}s_{23}s_{13}e^{i\delta_{CP}} & c_{12}c_{23} - s_{12}s_{23}s_{13}e^{i\delta_{CP}} & s_{23}c_{13} \\ s_{12}s_{23} - c_{12}c_{23}s_{13}e^{i\delta_{CP}} & -c_{12}s_{23} - s_{12}c_{23}s_{13}e^{i\delta_{CP}} & c_{23}c_{13} \end{pmatrix} \\ &= \begin{pmatrix} 1 & 0 & 0 \\ 0 & c_{23} & s_{23} \\ 0 & -s_{23} & c_{23} \end{pmatrix} \begin{pmatrix} c_{13} & 0 & s_{13}e^{-i\delta_{CP}} \\ 0 & 1 & 0 \\ -s_{13}e^{i\delta_{CP}} & 0 & c_{13} \end{pmatrix} \begin{pmatrix} c_{12} & s_{12} & 0 \\ -s_{12} & c_{12} & 0 \\ 0 & 0 & 1 \end{pmatrix} \end{aligned} \tag{3.2}$$

where $c_{ij} = cos\theta_{ij}$, $s_{ij} = sin\theta_{ij}$. In the case of Majorana neutrinos the three-neutrino mixing matrix contains, in addition, two Majorana phases which appear in a diagonal matrix at the right of the mixing matrix U_{PMNS}.

In vacuum, on the way from the neutrino source to the neutrino detector, the evolution of the flavor state is given by

$$|\nu_\alpha(t)\rangle = \sum_{k=1}^{3} U^*_{\alpha k}\ e^{-iE_k t}\ |\nu_k\rangle, \tag{3.3}$$

where energy eigenvalues $E_k = \sqrt{p^2 + m_k^2}$, and for ultrarelativistic neutrinos $E_k \cong E + m_k^2/2E$, with $E = |\bar{p}|$ as neutrino energy assuming no mass contribution. If values of mass eigenstates are not identical, a phase $exp(-itm_k^2/2E)$ is different for each mass m_k. As a result, the probability $P(\nu_\alpha \to \nu_\beta)$ to observe a flavor state $|\nu_\beta\rangle$ at time t from a flavor state $|\nu_\alpha\rangle$ at $t=0$, turns to be non-zero

$$P_{\nu_\alpha \to \nu_\beta}(t) = \sum_{k,j=1}^{3} U^*_{\alpha k} U_{\beta k} U_{\alpha j} U^*_{\beta j}\ e^{\frac{-i\Delta m^2_{kj} t}{2E}}, \tag{3.4}$$

where

$$\Delta m^2_{kj} = m^2_k - m^2_j. \tag{3.5}$$

In the neutrino oscillation experiments the distance L between the neutrino source and neutrino detector is known. Ultrarelativistic neutrinos travel at the speed very close to the speed of light, therefore eq.(3.4) can be written as

$$P_{\nu_\alpha \to \nu_\beta}(L) = \sum_{k,j} U^*_{\alpha k} U_{\beta k} U_{\alpha j} U^*_{\beta j}\ e^{\frac{-i\Delta m^2_{kj} L}{2E}}. \tag{3.6}$$

Presently, values of the three-neutrino oscillation parameters obtained from a global fit to the oscillation data from many experiments are known. The best fit values are given in Table 3.1.

The fit values depend on the normal or inverted mass hierarchy (see Figure 3.1). Since the neutrino oscillation experiments measure only the mass square difference, there are two possibilities: for normal hierarchy - smaller mass difference is for two lighter neutrinos, and for inverted hierarchy - greater mass difference refers to two lighter neutrinos.

A direct observation of $\nu_\mu \to \nu_\tau$ oscillation, governed by θ_{23}, was the main motivation of the CNGS (CERN to Gran Sasso) project. Almost pure (contamination of $\bar{\nu}_\mu$, ν_e, $\bar{\nu}_e$ and ν_τ at the level of 2%, 0.8%, 0.3% and 10^{-5}%, respectively) ν_μ beam of energy peaked at

Parameter	best-fit	3σ
$\Delta m^2_{21}[10^{-5}\ eV^2]$	$7.54^{+0.26}_{-0.22}$	6.99 - 8.18
$\lvert\Delta m^2\rvert[10^{-3}\ eV^2]$	2.43 ± 0.06	2.23 -2.61
$sin^2 2\theta_{12}$	0.308 ± 0.017	0.259 - 0.359
$sin^2 2\theta_{23}, \Delta m^2 > 0$	$0.437^{+0.033}_{-0.023}$	0.374 - 0.628
$sin^2 2\theta_{23}, \Delta m^2 < 0$	$0.455^{+0.039}_{-0.031}$	0.380 - 0.641
$sin^2 2\theta_{13}, \Delta m^2 > 0$	$0.0234^{+0.0020}_{-0.0019}$	0.0176 - 0.0295
$sin^2 2\theta_{13}, \Delta m^2 < 0$	$0.0240^{+0.0019}_{-0.0022}$	0.0178 - 0.0298
$\delta/\pi(2\sigma$ range quoted)	$1.39^{+0.38}_{-0.27}$	$(0.00 - 0.16) \oplus (0.86 - 2.00)$

Table 3.1: The best-fit values and 3σ allowed ranges of the 3-neutrino oscillation parameters, derived from a global fit of the current neutrino oscillation data [18].

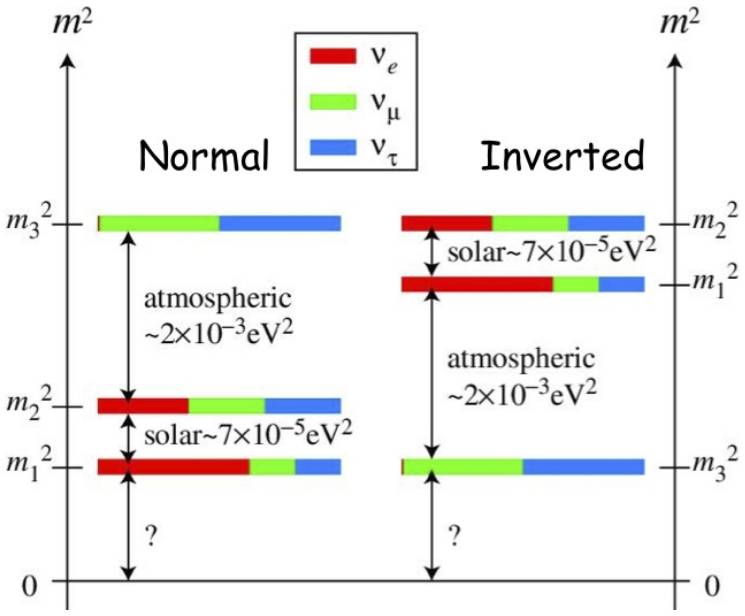

Figure 3.1: Ordering of neutrino masses as follows from analysis of neutrino experiments. The colors indicate the proportion of neutrino flavors in each of mass neutrino states, i=1, 2, 3.

$\sim$20 GeV (see Figure 2.5) was produced at CERN and delivered to the Gran Sasso underground laboratory. High energy threshold needed for ν_τ CC interaction prevented low energy beam experiments (K2K, T2K, ...) from $\nu_\mu \to \nu_\tau$ oscillation observation. Also ν_τ CC interactions are difficult to exhibit in water Cerenkov detectors (like Super-Kamiokande), due to high multiplicity of the final state coming from multi-GeV ν_τ interaction.

To search $\nu_\mu \to \nu_\tau$ oscillations, OPERA [19] and ICARUS detectors were exposed to the ν_μ CNGS beam. Emulsion detection technique, which allow to reconstruct trajectories of high energy particles with a submicrometric accuracy was chosen by the OPERA Collaboration. They observed four ν_τ events [20], [21], [22], [23] in agreement with the detector mass and exposure, beam intensity, reconstruction efficiency and values of neutrino oscillation parameters.

In the ICARUS experiment the search for the ν_τ signal was based on the kinematical suppression of the background. The main ν_τ detection channel is $\bar{\tau} \to \bar{e}\bar{\nu}_e\nu_\tau$, with branching ratio of 17.8%, with small background originating mainly from CC interactions of ν_e beam contamination. Taking into account the entire ICARUS data taking period, CNGS beam intensity, reconstruction efficiency, and $sin^2\theta_{23} \approx 0.4$, about 3 ν_τ CC events should be observed.

In the time of writing this thesis the scanning of ICARUS data was still in progress, not resulting in evidence of observation of $\nu_\mu \to \nu_\tau$ oscillation.

3.2 Search for Sterile Neutrinos

The LSND experiment [24] at LANSCE Los Alamos accelerator and the MiniBooNE experiment [25] at the FNAL-Booster have reported significant evidence for an anomalous excess of ν_e and $\bar{\nu}_e$ events. These results may imply the existence of new sterile neutrino flavor with additional mass-squared differences and new elements of the mixing matrix which will affect the $\nu_\mu \to \nu_e$ oscillations. The mass-squared difference allowed by the LSND and MiniBooNE for an additional neutrino state will be in a wide interval $\Delta m^2_{new} \sim 0.01 \div 1.0\ eV^2$ with a corresponding associated value of $sin^2(2\theta_{new}) = 4|U_{e4}|^2|U_{\mu 4}|^2$, largely incompatible with the standard three neutrino mixing model.

The LSND anomaly would manifest as an excess of ν_e events, characterized by a fast energy oscillation averaging approximately to $sin^2(1.27\Delta m^2_{new}L/E_\nu) \approx 1/2$ with probability $P_{\nu_\mu \to \nu_e} = 1/2 sin^2(2\theta_{new})$.

The ICARUS analysis was based on over 3000 events collected in

2010-2012 [6], [7]. Four clear ν_e events have been visually identified with the expectation of 6.4 ± 0.9 events from conventional sources. At 90% and 99% CL, the limits to possible oscillated events are 3.7 and 8.3, respectively. The corresponding limit to oscillation probability becomes 3.4×10^{-3} and 7.6×10^{-3}, respectively.

The window for the LSND anomaly is strongly limited to a narrow region around $(\Delta m^2, sin^2(2\theta))_{new} = (0.5\ eV^2, 0.005)$, with an overall agreement (90% CL) between the present ICARUS limit, the published limits of KARMEN and the published positive signals of LSND and MiniBooNE Collaborations (Figure 3.2).

The result of the ICARUS Collaboration is compatible with the absence of a LSND anomaly. Nevertheless, further experimental efforts are required to prove the possible existence of sterile neutrinos.

Compared to the ICARUS measurement at the CNGS beam, much shorter distances and lower neutrino energies will allow to increase the event rate, reduce the overall particle multiplicity of the neutrino events, and enlarge the angular range of the secondaries substantially improving the ν_e selection efficiency.

3.3 Atmospheric Neutrinos

The interaction of primary cosmic rays (mainly protons) with nuclei in the Earth's atmosphere is a source of hadrons and their decay products. Abundantly produced secondary pions are source of muon neutrinos

$$\begin{aligned} \pi^+ &\rightarrow \mu^+ + \nu_\mu, \\ \pi^- &\rightarrow \mu^- + \bar{\nu}_\mu. \end{aligned} \tag{3.7}$$

The subsequent muon decays are source of muon and electron neutrinos (antineutrinos)

$$\begin{aligned} \mu^+ &\rightarrow e^+ + \nu_e + \bar{\nu}_\mu, \\ \mu^- &\rightarrow e^- + \bar{\nu}_e + \nu_\mu, \end{aligned} \tag{3.8}$$

which can be detected in terrestrial detectors working underground. Super-Kamiokande water Cerenkov detector, through the evidence of an up-down asymmetry of recorded atmospheric muon neutrino interaction, proved neutrino oscillations [26].

Even with fiducial mass much lower than 22 kton of water of Super-Kamiokande detector, the ICARUS T600 can give contribution to atmospheric neutrinos studies. Reconstruction of higher than few GeV events, resulting in complicated multi-prong topologies can

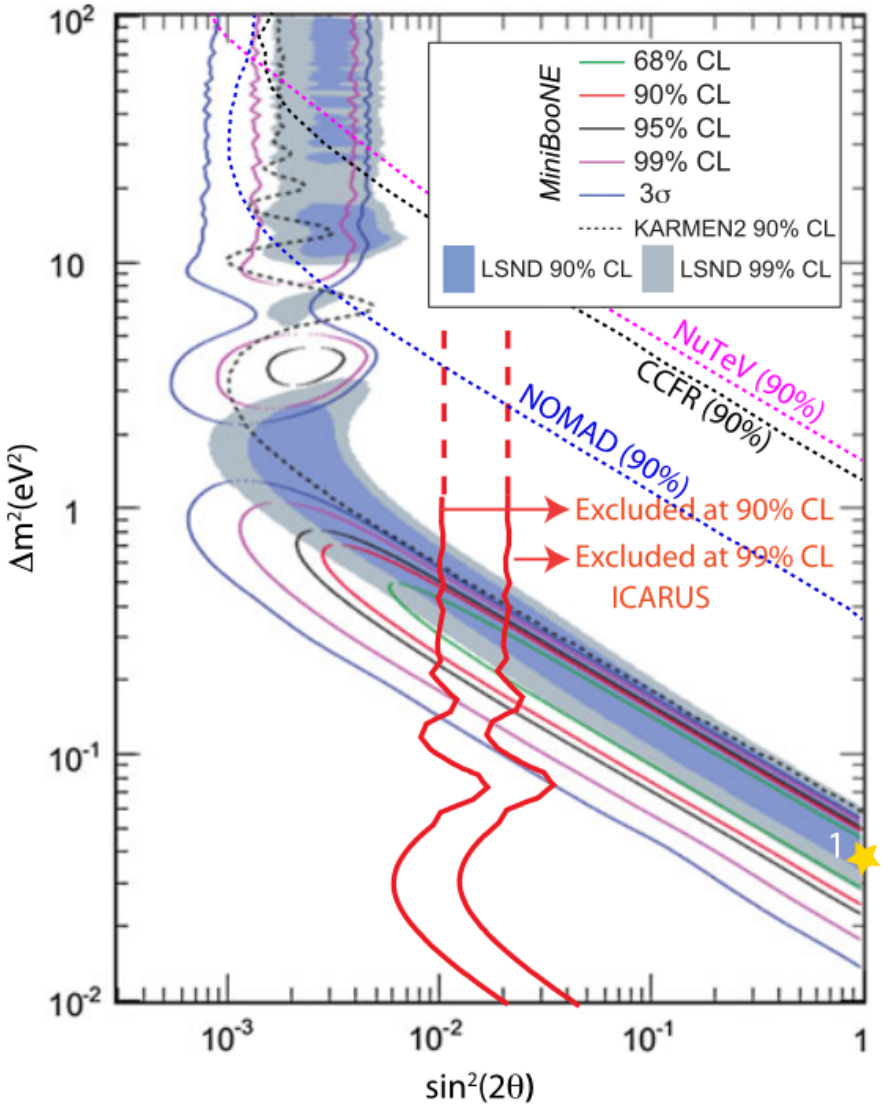

Figure 3.2: Two-dimensional plot of Δm^2 versus $sin^2 2\theta_{new}$ for the main published experiments sensitive to the $\nu_\mu \rightarrow \nu_e$ anomaly and the present ICARUS result [6].

be performed more completely using LAr detection technique. Moreover, ICARUS detector can measure both NC and CC interactions for all three neutrino flavors, down to energy of few tens of MeV. The study of atmospheric neutrino sample is also important for nucleon decay searches, as it represent substantial part of the background.

The predicted number of atmospheric neutrino electron-like and muon-like events in ICARUS T600 are equal to 41 and 31, respectively [27].

The visual scanning of collected atmospheric data (one example in Figure 3.3), which are automatically preselected asking for an interaction vertex, is ongoing. The number of found events is consistent with the Monte Carlo expectations.

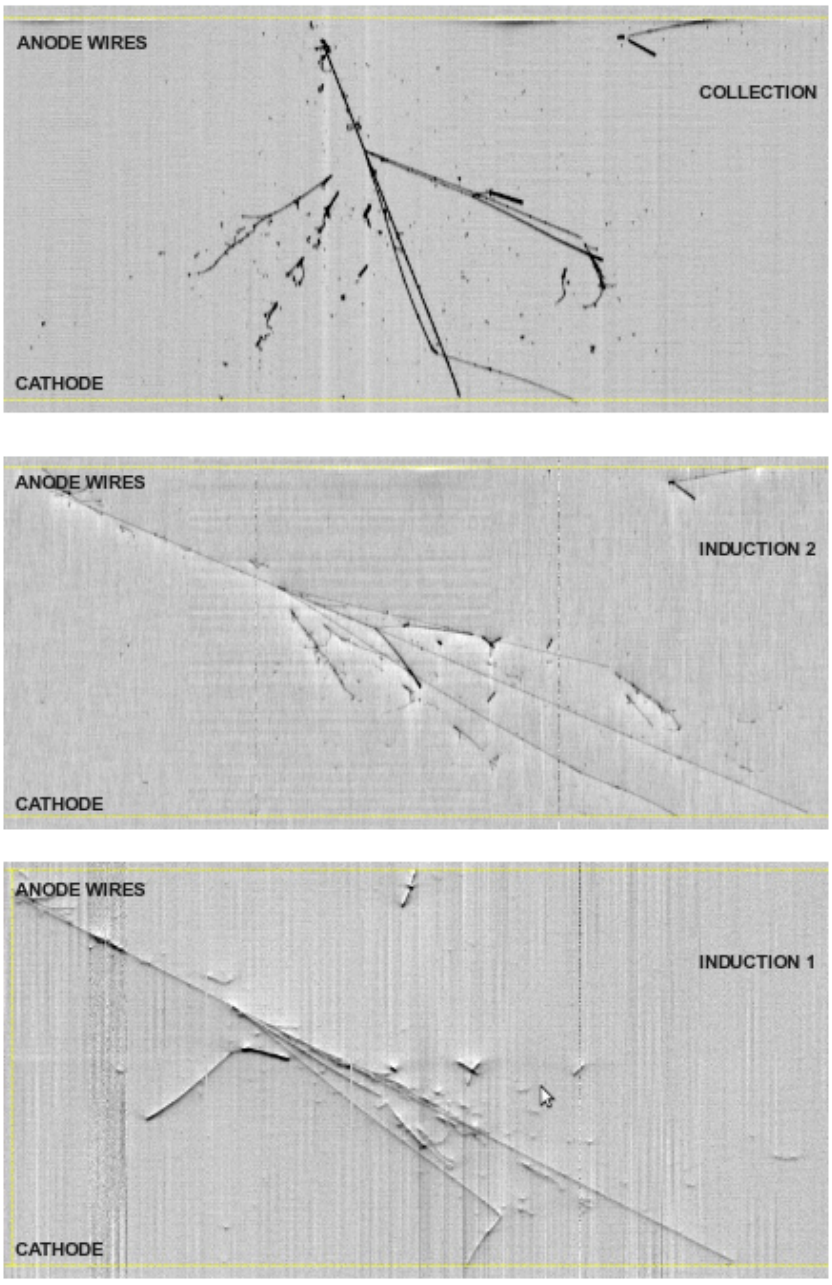

Figure 3.3: An example of an interaction of atmospheric neutrino inside fiducial volume of the ICARUS detector.

3.4 Superluminal Neutrinos

In 2011 the OPERA Collaboration has announced surprising results on the measurement of the velocity of neutrinos [28]. OPERA reported that neutrinos arrive earlier than expected from luminal speed by a time interval:

$$\delta t = 57.8 \pm 7.8_{stat}{}^{+8.3}_{-5.9_{sys}}\ ns. \tag{3.9}$$

This result has triggered new experimental searches.

Cohen and Glashow [29] have argued that such super-luminal neutrinos should lose energy by producing photons and e^+e^- pairs, through Z_0 mediated processes, analogous to Cerenkov radiation:

$$\begin{aligned} &\nu_x \to \nu_x + \gamma, \\ &\nu_x \to \nu_x + \nu_y + \bar{\nu}_y, \\ &\nu_x \to \nu_x + e^+ + e^-. \end{aligned} \tag{3.10}$$

The ICARUS Collaboration performed an analysis based on the 2010 and part of the 2011 data sets [30]. It was found that the rates and deposited energy distributions of neutrino events agree with the expectations for an unperturbed spectrum of the CERN neutrino beam. No super-luminal Cerenkov-like e^+e^- pair or γ emission event has been directly observed. ICARUS results refute therefore a super-luminal interpretation of the OPERA result, according to the Cohen and Glashow prediction.

At the end of the 2011 run (October 21^{st} - November 4^{th}) and in the middle of 2012 (10^{th} to 24^{th} May), the CERN CNGS neutrino beam has been operating in lower intensity mode with $\sim 10^{12}$ pot/pulse and with a proton beam structure made of LHC-like extractions (gray areas in Figure 2.6) [31], [32]. This tightly bunched beam structure allowed a very accurate neutrino time of flight measurement on an event-by-event basis. During those periods, the ICARUS detector has collected 7 (in 2011) and 25 (in 2012) beam-associated events, in agreement with characteristics of neutrino events in the LAr-TPC. The resulting values of the difference between measured neutrino time of flight and the expected value

$$\begin{aligned} \delta t_{2011} &= 0.3 \pm 4.9_{stat} \pm 9.0_{sys}\ ns, \\ \delta t_{2012} &= 0.10 \pm 0.67_{stat} \pm 2.39_{sys}\ ns \end{aligned} \tag{3.11}$$

are fully compatible with the neutrino propagation at the speed of light.

Those measurements excluded the hypothesis of neutrino velocities exceeding the speed of light by more than 1.35×10^{-6} c at 90% CL.

3.5 Nucleon Decay

The Grand Unification refers to integration of the electroweak and strong interactions at large energy scale, which is highly beyond today's acceleration techniques. In the Grand Unification Theories (GUTs) the conservation of baryon number can be violated, i.e. a baryon can decay into meson (or mesons) and antilepton. Therefore, an observation of a nucleon decay non-conserving the baryonic number will be a direct evidence of physics beyond the Standard Model.

Searches for nucleon decay are unavoidable in the physics program of every neutrino experiment. The results are presented as partial lifetime lower limits τ. The sensitivity to nucleon decay depends on: (1) the detector exposure, usually expressed in kilotons per year, (2) the selection efficiency, and (3) the constrained CL upper limit on the number of observed signal events, obtained from the ratio of two Poisson functions including estimated background.

The exposure is of great advantage for the water Cerenkov detectors. Super-Kamiokande provided, so far, the best limits on several decay modes of nucleon decay [34]. However, not all nucleon decay modes are directly accessible for water Cerenkov detectors. For example: K^+ meson from $p \to K^+\bar{\nu}$ has momentum below the Cerenkov threshold, therefore its detection has to relay on measurement of decay products with low detection efficiency.

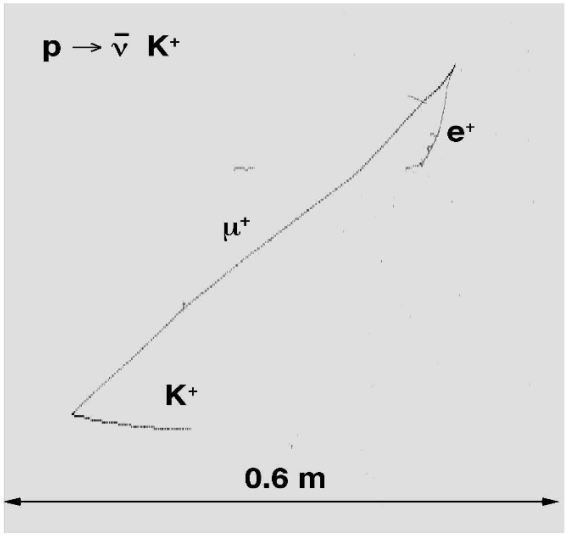

Figure 3.4: Simulated proton decay in the preferred channel in Supersymmetric models $p \to K^+\bar{\nu}$ as could be observed in ICARUS detector [33].

In the ICARUS detector the identification of K^+ and its decay products (see Figure 3.4) can be done with much higher efficiency. The background can be effectively eliminated by the measurement of the energy deposited by charged particles equal to the nucleon mass [33]. The ICARUS detector sensitivity to the proton and neutron decay is presented in Figure 3.5. The results were obtained from Monte Carlo simulations, including nuclear effects, and detailed studies of dominant background component from atmospheric neutrino interactions in LAr.

3.6 Supernovae Neutrinos

The only, so far, neutrinos from SN1987A supernova (SN) collapse, have been detected in 1987 by three terrestrial detectors: Kamiokande [35], [36], IBM [37] and Baksan [38]. Since that time an observation of SN explosion neutrinos comprises physics program of a neutrino experiment. All neutrino flavors produced during SN collapse can be detected in the ICARUS LAr TPC via charge and neutral current interactions. The total number of expected SN events in the ICARUS detector come from:

- elastic scattering on electrons (sensitive to all neutrino flavors): $\nu_x + e^- \rightarrow \nu_x + e^- \qquad x = e, \mu, \tau,$
- absorption of ν_e on Argon nuclei: $\nu_e + \ ^{40}Ar \rightarrow e^- + \ ^{40}K^*,$
- neutral current interactions on Argon nuclei (for all flavors).

A direction of a single recoil electron in the elastic scattering gives the possibility to determine the SN source.

Reaction	Number of events
elastic	8 (8)
CC	153 (200)
NC	182 (182)
total	343 (390)

Table 3.2: Expected number of SN events in ICARUS T600 detector for normal (inverted) mass hierarchy [33].

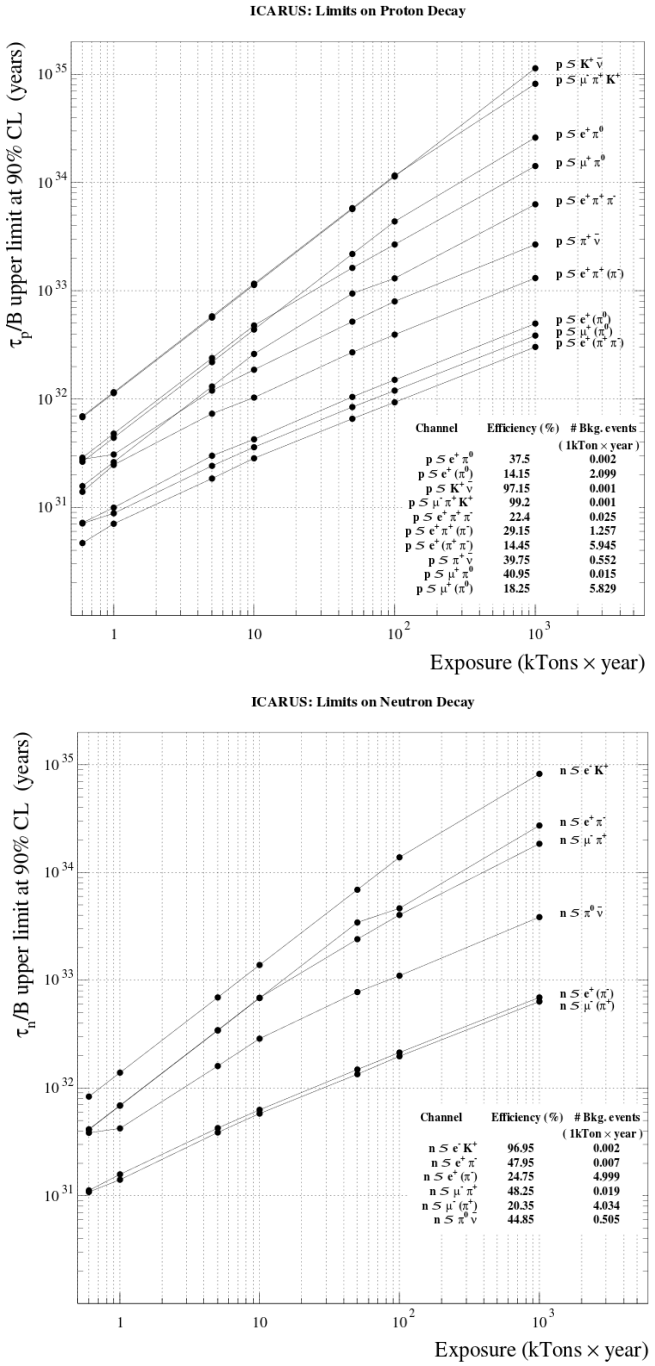

Figure 3.5: Lifetime limits for the proton (top) and neutron (bottom) decay (τ/B) with the exposure. The limits are at 90% confidence level. The tables indicate the selection efficiencies and the estimated number of background events for each decay mode, at an exposure of 1 $kton \times year$ [33].

The number of observed SN events depend on the neutrino mass hierarchy: normal or inverted. In the Table 3.2 the expected number of neutrino events in the ICARUS T600 detector from SN explosion at a distance of 10 kpc is given. The total binding energy of 3×10^{53} ergs, mean energies of 11 MeV, 16 MeV and 25 MeV for ν_e, $\nu_{\bar{e}}$ and $\nu_{\mu,\bar{\mu},\tau,\bar{\tau}}$ respectively, and the same luminosity for all neutrino species have been used to obtain these numbers.

Chapter 4

Electromagnetic Showers

The core of the analysis made by the author of this thesis is based on electromagnetic showers studies. In this chapter, a theoretical introduction to this topic is presented. Electromagnetic showers in LAr can be initiated by electrons or photons. The interactions with matter of those particles is essential in order to understand the processes occurring in LAr.

4.1 Interaction of Charged Particles

The passage of charged particles through matter is described by two principal features: (i) a loss of energy and (ii) a deflection from its incident direction [39]. These effects are the result of the following main processes:

1. inelastic collisions with the atomic electrons of the material,
2. elastic scattering from nuclei,
3. emission of Cerenkov radiation,
4. nuclear reactions,
5. bremsstrahlung.

From the point of view of particle interaction with matter, charged particles are divided into two classes: (1) electrons and positrons, which will be discussed in this chapter, and (2) heavy particles, for instance muons, pions, protons, α-particles.

The inelastic collisions occur with a certain probability. However, the fluctuations in the total energy loss are small and one can use the average energy loss per unit path length. This quantity, often called

the *stopping power* or *dE/dx*, was first calculated by Bohr using classical arguments and later by Bethe, Bloch and others using quantum mechanics.

The Bethe-Bloch Formula

The *linear stopping power* S for charged particles in a given absorber is defined as the differential energy loss divided by the corresponding differential path length [40]:

$$S = -\frac{dE}{dx}. \tag{4.1}$$

The value of *-dE/dx* along particle track is also called its *specific energy loss* or its "rate"of energy loss. For particles with a given charge, S increases as the particle velocity decreases.

The correct quantum-mechanical calculation of energy loss by charged particles was first performed by Bethe, Bloch [41] and other authors. The energy transfer is parametrized in terms of momentum transfer as it is a measurable quantity. The obtained formula is the following:

$$-\frac{dE}{dx} = 2\pi N_a r_e^2 m_e c^2 \rho \frac{Z}{A} \frac{z^2}{\beta^2} \left[ln\left(\frac{2m_e\gamma^2 v^2 W_{max}}{I^2} \right) - 2\beta^2 \right]. \tag{4.2}$$

Eq.(4.2), commonly known as the *Bethe-Bloch formula*, is the basic expression used for energy loss calculations. In practice, however, two corrections are added [40]: the *density effect* correction δ and the *shell* correction C, so that

$$-\frac{dE}{dx} = 2\pi N_a r_e^2 m_e c^2 \rho \frac{Z}{A} \frac{z^2}{\beta^2} \left[ln\left(\frac{2m_e\gamma^2 v^2 W_{max}}{I^2} \right) - 2\beta^2 - \delta - 2\frac{C}{Z} \right], \tag{4.3}$$

where
$2\pi N_a r_e^2 m_e c^2 = 0.1535\ MeV cm^2/g$
r_e: classical electron radius $= 2.817 \times 10^{-13}\ cm$
m_e: electron mass $= 5.486 \times 10^{-4}\ u$
N_a: Avogadro's number $= 6.022 \times 10^{23}\ mol^{-1}$
I: mean excitation potential
Z: atomic number of absorbing material
A: atomic weight of absorbing material
ρ: density of absorbing material
z: charge of incident particle in units of e
$\beta = \frac{v}{c}$ of the incident particle

$\gamma = 1/\sqrt{1-\beta^2}$
δ: density correction
C: shell correction
W_{max} : maximum energy transfer in a single collision.

Stopping Power

An example of the energy dependence of dE/dx is shown in Figure 4.1 which plots the Bethe-Bloch formula as a function of kinetic energy of different particles. The figure shows that the value of dE/dx for different types of charged particles approaches a near-constant broad minimum at energies above several hundred MeV, where their velocity approaches the velocity of light. This specific energy loss corresponds to about 2 MeV per g/cm^2 in light materials. Because of their similar energy loss behavior, such relativistic particles are referred to as *minimum ionizing particles (m.i.p.)*. At low particle velocities, the Bethe-Bloch formula begins to fail. From Figure 4.1 it is clear that as a heavy particle slows down in matter more energy per unit length is deposited towards the end of its path.

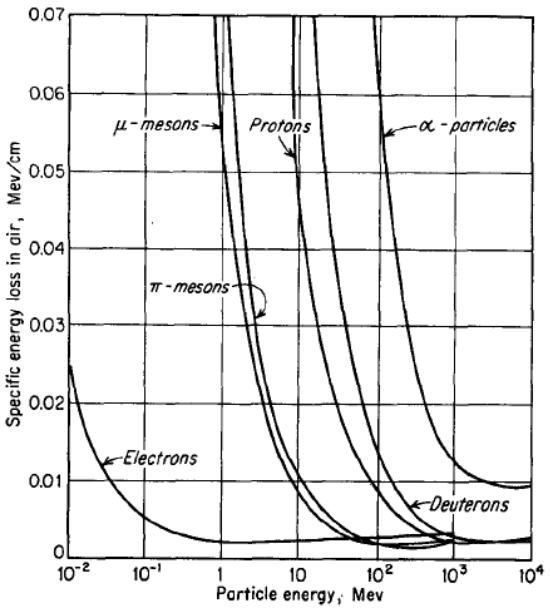

Figure 4.1: Specific energy loss dE/dx in air as a function of energy for charged particles [40].

Energy Loss of Electrons and Positrons

Electrons and positrons, like heavier charged particles, suffer a collisional energy loss when passing through matter. However, due to their small mass an additional energy loss mechanism comes into play: the emission of electromagnetic radiation arising from scattering in the electric field of nucleus (bremsstrahlung). Classically, this may be understood as a radiation arising from the acceleration of an electron (positron) as it is deflected from its straight-line course by the electrical attraction of the nucleus. At electron energies of a few MeV or less, this process is of small importance. However, as the electron energy increases, the probability of bremsstrahlung quickly goes up, so that at few 10's of MeV, loss of electron energy by radiation is comparable to, or greater than, the collision-ionization loss. At energies above *critical energy* i.e. the electron energy at which ionization and radiation losses are equal, bremsstrahlung dominates.

Electron Collision Loss

The basic mechanism of collision loss, outlined for heavy charged particles, is also valid for electrons and positrons with the modified Bethe-Bloch formula. Due to the small electron mass, the assumption that the incident particle remains undeflected during the collision process is no longer valid. Moreover, for electrons the collisions occur between identical particles, therefore the calculation must take into account their indistinguishability. These considerations change terms in the Bethe-Bloch formula, in particular, the maximum allowable energy transfer becomes $W_{max} = T_e/2$, where T_e is the kinetic energy of the incident electron or positron. If one redoes the calculations, the Bethe-Bloch formula for electrons/positrons collision energy loss reads [40]

$$-\frac{dE}{dx} = 2\pi N_a r_e^2 m_e c^2 \rho \frac{Z}{A} \frac{1}{\beta^2}\left[ln\left(\frac{\tau^2(\tau+2)}{2(I/m_e c^2)^2}\right) + F(\tau) - \delta - 2\frac{C}{Z}\right], \tag{4.4}$$

where τ is the kinetic energy of particle in units of $m_e c^2$, and

$$F(\tau) = 1 - \beta^2 + \frac{\frac{\tau^2}{8} - (2r+1)ln2}{(\tau+1)^2} \qquad for\ e^-,$$

$$F(\tau) = 2ln2 - \frac{\beta^2}{12}\left(23 + \frac{14}{\tau+2} + \frac{10}{(\tau+2)^2} + \frac{4}{(\tau+2)^3}\right) \qquad for\ e^+.$$

Bremsstrahlung

When fast electrons interact with matter, part of their energy is converted into electromagnetic radiation in form of *bremsstrahlung* [40]. Since bremsstrahlung emission depends on the strength of the electric field felt by the electron, the amount of screening from the atomic electrons surrounding the nucleus plays an important role. The fraction of electron energy converted into bremsstrahlung increases with increasing incident electron energy and is the biggest for materials with high atomic number. Bremsstrahlung spectrum is a continuum, which becomes more intense and whose peak intensity shifts toward higher frequencies, as the change of the energy of the accelerated particles increases [40].

4.2 Interaction of Photons

The behavior of photons in matter is dramatically different from that of charged particles. In particular, the photon's lack of an electric charge makes impossible many inelastic collisions with atomic electrons so characteristic to charged particles. The following three processes are the most important in gamma rays interaction with matter [40]:

1. photoelectric effect,
2. Compton scattering,
3. pair production.

All these processes lead to the partial or complete transfer of the photon energy to electron energy: the photon either disappears entirely or is scattered through a significant angle.

Photoelectric Effect

The photoelectric effect involves the absorption of a photon by an atomic electron with the subsequent ejection of the electron from the atom. The electron is ejected from its shell with a kinetic energy E, given by

$$E = E_\gamma - E_b,$$

where E_γ is the gamma-ray energy and E_b represents the binding energy of a photoelectron. In addition to the photoelectron, the interaction also creates an ionized absorber atom with a vacancy in one of its bound shells. This vacancy is quickly filled through capture of a free electron from the medium and/or rearrangement of electrons

from other shells of the atom. Therefore, one or more characteristic X-ray photons may be generated [40], [39].

Compton Scattering

The interaction process of Compton scattering takes place between the incident photon and an electron in the absorbing material. In Compton scattering, the incoming photon is deflected through an angle θ with respect to its original direction. The photon transfers a portion of its energy to an electron, called a *recoil electron*. Because all angles of scattering are possible, the energy transferred to the electron can vary from zero to a large fraction of the γ-ray energy [40], [39].

Pair Production

If the γ-ray energy exceeds twice the rest-mass energy of an electron (1.02 MeV), the process of pair production is energetically possible. At γ-ray energies that are only a few hundred keV above this threshold, the probability for pair production is small. This interaction mechanism becomes predominant as the energy increases into many-MeV range. In the pair production process, the γ-ray photon "disappears" and an electron-positron pair is created. The excess energy, carried by photon above the 1.02 MeV, required to create an e^+e^- pair, goes into kinetic energy shared by the positron and the electron. Because the positron will subsequently annihilate after slowing down in the absorbing medium, two annihilation photons are produced as a secondary products of the interaction [40], [39].

The relative importance of the three processes described above for different absorber materials and γ-ray energies is illustrated in Figure 4.2. The line at the left represents the energy at which photoelectric absorption (τ) and Compton scattering (σ) are equally probable as a function of the absorber atomic number. The line at the right represent the energy at which Compton scattering (σ) and pair production (κ) are equally probable.

4.3 Electron-Photon Showers

One of the most impressive results of the combined effect of pair production by high energy photons and bremsstrahlung emission by electrons is the formation of an *electron-photon shower*. A high-energy photon in matter converts into an electron and positron pair which then emit energetic bremsstrahlung photons. These, in turn, will

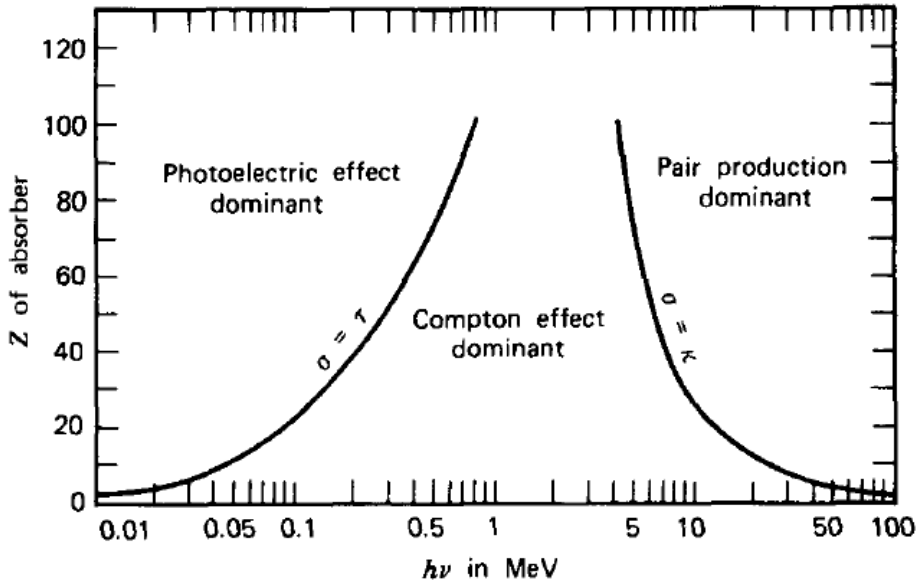

Figure 4.2: The relative importance of the three major types of gamma-ray interaction. Areas in which photoelectric effect, Compton scattering and pair production are dominant, are marked [40].

convert into further e^+e^- pairs, and so on. The result is a cascade of photons, electrons and positrons [42]. This continues until the energy of the pair-produced electrons and positrons drops below the critical energy. At this point, the e^+e^- pairs will preferentially lose their energy via atomic collisions, rather than bremsstrahlung emission, thus halting the cascade.

High-energy electrons predominantly lose their energy in matter by bremsstrahlung, and high-energy photons by e^+e^- pair production. The characteristic amount of matter, traversed for these related interactions, is called *the radiation length* X_0. It is both: (a) the mean distance over which a high-energy electron loses all but 1/e of its energy by bremsstrahlung, and (b) 7/9 of the mean free path for pair production by a high-energy photon [42]. The electromagnetic cascading is fully described by quantum electrodynamics (QED) and depends essentially on the density of the electrons in the absorber medium. For this reason it is possible to describe the characteristic longitudinal dimensions of the high-energy electromagnetic showers ($E > 1\ GeV$) in a material-independent way, using the radiation length X_0. The energy loss ΔE by radiation in length Δx can then be written as

$$(\Delta E)_{radiation} = -E(\Delta x/X_0). \tag{4.5}$$

While the high-energy part of the electromagnetic shower is governed by the value of X_0, the low-energy tail of the shower is characterized by the critical energy E_c of the medium. It is defined as the energy loss by collisions of electrons or positrons of energy E_0 in the medium in one radiation length, i.e.

$$(\Delta E)_{collision} = -E_c(\Delta x/X_0). \tag{4.6}$$

The value of E_c coincides approximately with the value of the electron energy below which the ionization energy loss starts to dominate the energy loss by bremsstrahlung. In describing electromagnetic shower behavior, it is therefore convenient to introduce the scale variables

$$t = x/X_0 \qquad and \qquad y = E/E_c, \tag{4.7}$$

so that distance is measured in units of radiation length and energy in units of critical energy.

The longitudinal development of an electron-positron shower is governed by the high-energy part of the cascade. If we assume that the shower stops abruptly at the critical energy E_c, then

$$E(t_{max}) = \frac{E_0}{2^{t_{max}}} = E_c, \tag{4.8}$$

which, solving for t_{max} yields:

$$t_{max} = \frac{ln\frac{E_0}{E_c}}{ln2}. \tag{4.9}$$

Beyond the first radiation length or so, the energy loss dE/dt, can be fitted reasonably well by the gamma distribution [43], [18]:

$$\frac{dE}{dt} = E_0 \ \beta \ \frac{(\beta t)^{\alpha-1}e^{-\beta t}}{\Gamma(\alpha)}, \tag{4.10}$$

where α and β are parameters dependent on the material. The depth t_{max} at which maximum occurs is given by

$$t_{max} = (\alpha - 1)/\beta = 1.0 \times (lny + C_j), \quad j = e, \gamma, \tag{4.11}$$

where $C_e = -0.5$ for electron-induced cascades and $C_\gamma = +0.5$ for photon-induced cascades [18].

The parameters of longitudinal shower profile given by Rossi are presented in Table 4.1.

In the early, most energetic part of the cascade, the lateral spread is characterized by the angle typical for the bremsstrahlung emission $\theta_{brems} \sim p_e/m_e$ and multiple scattering in the absorber. This latter

	Incident electron	Incident photon
Peak of shower, t_{max}	$1.0 \times (lny - 0.5)$	$1.0 \times (lny + 0.5)$
Center of gravity, t_{med}	$t_{max} + 1.4$	$t_{max} + 1.7$
Number of e^+e^- at peak	$0.3y \times (lny - 0.37)^{-1/2}$	$0.3y \times (lny - 0.31)^{-1/2}$
Total track length, T	y	y

Table 4.1: Shower parameters according to Rossi approximation B [18]. Unit of length is the radiation length.

process increasingly influences the lateral spread with decreasing energy of the shower particles, and therefore causes a gradual widening of a shower.

The transverse dimensions of electromagnetic showers is usually measured in terms of the *Moliére radius* [18], which is defined as

$$R_M = X_0 \frac{E_s}{E_c},$$

where $E_s = m_e c^2 \sqrt{4\pi/\alpha} = 21.2$ MeV and E_c is the critical energy. Like the radiation length, the Moliére radius scales fairly accurately with different materials. Qualitatively, we can see that the cascade remains relatively narrow in the first radiation lengths of its development with most of the particles contained in a dense central core. More than 90% of the shower is nevertheless contained within a distance of about $2R_M$ from the longitudinal axis.

Chapter 5

The Analysis Framework

The analysis framework of the ICARUS experiment is based on Qscan - an event visualization program and FLUKA - the Monte Carlo generator.

An example of ICARUS raw data from the Qscan program is shown in Figure 5.1. On x axis consecutive wires are placed, while the y axis denotes the drift coordinate in time samples ($\times$400 ns). A three dimensional (3D) reconstruction of an ionizing particle is possible with the use of two out of three views. In this chapter some technical details, that make the reconstruction of an event possible, are described.

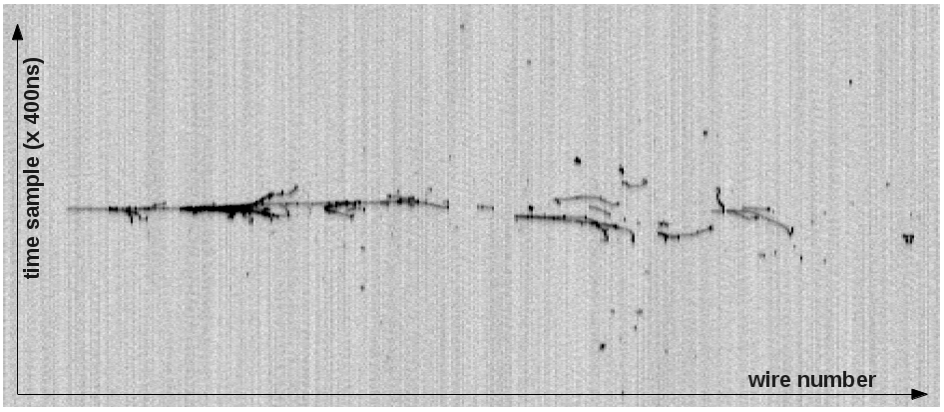

Figure 5.1: An example of an electron interaction in the ICARUS detector visualized in the Qscan.

5.1 Qscan

The Qscan program allows both, geometric reconstruction and calorimetric measurement. The reconstruction procedure extracts information provided by the wire output signals, i.e. the amount of charge deposited by different particles and the geometrical points where such deposition took place. With these information, from at least two of three anode wire planes, we are able to built a 3D picture of an event. For the calorimetric reconstruction, information from Collection anode plane is necessary.

The basic building block of a particle track is called *hit*, defined as a part of a track whose energy is detected by a given wire of the read-out wire planes [9]. The reconstruction of an event is divided into several steps realized with independent algorithms:

- *hit identification*: the hits are independently searched for on each wire as regions of a certain width above the baseline value,
- *hit reconstruction*: the parameters defining the hit (position, height, area), which contain the physical information, are determined,
- *cluster reconstruction*: hits are grouped into common charge deposition distributions based on their positions in the wire/drift coordinate plane,
- *3D reconstruction*: the hit spatial coordinates are reconstructed by using the association of hits from different views into common track segments.

Below, these steps are described in details.

5.1.1 Spatial Reconstruction

Hit Identification

The hit identification aims in distinguishing signals produced by ionization electrons from electronic noise. Hits are identified as signal regions of a certain width and values above the local mean (Figure 5.2). The number of ADC counts above the local mean by more then *threshold* indicates a hit candidate. The hit candidate is built with all the subsequent output samples above the threshold and is characterized by its width, i.e. the distance (in drift samples) between the hit initial and final points. Rejection of fake (noise) candidates is achieved by imposing a minimal width value. An extra requirement on the minimum distance from the peak position to the hit end is also

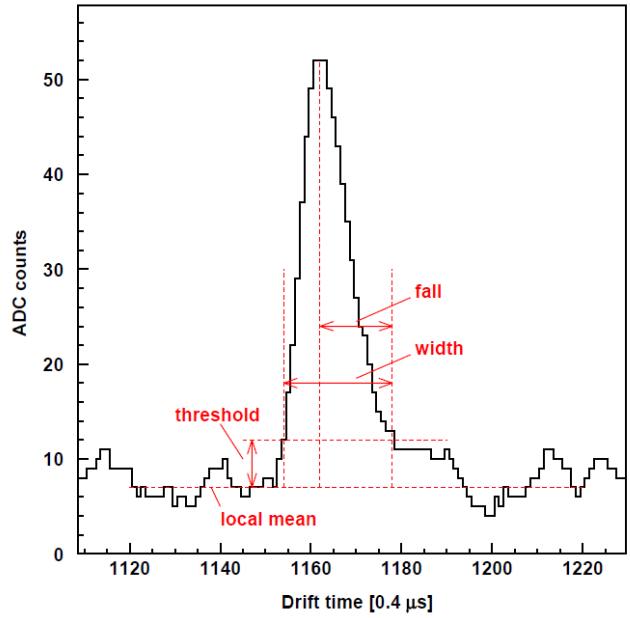

Figure 5.2: Example of a hit produced by a minimum ionizing particle on a Collection wire. Parameters used in the hit search are highlighted [9].

imposed. Once the hit has been detected, a finer hit reconstruction is performed. With this procedure, the parameters defining the hit are extracted. The hit spatial reconstruction is based on the determination of the hit peak position, whereas the hit area in Induction1 and Collection wires (or height in Induction2) is proportional to the energy deposited by ionizing particle, and therefore is the base for the calorimetric reconstruction [44].

Fine Hit Reconstruction

The output signal around the hit region is fitted with an analytic function of the drift time t:

$$f(t) = B + A \, \frac{e^{-(t-t_0)/\tau_1}}{1 + e^{-(t-t_0)/\tau_2}}, \tag{5.1}$$

where B is the fit baseline, A is the amplitude, t_0 the point for which the height of the function with respect to the baseline is equal to $A/2$, and τ_1 and τ_2 are related to the falling and rising characteristic times, respectively (Figure 5.3) [44]. This method requires the determination of the optimal window for the fit, illustrated in Figure 5.3. Fitting procedure is applied to the hits in the Collection plane only. This

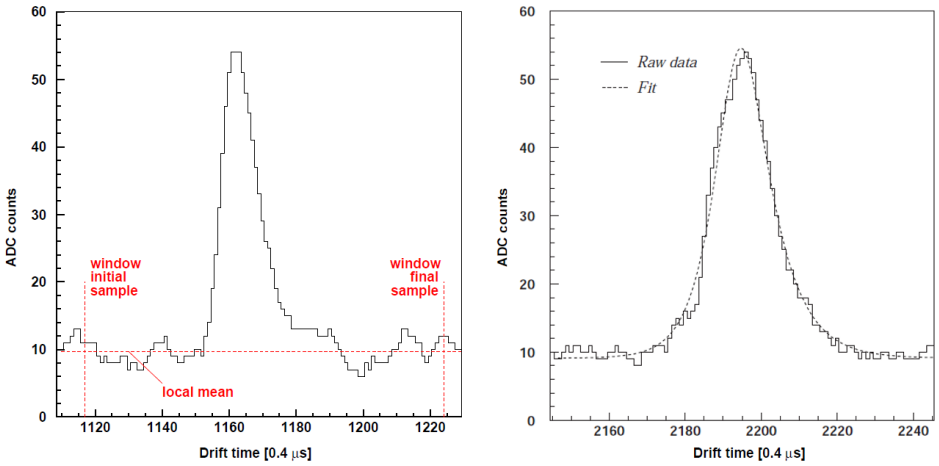

Figure 5.3: Example of computed local mean and hit windows for an isolated hit (left) and fitted signal (right) [9].

improves the hit positioning, resolves overlapping hits and allows the reconstruction of the energy deposit for individual hits.

Cluster Reconstruction

A cluster is defined as a group of adjacent hits within the wire/drift coordinate plane. The goal of the cluster reconstruction is to perform the first grouping of hits belonging to a common charge deposition, such as tracks or showers. Clusters provide identification criteria for different patterns, and thus determine which reconstruction procedure must be applied. They provide also a criterion for the discrimination between signal and noise hits, based on the cluster hit multiplicity. Clusters of the same track/shower can be *linked* between the different views, what is essential for the 3D reconstruction [44].

3D Position Reconstruction

The goal of the 3D reconstruction is the determination of the space coordinates of the energy deposition segments produced by ionizing tracks traversing the LAr-sensitive volume. Each wire plane constrains two spatial degrees of freedom of the hits, one common to all wire planes (the drift coordinate) and one specific for each plane (the wire coordinate). The redundancy on the drift coordinate allows the association of hits from different planes to a common energy deposition, and together with the wire coordinates from at least two planes, allows spatial reconstruction of a hit. The Cartesian reference frame,

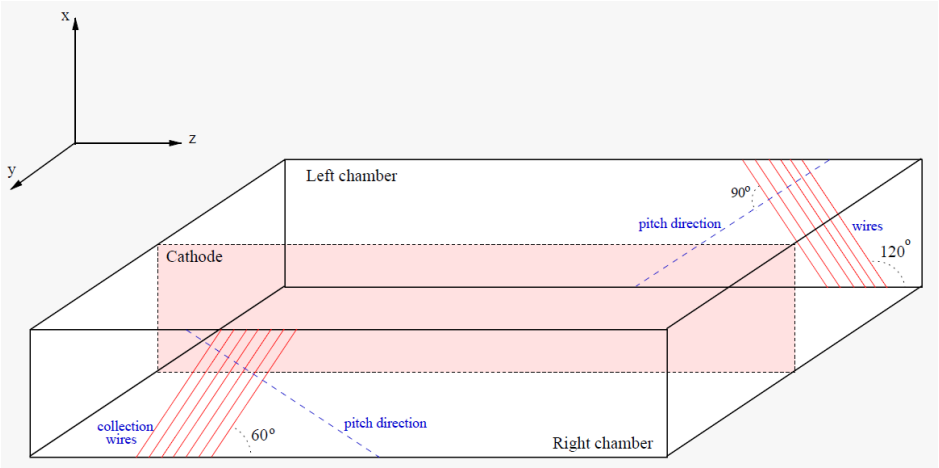

Figure 5.4: Sketch of the Cartesian reference frame of the East half-module of the ICARUS detector.

used by the ICARUS experiment defined in Figure 5.4, relates the wire and drift coordinates by the following expressions [9]:

- if Collection and Induction2 views are used:

$$Left\ \ TPC: \begin{cases} x = \frac{p}{2cos\Theta_w}(wcoll - wind2 + w_0) + X_0 \\ y = \frac{v}{f}\ scoll - Y_1 \qquad\qquad (module1) \\ y = \frac{v}{f}\ scoll + Y_0 \qquad\qquad (module2) \\ z = \frac{p}{2sin\Theta_w}(wcoll + wind2 - w_0) + Z_0 \end{cases} \tag{5.2}$$

$$Right\ \ TPC: \begin{cases} x = \frac{p}{2cos\Theta_w}(wind2 - wcoll + w_0) + X_0 \\ y = -\frac{v}{f}\ scoll - Y_0 \qquad\qquad (module1) \\ y = -\frac{v}{f}\ scoll + Y_1 \qquad\qquad (module2) \\ z = \frac{p}{2sin\Theta_w}(wcoll + wind2 - w_0) + Z_0 \end{cases} \tag{5.3}$$

- if Collection and Induction1 views are used:

$$Left\ \ TPC: \begin{cases} x = p\ wind1 + X_0 \\ y = \frac{v}{f}\ scoll - Y_1 \qquad\qquad (module1) \\ y = \frac{v}{f}\ scoll + Y_0 \qquad\qquad (module2) \\ z = \frac{p}{tan\Theta_w}(\frac{wcoll}{cos\Theta_w} - wind1) + Z_0 \end{cases} \tag{5.4}$$

$$Right\ \ TPC: \begin{cases} x = p\ wind1 + X_0 & \\ y = -\frac{v}{f}\ scoll - Y_0 & (module1) \\ y = -\frac{v}{f}\ scoll + Y_1 & (module2) \\ z = \frac{p}{tan\Theta_w}(\frac{wcoll}{cos\Theta_w} + wind1) + Z_0 & \end{cases} \tag{5.5}$$

where p is the wire pitch, Θ_w the angle of the Induction2/Collection wires with respect to the horizontal plane, w_0 half the number of wires from the Induction2 (Collection) planes intersecting with a wire from the Collection (Induction2) plane, f the read-out sampling frequency, v electron drift velocity, *wcoll* wire number in Collection view, *wind1/2* wire number in Induction1/2 plane, *scoll* drift coordinate (value of time sample). Values of the constant parameters entering the formulas are listed in Table 5.1.

3D Tracks Reconstruction

Typical approaches to the track 3D reconstruction are based on matching the hits or track end points from the individual 2D wire planes by their drift timing. There are, however, some limitations to this approach which lead to:

- position quantization in the XZ plane, 3.5×3.5 mm^2 assuming 3 mm wire spacing and 60° inclination between wires of the consecutive readout planes,

Parameter	Value
p	2.99137 mm
Θ_w	60°
f	2.5 MHz
v	1.589 mm/μs
w_0	528
X_0	2332 mm
Y_0	596 mm
Y_1	3560 mm
Z_0	-56980.5 mm

Table 5.1: Values of the constant parameters entering the formulas for the 3D Cartesian coordinates in the ICARUS detector [9].

- additional error of 3.5 mm per each wire shift with respect to the correct matching for any spurious hit matching, which introduces kinks and distortions to the reconstructed track,
- inefficiency of the reconstruction of tracks parallel to the wire planes: the low variation in the hit drift time along the track increases ambiguities in the individual hit association between wire planes,
- incomplete information, if there are missing parts of the track in one of the wire planes due to a hardware problem.

To avoid above-mentioned limitations it was proposed to built 3D objects by simultaneous optimization of their 2D projections to match data in the wire planes. A single fit function is constructed to combine all pieces of information available in data with the constraints specific to the considered object type.

The particle track T is observed in the detector as a set of three 2D projections $P_i(T)$ to Induction1, Induction2 and Collection wire planes. These projections consist of 2D hits. The 3D fit trajectory F may be projected to the wire planes. The fit F is build by minimizing the distance D between the fit projections and the track hits in all wire planes simultaneously, with constrains like trajectory curvature and distance to the already identified and reconstructed interaction vertices. For the practical implementation of constructing the best fit to a track, the Polygonal Line Algorithm (PLA) [45] was adopted.

The main advantage of this approach is the full exploitation of all available information. The reconstructed object is built in the 3D space to match data simultaneously in all its 2D projections, with a set of object-specific constraints.

General approach to 3D reconstruction for LAr TPC, with application to the track reconstruction, is described in details in [44].

5.1.2 Calorimetric Reconstruction

Electromagnetic shower energy is computed by summing the energies of all hits reconstructed in the Collection view [4]. Hits are produced by the electrons generated in the showering process in LAr. Once all hits belonging to the shower are found (clustering), the overall shower energy E is computed by summing all hit energies E_i, (index i denotes the hit inside the shower area):

$$E = \sum_i E_i, \tag{5.6}$$

given by the following formula [4]:

$$E_i(MeV) = \frac{1}{\epsilon} \frac{CW}{R} e^{\frac{t_0 - t_i}{\tau_e}} Q, \tag{5.7}$$

where

- Q is the hit area, evaluated in ADC counts over the hit baseline,
- C = $(152 \pm 2)\times10^{-4}$ fC/(ADC$\times\mu$s) is the calibration factor converting ADC counts to MeV,
- $W = 23.6\ ^{+0.5}_{-0.3}$ eV is the average energy needed for the creation of an electron-ion pair in LAr,
- ϵ is the efficiency factor described in details in section 6.3 and chapter 7,
- $R = 0.67 \pm 0.01$ is the electron-ion recombination factor (see section 6.3.2),
- $e^{\frac{t_0 - t_i}{\tau_e}}$ is the drift electron attenuation factor, t_i is the hit drift time coordinate, t_0 is the event zero-time, τ_e is the actual electron lifetime in LAr, that is monitored during the detector operation and varies run by run (see Figure 2.2).

The uncertainty σ of the energy deposit of the reconstructed hits was estimated from reconstruction of the simulated signal with added electronic noise based on the data [4]. The obtained value of σ=0.06 MeV practically does not depend on the hit energy.

5.2 Example of Fully Reconstructed Event

In this section, an example of fully reconstructed ν_μ CC CNGS event collected by T600 will be described.

The reconstruction of the final state of a neutrino interaction in LAr consists of the following steps:

- 3D geometrical reconstruction of the event topology,
- Particle Identification (PID),
- momentum reconstruction,
- total neutrino energy reconstruction.

Three dimensional reconstruction of tracks was described in section 5.1.1.

Particle identification is achieved by studying the event topology and the energy deposition per track length unit as a function of the residual particle range for muons/pions, kaons and protons stopping within the LAr active volume. A dedicated program based on a neural network for particle identification was used for this purpose.

The momenta of stopping particles can be reconstructed knowing their kinetic energy and identity. The kinetic energy is measured through calorimetry. For muons escaping the detector the momentum is determined exploiting the Multiple Coulomb Scattering along the track. All the particle momenta are summed up to obtain the total momentum.

Finally, total neutrino energy is computed as the sum of the muon energy and the energy related to the non-leptonic part of the event, using a proper correction factor, evaluated through MC simulation, to account for nuclear binding energy loss, escaping particles, neutral particles and nucleon mass production.

Event number 284 from run 9722 (Figure 5.5) was fully reconstructed by the author of this thesis and was identified as ν_μ CC CNGS beam even/, given the presence of a 4 m long minimum ionizing track at the primary vertex, attributed to the charged lepton. The primary neutrino interaction generates also three charged pions: the first gets scattered before escaping the detector from the wire plane boundary; the second interacts inelastically before decaying into muon and the muon into electron; the third, after short range, gives a secondary vertex producing one decaying particle and two heavily ionizing particles. A neutral particle, probably a neutron produced at the primary vertex, after a path of 46 cm, interacts inelastically with an Argon nucleus giving a heavily ionizing particle identified as a proton. Two electromagnetic contained showers pointing to the primary vertex have been identified as generated by two γs converting at $d_1 = 33.9$ cm and $d_2 = 11.7$ cm from the primary vertex, with energy deposition per unit length of approximately 2 and 2.6 m.i.p.s respectively in the first centimeters from the conversion points. The energy deposited by each γ amounts to $E_1 = 698 \pm 59$ MeV and $E_2 = 565 \pm 48$ MeV, respectively and the opening angle between them is $\theta_{12} = 12.5 \pm 0.4°$; the reconstructed invariant mass is 136.3 ± 4.7 MeV/c^2, in agreement with the π^0 mass. The total reconstructed momentum for the event is $p_{tot} = 13.7$ GeV/c, with a transverse momentum of $p_T = 274$ MeV/c. The total incoming neutrino energy has been evaluated to be $E_\nu \sim$15 GeV.

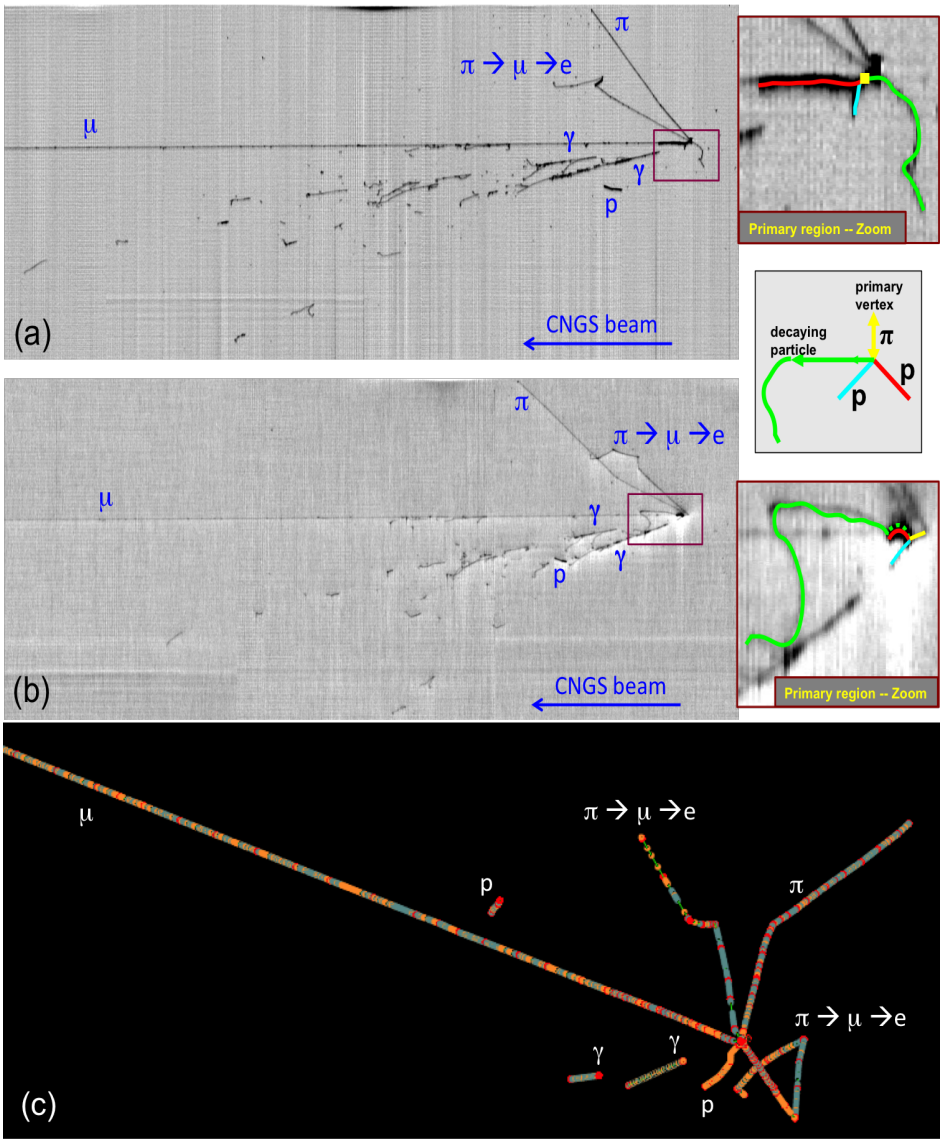

Figure 5.5: Visualization of the event 284 from run 9722 ocurring in the left TPC of the East module of the ICARUS T600 detector. Collection (a) and Induction2 (b) views of the event are presented, where vertical axes correspond to the time coordinate while the horizontal axis represents the wire number. Identified tracks are tagged with the particle name. On the right, a zoom of the primary vertex region is given for both views. The event 3D reconstruction is shown in (c).

5.3 FLUKA

Particle interactions in the ICARUS detector can be studied with the use of Monte Carlo code FLUKA [46], [47]. FLUKA is a general purpose tool for calculations of particle transport and interactions with matter, covering an extended range of applications: accelerator shielding, target design, calorimetry, dosimetry, detector design, cosmic rays, neutrino physics etc. With FLUKA one can simulate, with high accuracy, the interactions and propagation in matter of about 60 particles, including photons and electrons from 1 keV to thousands of TeV, neutrinos, muons of any energy, hadrons of energies up to 20 TeV and all the corresponding antiparticles, neutrons down to thermal energies and heavy ions.

Some particular interactions implemented in FLUKA, and used during the analysis of ν_μ CC CNGS interactions leading to π^0 production, are described below.

Electrons

FLUKA uses a complete multiple Coulomb scattering treatment what result in the correct lateral displacement even near a boundary. The variations with energy of the discrete event cross-sections and of the continuous energy loss in each transport step are taken into account exactly. Differences between positrons and electrons are implemented regarding both, stopping power and bremsstrahlung. Electron-nucleus and electron-electron bremsstrahlung cross-sections, as function of photon energy and angle are applied. Thanks to extending the differential cross-sections, the angular distribution of bremsstrahlung photons is sampled accurately. The minimum primary electrons energy is about 50 to 100 keV for low-Z materials and 100-200 keV for heavy materials, for FLUKA applications.

Photons

Photon interactions include pair production with actual angular distribution of electrons and positrons, Compton effect with account for atomic bonds through use of inelastic Hartree-Fock form factors, photoelectric effect with actual photoelectron angular distribution, optional emission of fluorescence photons and an approximate treatment of Auger electrons, and Rayleigh effect. Photon polarization can be taken into account for Compton, Rayleigh and photoelectric effects. Photohadron production is modeled according to the Vector Meson Dominance Model, modified and improved below 770 MeV, Quasideuteron interactions and Giant Dipole Resonance.

Neutrinos

The generation of neutrino interaction implemented in FLUKA handle not only Quasi Elastic (QE) interactions, but also more complicated Deep Inelastic Scattering (DIS) and production of delta resonances (RES). Hadronisation after DIS interaction is handled by the hadronisation model used and well tested in hadron-hadron interactions. With FLUKA nuclear effects in QE neutrino interactions and neutrino-nucleus reactions in DIS and RES can be studied. FLUKA package has been designed to handle Neutral Current (NC) and Charged Current (CC) interactions for incident electron, muon and tau neutrinos and antineutrinos on protons and neutrons.

Chapter 6

Electromagnetic Showers Reconstruction

In this and following chapters, the performance of the geometric and calorimetric reconstruction of the electromagnetic showers in the ICARUS T600 TPC will be evaluated.

The analysis is based on Monte Carlo simulations and on data collected by the ICARUS detector during 2011-2012 CNGS runs. A good electromagnetic shower reconstruction is fundamental for the identification and reconstruction of π^0 meson. The correct identification and reconstruction of π^0 is a key point to background rejection of NC ν_μ events with π^0 production versus the ν_e CC signal events. The procedure of reconstruction of γ initiated electromagnetic showers is realized in the following steps:

1. vertex position reconstruction,
2. identification of particle initiating electromagnetic shower (e^-/γ),
3. conversion distance calculation,
4. reconstruction of the direction of propagating shower,
5. calorimetric reconstruction.

As written above, in the first step of the analysis, the vertex position is reconstructed. It is important to know not only the amount of the energy deposited by an interacting particle, but also where the interaction occurred in the detector. Later, a precise study of energy reconstruction, that is the key for an unbiased measurement of γ shower, and for the precise energy reconstruction of π^0, will be presented.

6.1 Monte Carlo Data

In Table 6.1 sets of simulated data generated with FLUKA are shown. Simulation sets A-E contain electromagnetic showers initiated by electrons, while in sample F cascades are initiated by photons. Data sets A-D consist of 1000 monochromatic electrons with momentum of 100 MeV/c. Electrons in this four sets are generated at fixed x and z positions, while the y coordinate is changed by a step of 30 cm (see details in Table 6.1): for set A being close to the anode wires and for set D close to the cathode. Monte Carlo samples E (and F) consist of 10000 electrons (and photons) with momenta up to 3 GeV/c uniformly distributed and with interaction vertices spread uniformly in the fiducial volume of the T600 detector (in four TPCs).

In the energy range of interest for the following studies (hit finding efficiency, recombination factor) and for what concerns longitudinal profile, showers initiated by electron or photon have identical behavior. The advantage of using electrons as initiating particle is the control of the position of the MC primary vertex. Photons are invisible in the detector unless they start producing e^+e^- pairs (pair production is the main γ interaction for the ICARUS energy range - from few tens of MeV up to few GeV) and from that point it is possible to track them in the detector. In Figure 6.1 examples of electromagnetic showers interactions initiated by electron and photons are shown.

The simulated events were used in estimating the precision of vertex position reconstruction, in defining the corrections used for electromagnetic showers and for precise studies on electromagnetic shower containment.

sample	particle	p [GeV/c]	y [cm]	source distance from	
				anode [cm]	cathode [cm]
A	e^-	0.1	-90	30	118
B	e^-	0.1	-120	60	88
C	e^-	0.1	-150	90	58
D	e^-	0.1	-180	120	28
E	e^-	0-3	all	all	all
F	γ	0-3	all	all	all

Table 6.1: Generated Monte Carlo data sets used during the analysis of electromagnetic showers.

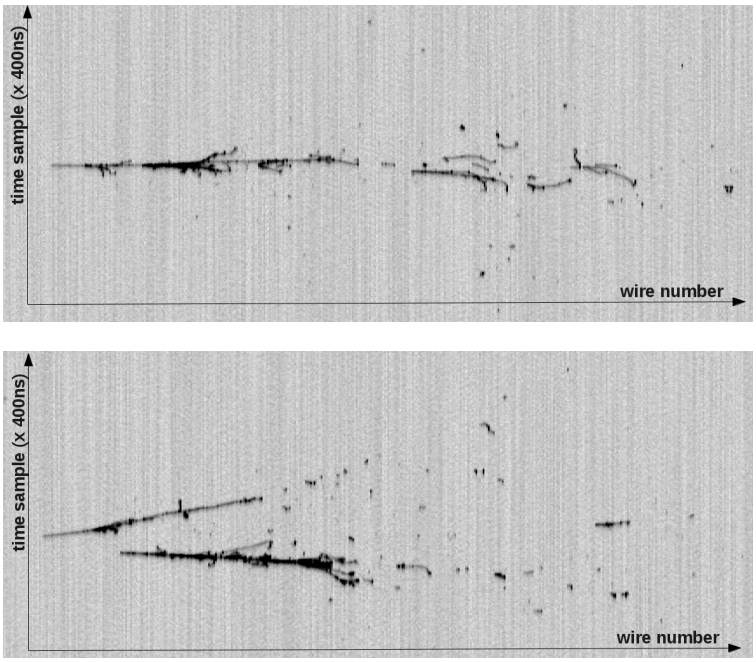

Figure 6.1: Examples of electromagnetic showers generated with FLUKA: top view - electromagnetic shower initiated by 1 GeV/c electron, bottom view - electromagnetic cascades coming from $\pi^0 \rightarrow \gamma\gamma$ decay.

6.2 Vertex Position Reconstruction

In order to study the precision of the vertex position reconstruction, a visual scanning was performed on a sample of 169 Monte Carlo events from the uniformly distributed simulated electrons (set E). The manual scanning was done by "clicking" on the point that represents a vertex in 2D. To reconstruct the position in 3D in T600 it is needed to combine information from at least two views, Collection and Induction (1 or 2) [44].

It was checked if the reconstruction of position depends on which of the two Induction views are chosen. During visual scanning the vertex position was constructed using both combinations, Collection+Induction1 and Collection+Induction2. In Table 6.2 and on Figure 6.2, the results of the position reconstruction are shown for Collection+Induction1 views (gray) and Collection+Induction2 views (red). It appears that the x coordinate is slightly better reconstructed for Collection+Induction1 views (see Figure 5.4 for the frame reference in T600). This effect, however, is not relevant for the studies discussed in this thesis. Only the 3D position need to be accurate at

	Collection+Induction1 [cm]	Collection+Induction2 [cm]
Δx	0.14 ± 0.23	0.3 ± 0.2
Δy	0.0 ± 0.4	
Δz	0.03 ± 0.23	0.011 ± 0.156
$\|r\|$	0.4 ± 0.3	0.5 ± 0.2

Table 6.2: Mean values of vertex position reconstruction taking into account views Collection+Induction1 or Collection+Induction2.

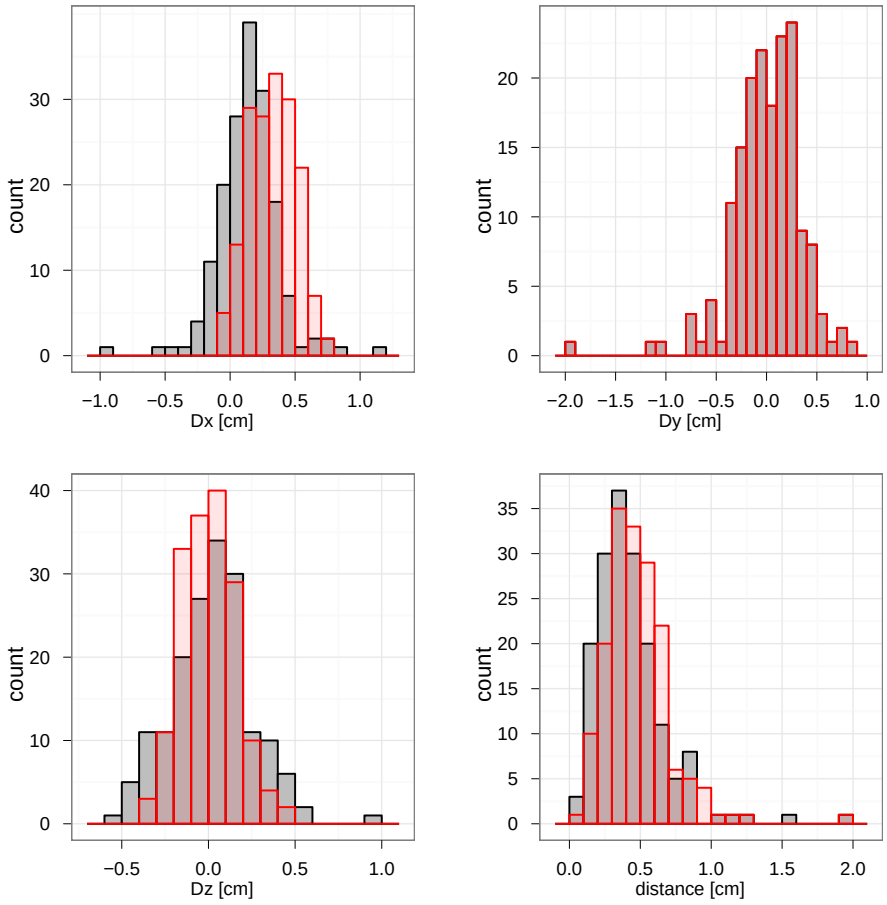

Figure 6.2: Difference between Monte Carlo and reconstructed position for x, y, z coordinates axes and the distance between reconstructed vertex and simulated interaction point (Collection+Induction1 views - gray and Collection+Induction2 views - red).

the level of millimeters. The z coordinate (direction along beam) reconstruction does not depend on the chosen view. It should be noted that the drift coordinate (y) is reconstructed only by the drift time taken from the Collection view and therefore does not depend on the choice of Induction view.

It was found that the overall resolution (scalar distance between reconstructed vertex and simulated point) for electron vertex reconstruction is better than 5 mm. This uncertainty could be attributed to the manual procedure of the position reconstruction.

6.2.1 Opening Angle Resolution

In this section a reconstruction of the opening angle θ between two γ's from π^0 decay will be evaluated. To reconstruct θ it is needed to define three interaction vertices: the point of π^0 decay and two points where pair production or Compton scattering occur (see Figure 6.3). To check the resolution of the θ angle reconstruction, a simple *toy Monte Carlo* was developed. The three points are generated according to the decay dynamic of π^0 in the energy range of interest. To the simulated positions of each point, a noise sphere with radius of 5 mm is applied (gaussian smearing). This value was chosen according to previous result on precision of position reconstruction. In Figure 6.4 the resulting resolution of θ versus the shortest of the conversion distances (a distance that a photon is traveling before converting to Compton e^- or e^+e^- pair) related to the two γ's produced in a π^0 interaction is shown.

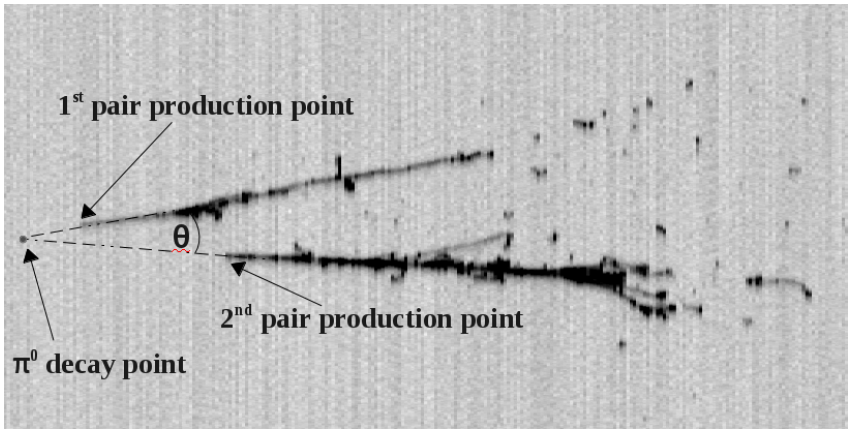

Figure 6.3: Three interaction vertices for the θ reconstruction.

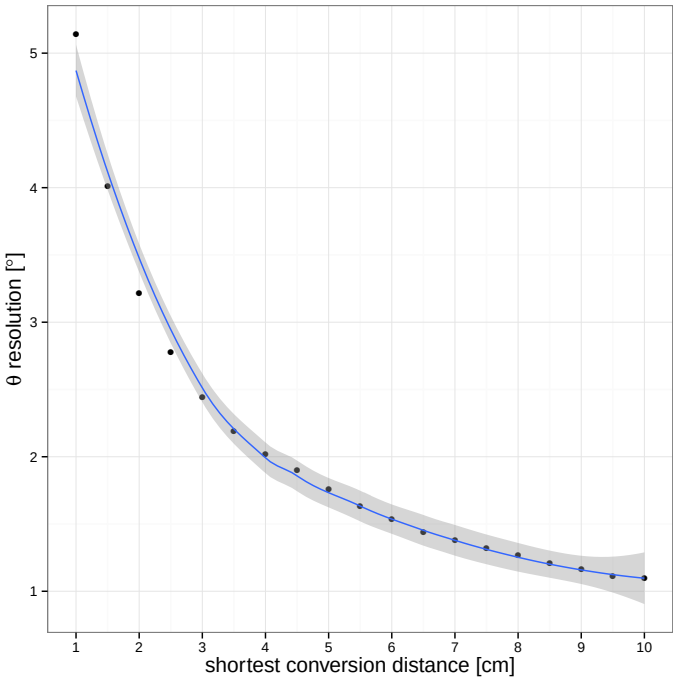

Figure 6.4: θ resolution versus shortest conversion distance.

6.3 Energy Reconstruction

The reconstruction of the deposited energy in ICARUS T600 TPC was described in section 5.1.2. In this section corrections to the reconstructed energy are discussed.

In the ICARUS T600 TPC the electromagnetic energy reconstruction from the detected charge (E_{hit}) to the shower initiating particle energy (E_{mc}) must account for several losses, namely shower uncontainment in the detector, charge attenuation due to electronegative impurities, charge quenching. Therefore the following energy estimators has to be introduced:

- E_{nq} is the fraction of the electromagnetic cascade energy that is deposited in the active volume of T600; the containment correction factor is described as $\xi = \frac{E_{nq}}{E_{mc}}$,
- E_q is the ionization charge surviving the e^--ion recombination process; the correction factor which accounts for this charge loss is $R = \frac{E_q}{E_{nq}}$,
- E_d is the charge collected after the losses due to e^- attachment by impurities during the drift toward the anode - electron drift

factor $A = \frac{E_d}{E_q}$,

- E_{hit} denotes the read out energy after the losses for the hit finding algorithm and electronic noise, its correction is defined as $\varepsilon^{shower} = \frac{E_{hit}}{E_d}$.

The importance of these four factors during the electromagnetic showers energy reconstruction in the ICARUS T600 TPC is presented schematically in Figure 6.5. One starts with E_{hit} which value has to be corrected by hit finding correction factor ε^{shower}, next the obtained value is corrected for the electron drift time factor A, electron-ion recombination factor R, and finally the containment of a shower in the fiducial volume of the detector has to be checked. After applying these corrections one should obtain the *truth* value of shower energy E_{mc}.

The analysis of the shower containment and relative connection will be discussed in the next chapter, while the other correction factors are described in the following sections.

6.3.1 Electron Lifetime Correction

One of the most important requirements for the LAr TPC, is that electrons produced by ionizing particles can travel unperturbed from the point of production to the charge-collecting anode plane. Drifting electrons may be captured by electronegative impurities that come

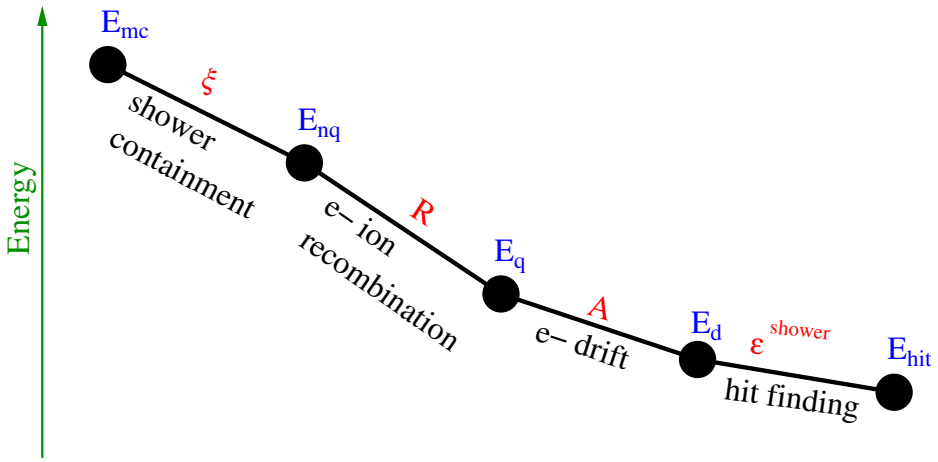

Figure 6.5: Losses in the energy measurement for electromagnetic showers in the ICARUS T600 TPC - schematic presentation. Factors ξ, R and ε^{shower} are not implemented in the ICARUS T600 reconstruction software.

from oxygen, fluorinated or chlorinated compounds present in the LAr. The LAr purification and purity measurement developed by the ICARUS Collaboration are described in details in section 2.2.

The losses of drifting electrons can be modeled by an exponential as follows:

$$Q(t_{drift}) = Q_0 \; e^{-\frac{t_{drift}-t_0}{\tau_e}} \tag{6.1}$$

and

$$A = e^{-\frac{t_{drift}}{\tau_e}}, \tag{6.2}$$

is the attenuation factor, where τ_e represent the electron lifetime that is continuously measured (see Figure 2.2 in section 2.2). In the Monte Carlo simulations a fixed value for electron lifetime of 6 ms is used.

The electron drift time (t_{drift}) ranges from 0 to 950 μs depending on the distance from the cathode of the ionizing particle. The correction for e^- losses during the drift are already implemented in the reconstruction program.

The finite value of electron lifetime also affect the hit finding efficiency ε. This inefficiency arises from the misidentification of the hits by the hit finding algorithm with respect to noise. The loss of the reconstructed hits at the shower edge, where energy deposition goes below the intrinsic wire background noise (especially for low values of τ_e) has a large impact on the value of ε. The correlation between the electron drift time factor A and ε is shown in Figure 6.6. The analysis was performed using a Monte Carlo sample with several val-

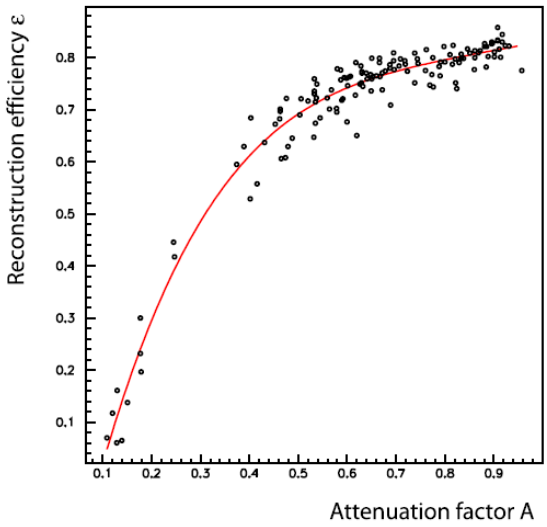

Figure 6.6: Reconstruction efficiency ε as a function of attenuation factor A [4].

ues of τ_e [4]. Depending on the values of attenuation factor, ε was found to range from 0.69 ± 0.03 ($A = 0.5$) to 0.83 ± 0.04 ($A = 1$). The author of this thesis found that, for the electromagnetic showers, additional correction (ε^{shower}) is needed with respect to reconstructed energy. For track with 1 m.i.p., hit finding has very high efficiency, while for electromagnetic showers a loss of about 4% is present. In Figure 6.7, the ratio ε^{shower} between the shower reconstructed energy (E_{hit}) and the Monte Carlo quenched energy (E_q) is shown for Monte Carlo data sets A-F. The value of ε^{shower} does not depend, neither on the position of a shower in the detector (top plot) nor on the electron lifetime (bottom plot). The value of the effective energy reconstruction factor ε^{shower} was found to be equal 0.958 ± 0.004, by averaging on the different MC data sets A-F.

6.3.2 Electron-Ion Recombination Factor

The collection of charge in the TPC is possible thanks to the electric field that drifts the electrons produced by an ionizing particle. A competing phenomena to the electron extraction is the electron-ion recombination in the ionic cloud. This effect is known as quenching and can reduce the collected energy by a significant factor. Therefore its estimation is fundamental for the reconstruction of an event energy. The electron-ion quenching is inversely proportional to the electric field; in fact higher fields extract electrons more quickly, before they start recombine. Conversely, the recombination quenching is proportional to the ionization density, that is, the energy deposited per unit length, dE/dx which depends on the particle type and its energy [48]. In the ICARUS T600 TPC the electron-ion quenching factor R is well described by the Birk's model [49]:

$$R = \frac{A}{1 + \frac{k}{\mathcal{E}} \frac{dE}{dx}}, \tag{6.3}$$

where $\mathcal{E}$ is the applied electric field, and A and k are the parameters that are extracted from a fit to the data. The average value of R for electromagnetic showers is then obtained using simulations, which account for the different ionizing power of low energy electrons in the shower using Birks model. Such analysis was performed for sets (A-F) of simulated electrons. In Figure 6.8 electron-ion recombination factor is plotted for electromagnetic showers. The average value of $R = 0.67 \pm 0.01$ was obtained.

The evaluation of ξ and relative corrections are reported in the following chapter.

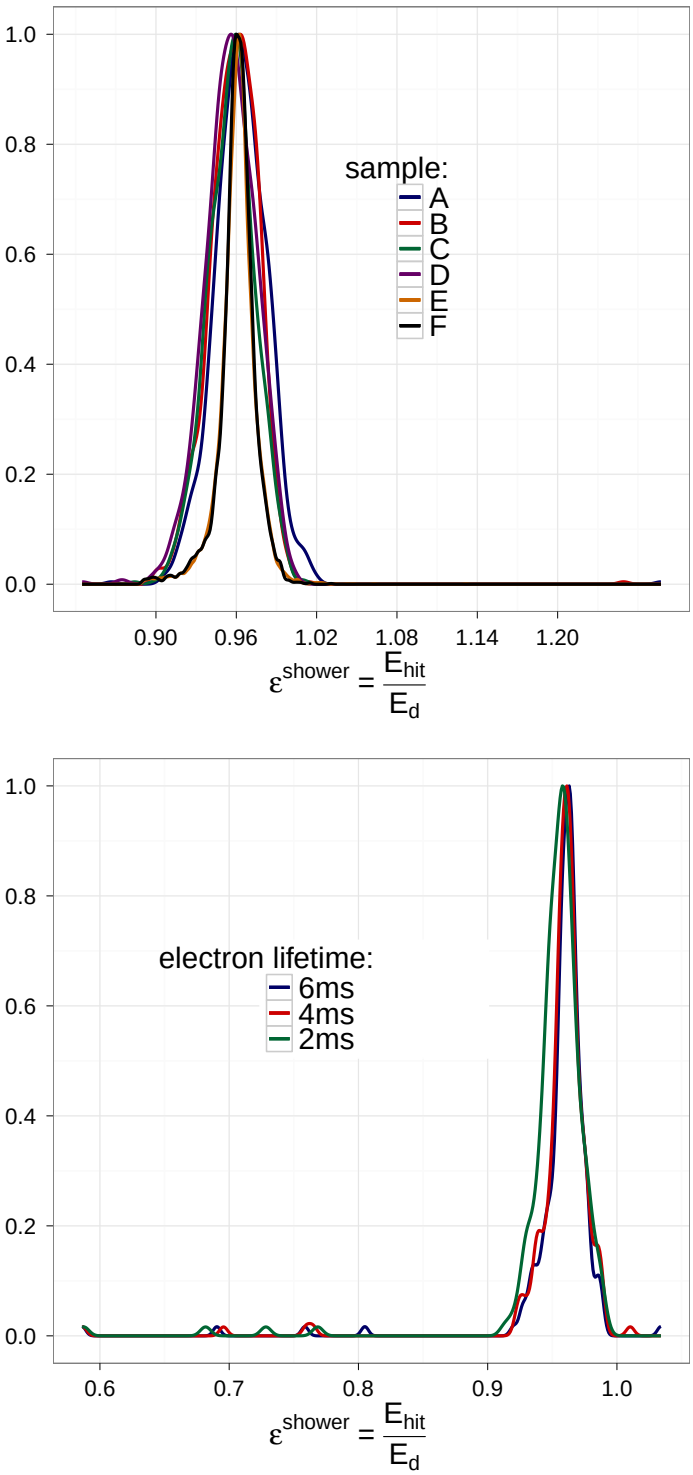

Figure 6.7: Efficiency of reconstruction on deposited energy (reconstructed/generated) for electromagnetic showers in different positions in the T600 detector (top), and for different values of the electron lifetime (bottom).

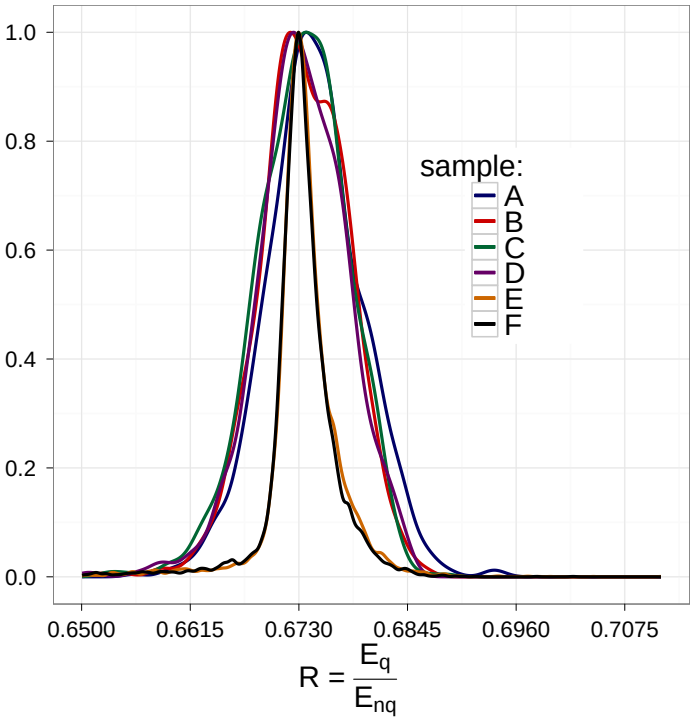

Figure 6.8: Electron-ion recombination factor obtained from Monte Carlo electrons simulated in the ICARUS detector.

Chapter 7

Electromagnetic Shower Containment

The most challenging correction to the reconstruction of energy of electromagnetic showers come from its containment within the fiducial volume of the ICARUS T600 detector. Electromagnetic showers can extend in LAr up to more than 1.5 m in the energy range of the interest (∼100 MeV to few GeV). Consequently, it is not sufficient to know the point where the shower starts, but it is of equal importance to know in which direction the shower develops and the profile of its longitudinal development.

7.1 Monte Carlo Data

A new sample of Monte Carlo data sets (see Table 7.1) were generated with FLUKA. Electromagnetic showers were initiated by electrons with momenta 0.1 - 1.5 GeV/c, at different distances from the detector wall (1 - 20 X_0, where X_0 is radiation length equal 14 cm in LAr).

sample	p [GeV/c]	directional distance [X_0]	angular distribution
E	0-3	all	isotropic
G	0.1, 0.2, 0.4, 0.5, 1.0, 1.5	1-20	parallel to cathode and anodic plane

Table 7.1: Generated e^- Monte Carlo data sets used during the analysis of the containment of electromagnetic showers in the ICARUS T600 detector. Directional distance is defined in section 7.3.

7.2 Electromagnetic Showers Parameters

Longitudinal development of electromagnetic shower in homogeneous media had been studied analytically by Rossi [42] and Longo, Sestili [43]. An important result of the calculations using "Rossi Approximation B" is that longitudinal shower moments are equal in different materials, provided one measures all lengths in units of radiation length (t=distance/X_0) and energies in units of the critical energy (E_c). The start of the shower is defined by the space point, where the first electron or positron from a bremsstrahlung process occurs.

The "center of gravity" of an electromagnetic shower (t_{med}) and the depth of its maximum (L_{max}) can be calculated from the shape parameter α and the scaling parameter β according to

$$t_{med} = \frac{\alpha}{\beta}, \tag{7.1}$$

$$L_{max} = \frac{\alpha - 1}{\beta}. \tag{7.2}$$

Therefore, if one finds two out of the three parameters α, β, L_{max}, the longitudinal shower profile $P_L(E,t)$ of a shower with energy E is determined as follows [42]:

$$P_L(E,t) = \left\langle \frac{1}{E}\frac{dE(t)}{dt} \right\rangle = \frac{(\beta t)^{\alpha-1}\ \beta\ e^{-\beta t}}{\Gamma(\alpha)}. \tag{7.3}$$

The longitudinal profile describes the energy deposition density (normalized by the energy of the primary particle) along the main axis of the shower. Eq. (7.3) is valid for energies significantly higher than the critical energy in LAr (E_c = 31 MeV). The LArIAT (Liquid Argon in a Test Beam) Collaboration [50] extensively studied electromagnetic showers in LAr at different incident photon energies from 0.5 to 4 GeV and the longitudinal distributions of E_{nq} have been evaluated for each photon energy. Combining results from the simulation at different energies, they found that

$$\alpha = 0.62\ ln\left(\frac{E}{E_c}\right) - 0.76, \tag{7.4}$$

and

$$L_{max} = \Big[1.07\ ln\left(\frac{E}{E_c}\right) - 1.13\Big] X_0. \tag{7.5}$$

Following parametrization of the electromagnetic showers given in eqs. (7.1), (7.2) and (7.3), and energy dependence of α and L_{max} found by LArIAT (eqs. (7.4) and (7.5)) one can find that it is applicable for showers of energy greater than ∼530 MeV (eq. (7.3) requires $\alpha > 1$ and then from eq. (7.4) we obtain $E/E_c \approx 17.1$, and from eq. (7.5) L_{max} is automatically greater than 0). This is clearly visible in Figure 7.6, where for $E_{mc} \leq 530$ MeV LArIAT model misbehaves. As in the ICARUS experiment electromagnetic showers of energies below 500 MeV are measured, there is a need to find a new electromagnetic showers parametrization.

For this purpose, a set of Monte Carlo simulations of different momenta range (100 MeV/c to 1.5 GeV/c) were used (set G in Table 7.1).

The longitudinal dE/dt distributions for different electromagnetic

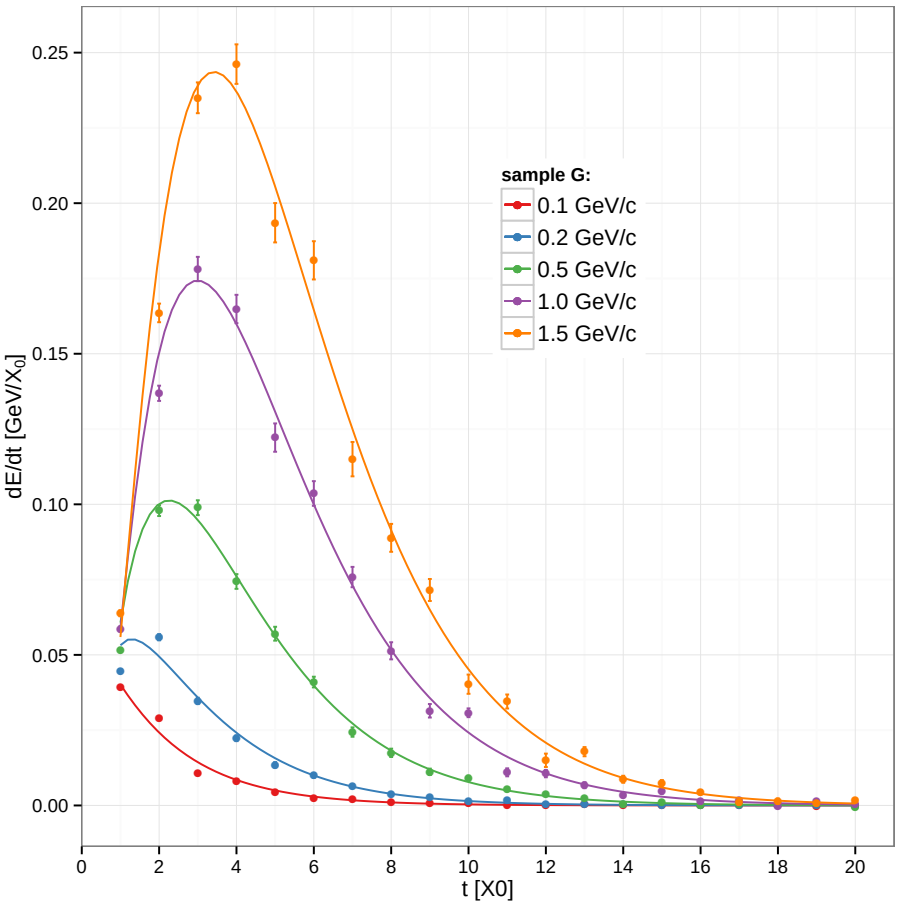

Figure 7.1: Longitudinal profile for electromagnetic showers initiated by electrons of different momenta (0.1 GeV/c to 1.5 GeV/c).

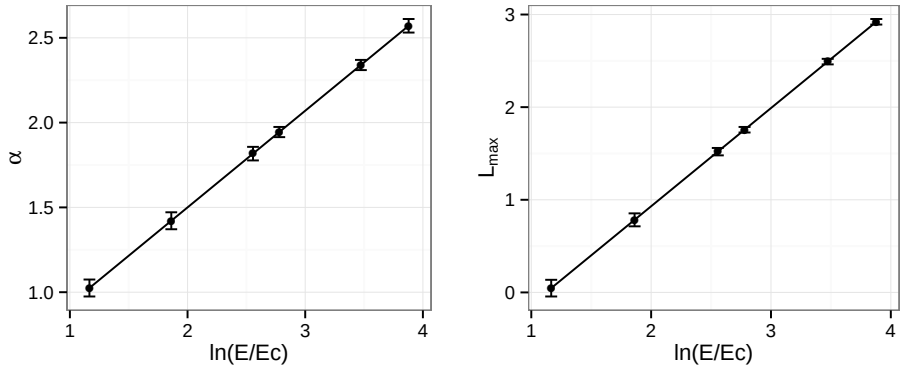

Figure 7.2: Shape parameter α and the depth of maximum L_{max} of the electromagnetic shower as function of electromagnetic shower energy.

showers, obtained from the simulations are presented in Figure 7.1. With these simulations it was possible to study how the values of shape parameter, scaling parameter and the maximum of the shower depend on the energy. The solid line represents a fit, obtained with parameters α and L_{max}, which values are displayed Figure 7.2.

The following energy dependence of α and L_{max} parameters have been obtained:

$$\alpha = (0.57 \pm 0.01)\ ln\left(\frac{E}{E_c}\right) + (0.36 \pm 0.03), \tag{7.6}$$

$$L_{max} = \Big[(1.06 \pm 0.02)\ ln\left(\frac{E}{E_c}\right) - (1.19 \pm 0.05)\Big] X_0. \tag{7.7}$$

The α and L_{max} values found by LArIAT are close, but not identical with eqs. (7.6) and (7.7). This is probably due to the low energy range studied by the author of this thesis (0.1 to 1.5 GeV), with respect to eq. (7.4) and (7.5) obtained for energy of electromagnetic showers between 0.5 to 4 GeV.

7.3 Directional Distance to the Wall

For further analysis of electromagnetic showers it will be useful to define the quantity *directional distance to the wall* K, as the distance to the wall along the direction of the shower. The difference between K and the shortest distance to the wall is illustrated in Figure 7.3.

Directional distance is measured along a line starting at the point where the first electron or positron bremsstrahlung process occurs followed by a shower, up to the wall of the detector, whereas the *distance to the wall* is defined as a shortest distance between starting point of the cascade and the wall of the TPC.

To reconstruct the directional distance K, a manual procedure is applied. First, one finds a vertex where the electromagnetic shower starts. This point need to be clearly visible in at least two views. The cascade is relatively narrow in the first radiation lengths of its development with most particles contained in a dense central core. This allow to reconstruct a 3D track that will create a shower axis. The reconstructed shower axis is then extrapolated up to the wall.

To check the accuracy of the reconstruction of directional distance to the wall K, a sample of 169 Monte Carlo events (from sample E) was used. The K values were manually reconstructed and compared with MC truth value. Resulting scatter plot together with histogram is shown in Figure 7.4. The difference between Monte Carlo *truth* and reconstructed values of K is on average -7±30 cm. The relevant spread is introduced by the manual procedure of reconstruction of K.

7.4 Shower Containment - Special Case

The shower containment factor ξ, was studied using the Monte Carlo data set G (see Table 7.1). It is important to note that the direction of simulated electrons was perpendicular to the front wall. Therefore, for what concerns the shower containment, only the longi-

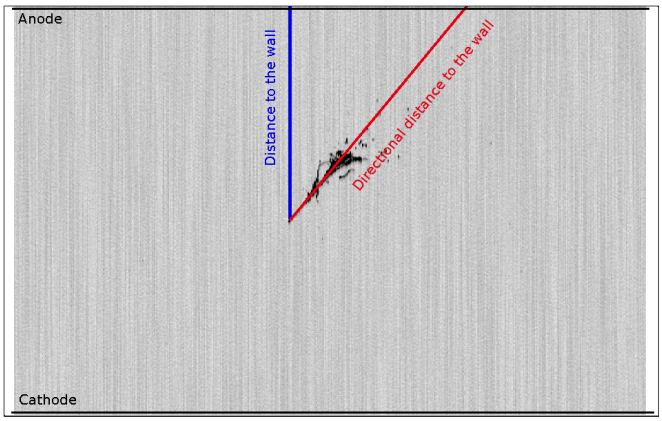

Figure 7.3: Illustration of directional and closest distance to the wall for electromagnetic showers.

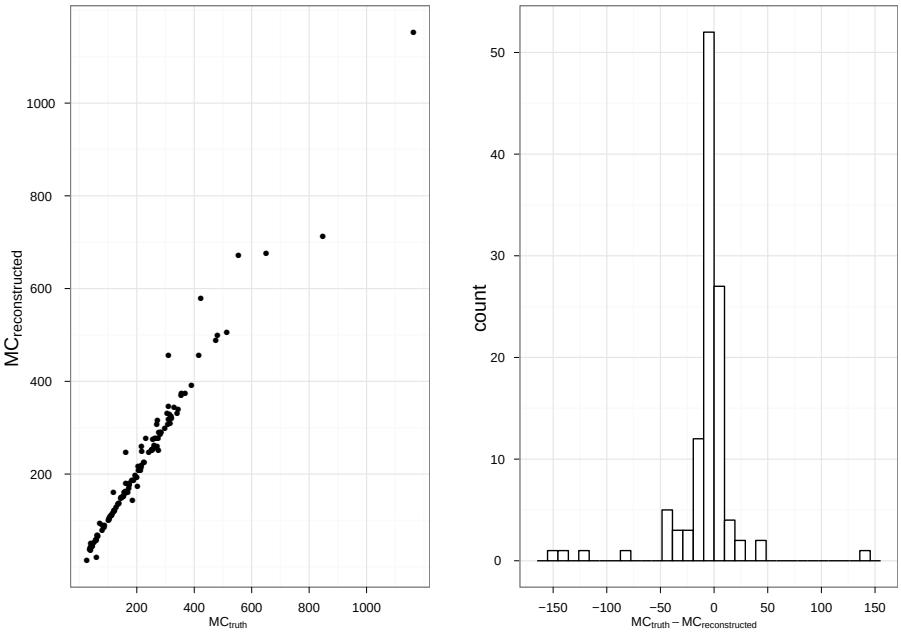

Figure 7.4: Reconstruction precision of the directional distance to the wall obtained from Monte Carlo events (sample E) reconstructed in the same way as collected CNGS events.

tudinal profile is relevant.

In Figure 7.5, factor ξ is shown for electrons of different momenta generated in a fiducial volume of the detector as a function of distance from detector wall (in X_0). The solid lines come from the numerical integration of eq. (7.3) with $\alpha(E)$ and $\beta(E)$ extracted by the fit on FLUKA data (eqs. (7.6) and (7.7)).

About 90% of the showers generated by 100 MeV/c (1.5 GeV/c) electrons have an average directional distance of 56 cm (126 cm), corresponding to 4 X_0 (9 X_0) in radiation length units (Figure 7.5).

7.4.1 Shower Containment Correction

In the special case of shower perpendicular to the wall, as shown in Figure 7.5, ξ can be defined as

$$\xi(E, K) = \int_0^K P_L(E, t)\ dt, \tag{7.8}$$

where K is the directional distance to the wall in units of X_0 and $P_L(E, t)$ is the longitudinal profile defined in eq. (7.3). From eq. (7.8)

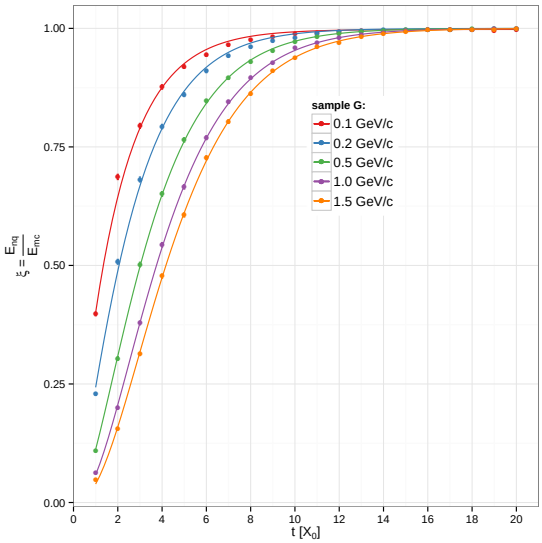

Figure 7.5: Shower containment factor ξ for simulated electromagnetic showers originating from electron interactions with different momenta, as function of radiation distance. Points indicate average normalized shower energy at the corresponding distance (in units of X_0), whereas the line refers to the cumulative longitudinal shower profile defined in eqs. (7.3), (7.6) and (7.7).

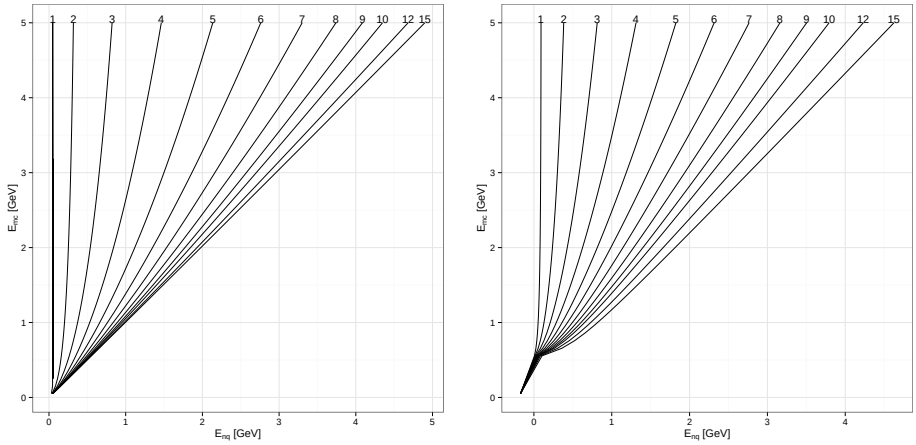

Figure 7.6: E_{mc} curves versus E_{nq} ones for different values of K according to eq. (7.9) using respectively, longitudinal profile best fit based on FLUKA (left) or LArIAT parameters (right).
(numbers above the lines correspond to 1-15 X_0).

$E_{mc}[GeV]$	0.1	0.2	0.4	0.5	1.0	1.5
E^*_{mc} [GeV]	0.099	0.198	0.398	0.498	0.999	1.499
sd(E^*_{mc}) [GeV]	0.001	0.001	0.003	0.002	0.007	0.012

Table 7.2: Reconstructed E_{mc} for different shower energies at different K: each value is the mean of the points shown in Figure 7.5 and reconstructed as described in the text. The standard deviation *sd* of the mean values grouped by K is shown.

deposited energy, E_{nq} can be extracted

$$E_{nq} \;=\; E_{mc}\,\xi(E_{mc}, K). \tag{7.9}$$

In a case of real data, E_{mc} is unknown, while E_{nq} and K are given. It is then required to invert eq. (7.9) in order to calculate E_{mc}. Figure 7.6, left, shows the E_{mc} curves versus E_{nq} ones for different values of K in the range from 1 to 15 X_0. It is important to notice that all the curves (with $K > 3\ X_0$) are clearly monotonic in the energy range of interest, therefore eq. (7.9) can be inverted numerically with a single result (while in Figure 7.6 it can be seen that the LArIAT approximation produces nonphysical results for showers with energy below ∼600 MeV).

A first approach is to evaluate the zeroes of $E_{nq} - E_{mc}\,\xi(E_{mc}, K)$ as a function of E_{mc} using well known root finding algorithms such as bisection or Newton-Raphson [51].

Another method is based on an iterative approach

$$E^{i+1}_{mc} \;=\; \frac{E_{nq}}{\xi_{corr}(E^i_{mc}, K)} \qquad with \qquad E^0_{mc} = E_{nq}. \tag{7.10}$$

The second method was found to be more stable against the fluctuations, and less sensitive on the monotonic requirement, which can be broken for small values of shower containment. In any case, the following two cuts are applied to avoid fluctuations of events where the correction is bigger than a factor of 10:

- $E_{nq} > 10$ MeV. Considering the typical hit energy (1.7 MeV) this cut suppresses events for which the corrected energy would be affected by strong quantization/statistical effects,
- $K > 3\ X_0$. For photons energy in the region of interest it corresponds to a minimal containment of 10%. This cut reduces the fiducial volume for the analysis to about 400 tons (90% of the original mass).

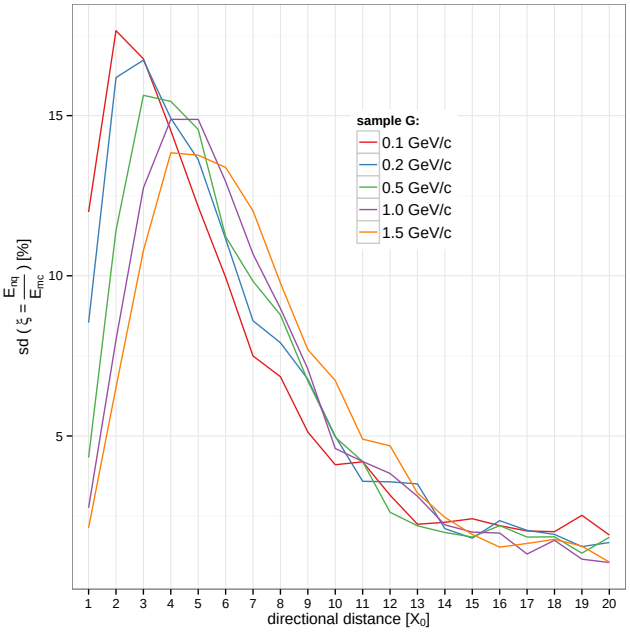

Figure 7.7: Statistical fluctuations of the shower containment for simulated data set G: each point represent the standard deviation of E_{nq}/E_{mc} of a sample of 1000 electron-induced electromagnetic showers with given starting energy and fixed distance to the wall. The showers were generated orthogonal to the wall.

In Table 7.2 the shower containment corrections according to eq. (7.9) are shown: the average reconstructed value of E^*_{mc} is always very close to the expected value.

In Figure 7.7 the statistical fluctuations of the electromagnetic shower containment are shown for a given initial e^- energy at fixed distance to the wall. In case of showers started by gammas a further dispersion would be present, due to the conversion distance of the initiating γ.

It is relevant to notice that the significant dispersion of the deposited energy (in excess of 15% even after 3 X_0) is an intrinsic property of the shower process and the containment correction can not reduce it: the role of the proposed algorithm is to eliminate the bias producing a symmetric distribution centered on 1.

7.4.2 Shower Containment - General Case

In the realistic case, the showers are almost never perpendicular to the detector wall, therefore the previous correction has to be reconsidered. In principle, a three dimensional (3D) model of the shower could be developed to estimate, event by event, the overlap between the shower and the ICARUS detector active volume. However, it is opinion of the thesis author, that the complexity of a 3D model and the related uncertainties could produce a result not better than the solution proposed in this section. In Figure 7.8 it is shown that for showers not perpendicular to the wall, the correction effect is of second order and can be neglected in the first approximation.

In Figure 7.9 and Figure 7.10, the performances of the energy correction algorithm are shown, for the simulation data set E (electrons uniformly distributed in the detector with $0 < E_{mc}[GeV] < 3$). The plots are presented in four panels according to four used energy estimators:

- E_{nq} is the reconstructed energy (deposited in active volume), corrected for hit finding losses and e^--ion recombination, but not for shower containment. This quantity significantly underestimates the shower energy.

- E_{corr} is obtained by numerical inversion of eq. (7.10) as described earlier; this approach fixes the underestimation due to the partial shower containment.

- E_{corr}^{LArIAT} is calculated with the same algorithm used for E_{corr} but with the LArIAT longitudinal profile parameters (eqs. (7.4) and (7.5)) instead of the best fit obtained on the FLUKA simulations (eqs. (7.6) and (7.7)).

- E_{shower} is obtained by a modification of eq. (7.9) to

$$E_{nq} = E_{shower}\ \xi_{corr}^{\frac{2}{3}}(E_{mc}, K) \quad \rightarrow \quad E_{shower} = E_{nq}/\xi_{corr}^{\frac{2}{3}}$$

  where ξ_{corr} is calculated with the same algorithm used for E_{corr} (eq. (7.10)).

  The reason for which the best correction happens at $2/3$ is not clear, numerical simulations of the containment prefer values in the range 0.5-1.

The dispersion of the corrected energies (for both E_{corr} and E_{shower}) is compatible to what was described in the previous section and depends mostly on the statistical fluctuations during the evolution of the shower in the ICARUS T600 volume.

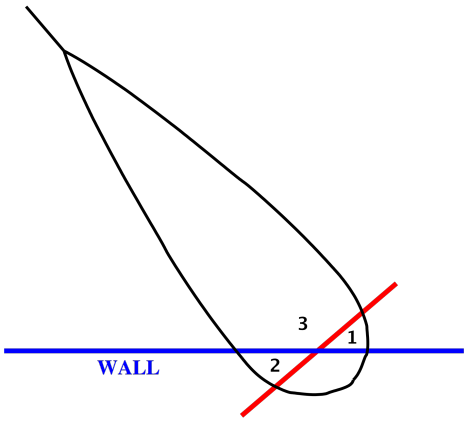

Figure 7.8: Sketch of an electromagnetic shower shape intersecting the wall of the detector; the red line represents the E_{corr} containment approximation. E_{nq} is defined as 3 + 1 volumes, while E_{corr} would require 3 + 2 volumes to reproduce correctly E_{mc}.

E_{shower} is an empirical correction tuned on MC, not differently from other corrections that are based on FLUKA. In this thesis, the author consider E_{shower} to provide the most accurate energy reconstruction of electromagnetic showers.

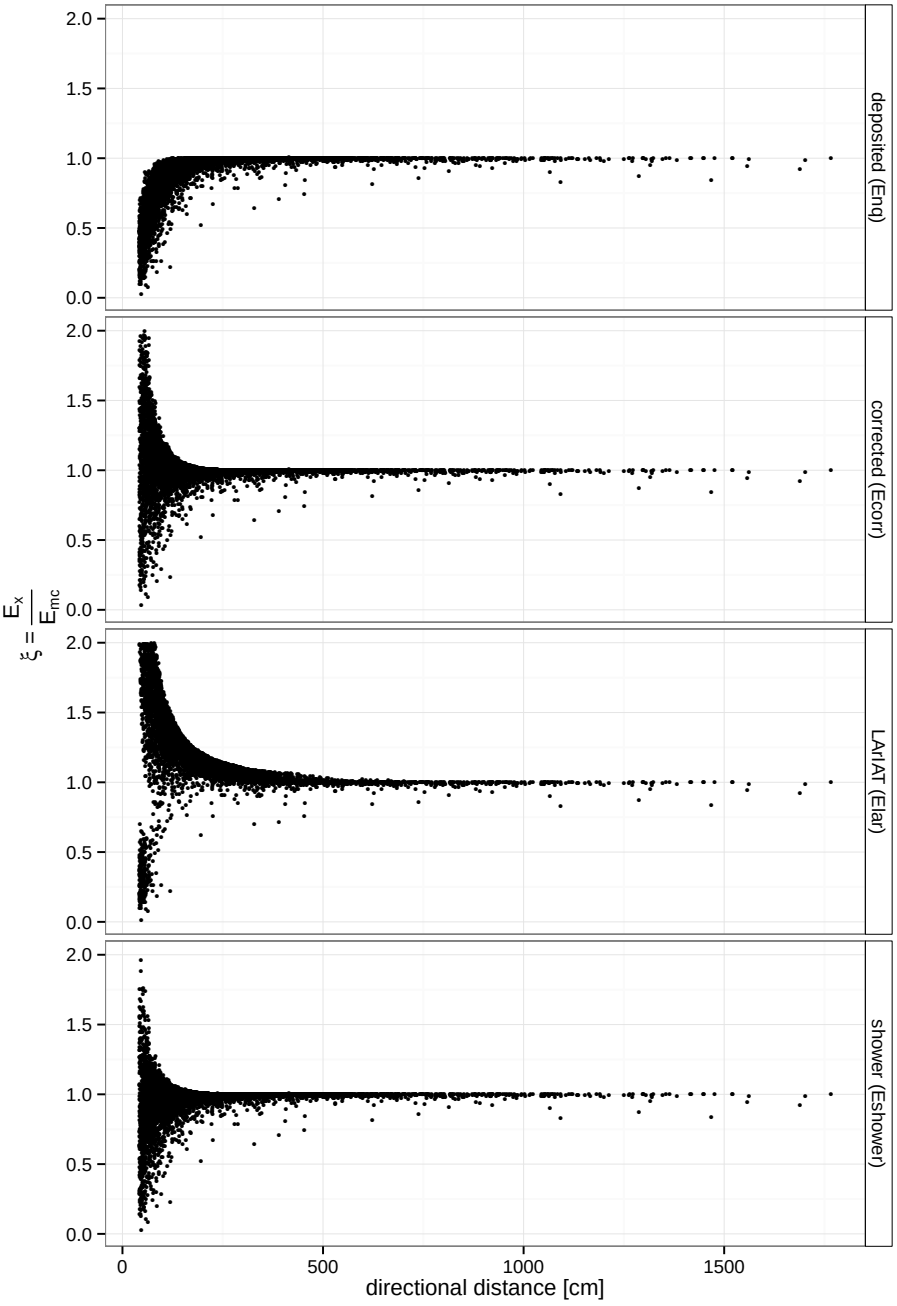

Figure 7.9: Shower containment factor $\xi_x = \frac{E_x}{E_{mc}}$ for the different energy correction approaches discussed in the text (x = nq, corr, lar, shower).

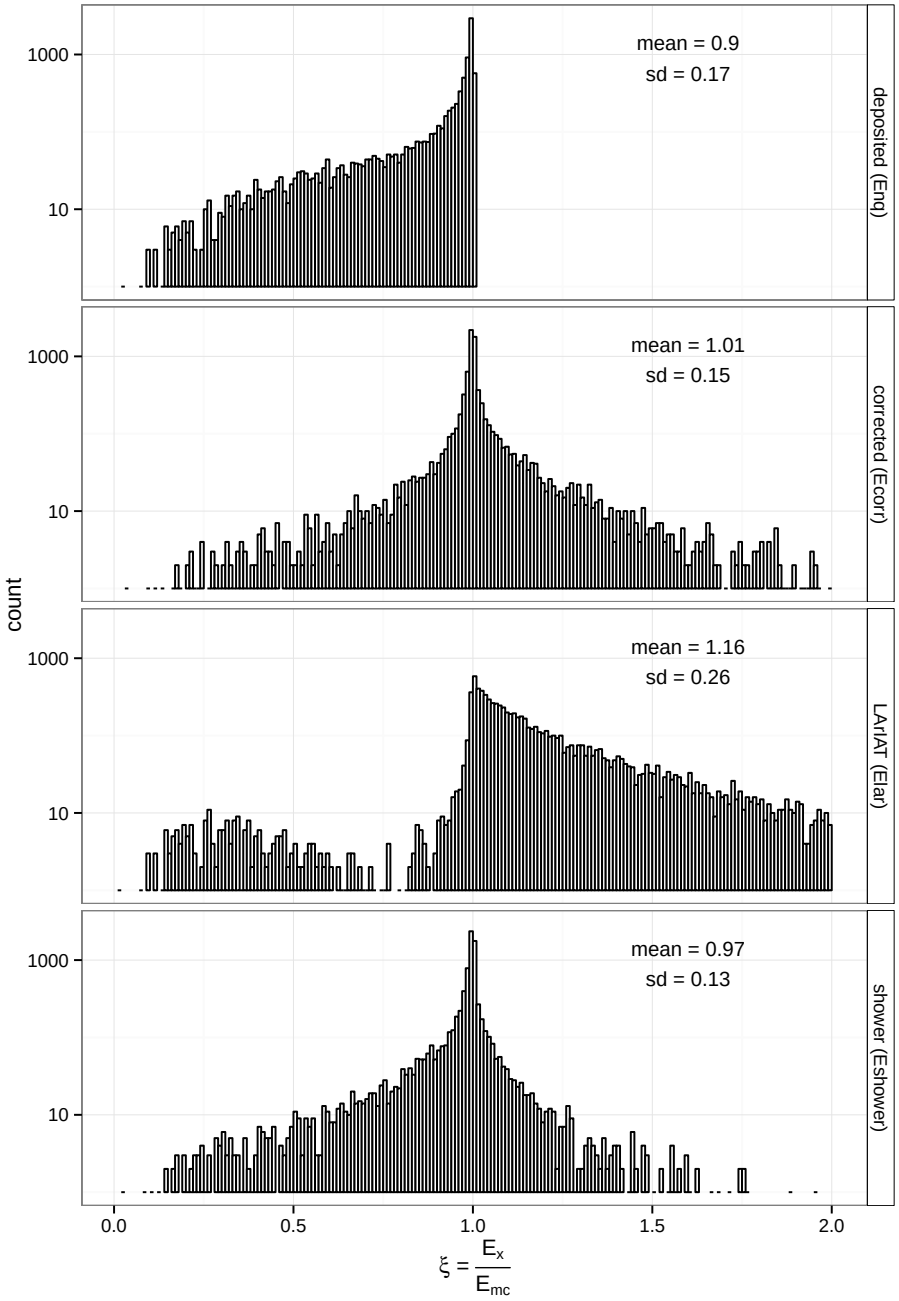

Figure 7.10: Effective $\xi_x = \frac{E_x}{E_{mc}}$ for the different energy correction algorithms discussed in the text (sd denotes standard deviation, x = nq, corr, lar, shower).

Chapter 8

Gamma Electromagnetic Showers - Results from T600 LAr TPC

ν_μ CC CNGS data collected in 2011 and 2012 by the ICARUS detector was chosen for the analysis of electromagnetic showers and neutral pions. Charged current ν_μ interactions are identified with the requirement of a track exiting the primary vertex and traveling at least 250 cm (interaction length in LAr being $\sim$85 cm) in the detector. In Table 8.1, the number of neutrino events and ν_μ CC interactions collected by the ICARUS detector are shown.

In the first step of the analysis, a visual scanning of all ν_μ CC events was performed by the author of this thesis. In order to be selected, for the analysis of electromagnetic showers, an event had to fulfill following requirements:

1. clearly localized two vertices inside the fiducial volume of T600: one indicating γ production point and one conversion point (e^+e^- pair production or Compton scattering) in at least two views,

2. charged tracks starting from the conversion vertex, fully consistent over at least 8 wire hits (2.5 cm) and subsequently building up into a shower,

3. visible spatial separation from other ionizing tracks within 150 mrad in the immediate vicinity of the conversion vertex in at least one of the two transverse views ($\pm 60^\circ$), except for short proton like recoils due to nuclear interactions.

year	pot (10^{19})	ν events	ν_μ CC events
2011	3.4	1137	713
2012	3.2	1142	574
total	6.6	2279	1287

Table 8.1: Numbers of data collected by the ICARUS T600 detector during 2011 and 2012 campaigns.

8.1 Conversion Distances

The radiation length X_0 in LAr is equal to 14 cm, corresponding to a γ mean conversion length X_γ of 18 cm. An extended studies of conversion distances was done using both, Monte Carlo and events coming from ν_μ CC CNGS data. The Monte Carlo study was done with a sample of photons generated with FLUKA, uniformly and isotropically distributed in the fiducial volume, and with flat energy distribution up to 600 MeV.

On the top panel of Figure 8.1, the distribution of energy for simulated gammas is shown, while the density plot of conversion distances versus photon energy is presented in the central panel. As shown by the color saturation in the density plot and as expected, for lower energies conversion distances are on average longer, while for higher energies, on average they are shorter. The black line is the result of a two-dimensional fit of X_γ as function of γ energy. It is obtained by an unbinned likelihood fit defined as:

$$L(\Theta) = \prod_i \frac{e^{\frac{-D_i}{X_\gamma(E_i,\Theta)}}}{X_\gamma(E_i,\Theta)}, \tag{8.1}$$

where E_i and D_i are the energy and the conversion distance of the i-th gamma, respectively, while $X_\gamma(E_i,\Theta)$ is the mean conversion distance as function of energy, within a *const+exp* model:

$$X_\gamma(E,\Theta) = X_\gamma(E,c,b,t) = c + b\,e^{-E/t}. \tag{8.2}$$

The obtained best fit parameters are following:

c	18.3 ± 0.7
b	6.9 ± 0.9
t	0.19 ± 0.06

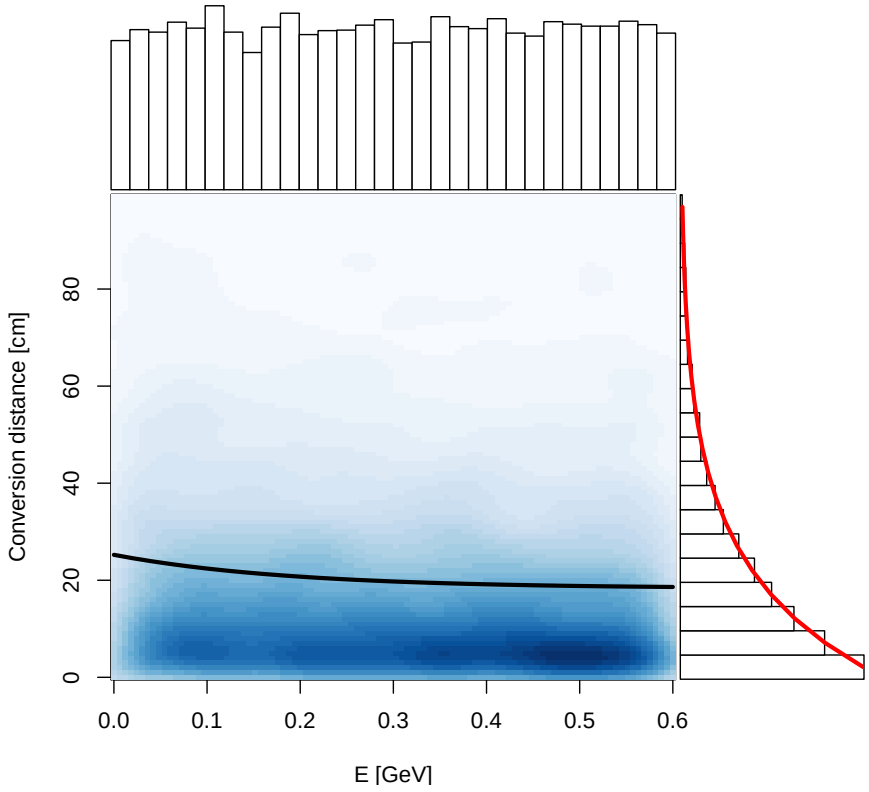

Figure 8.1: Density plots of photon conversion distances as a function of γ energy (MC simulations).

Above 400 MeV of gamma energy, the mean conversion distance is constant with the value of $\sim$ 18 cm (as expected), while for low energies it increases reaching values of about 24 cm.

On the right panel in Figure 8.1, the histogram of overall conversion distances is shown. The fit of the histogram with an exponential model returns a X_γ of $\sim 21.4 \pm 0.2$ cm and a reduced $\chi^2 = 0.98$ (with 18 degrees of freedom). This value is affected by the large quantity of low energy photons populating the histogram.

The data from ICARUS T600 ν_μ CC CNGS interactions were divided into two subsets depending on the availability of the energy reconstruction. During the manual scanning most of the interactions were too complicated to define a clear shower region and therefore reconstruct the photon energy.

- In Figure 8.2, 286 events for which the energy is reconstructed are shown with the same style as the Monte Carlo data. From the top panel it is clear that there is a non uniformity in the gamma energy peaked at $\sim$200 MeV. From both, the scatter

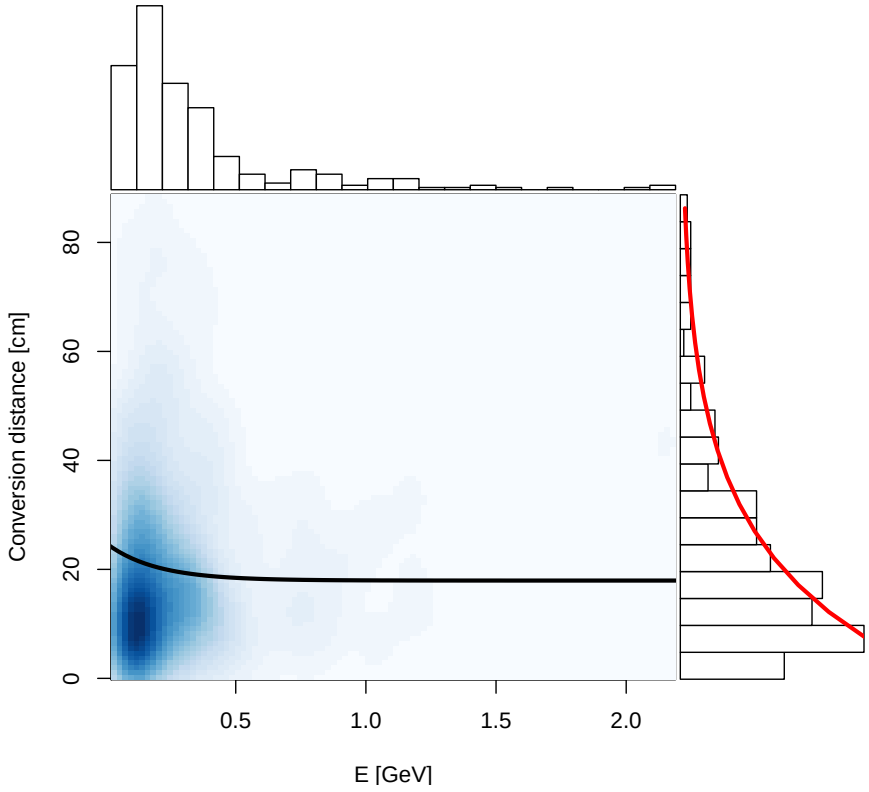

Figure 8.2: Density plots of photon conversion distances as a function of γ energy (ICARUS CNGS ν_μ CC events).

plot and the right histogram, it can be seen that a large fraction of events with low conversion distances is not present. Consequently, the likelihood fit $L(\theta)$ is modified to include only events with conversion distance greater than 10 cm. Due to the small and non uniform sample, the unconstrained fit returns nonphysical results. However, an asymptotic X_γ estimation can be obtained by a constrained likelihood. In fact, when fixing to the Monte Carlo best fit the parameters a and b, representing the low energy dependence of X_γ, the high energy mean conversion distance converges to $c = 18.0 \pm 1.4$ cm.

The fit on the histogram on the right panel returns a mean conversion distance of 21 ± 2 cm with a reduced χ^2 of 1 (and dof $= 14$) for events with conversion distance greater than 10 cm.

- In Figure 8.3, 804 events, for which the shower energy was not reconstructed, are shown. Even for this data set, a clear absence of low conversion distance events is visible. Therefore, the fit is performed only for events above 10 cm. The resulting mean

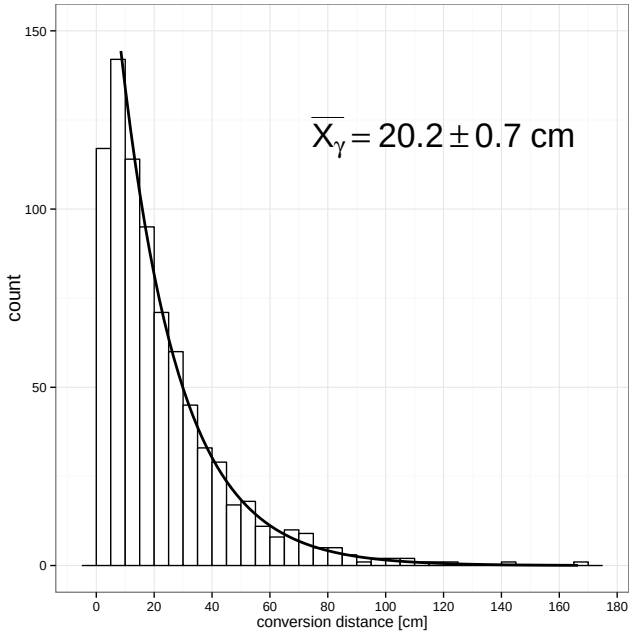

Figure 8.3: Photon conversion distances distribution with fit for events without reconstructed shower energy.

conversion distance is equal to 20.2 ± 0.7 cm with a reduced χ^2 of 0.24 (and dof = 8).

The absence of events with low values of gamma conversion distance in real data is not clear. It may be an effect of the manual scanning procedure. In fact, for higher energy events and short conversion distance, the identification of a clear shower region is not always possible. A hint towards this explanation is given by the fact, that the absence of low conversion events is more pronounced for higher energy gammas, as can be seen in the scatter plot of Figure 8.2.

8.2 Energy Losses for Ionization

In LAr a minimum ionizing particle (m.i.p.) should deposit about 2.1 MeV/cm. For high energy photon interactions, the ionization density in the first 2.5 cm of the track is approximately equal to 2 m.i.p.'s, corresponding to e^+e^- pair creation [52]. A concurring process is Compton scattering, in which a single m.i.p. is produced. This can lead to the γ/e^- misidentification. However, the Compton cross section becomes negligible with respect to the pair production above few hundreds MeV.

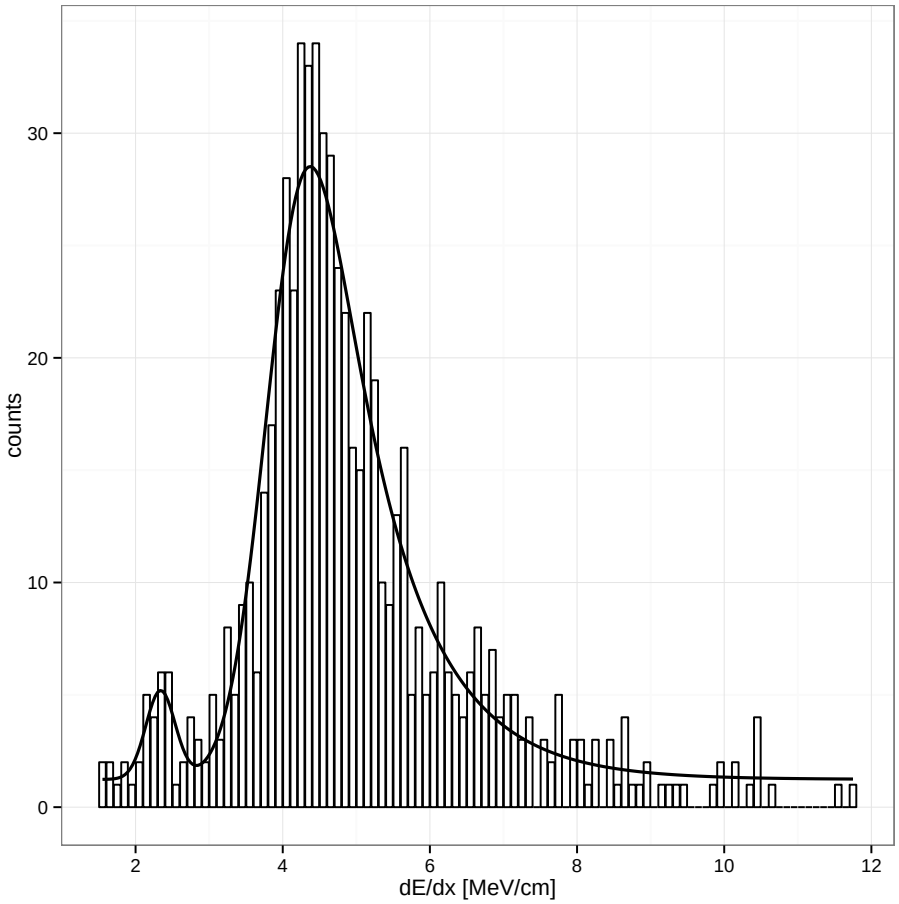

Figure 8.4: dE/dx distribution in the first 2.5 cm of the electromagnetic shower: two peaks are visible corresponding to 1 m.i.p. at 2.31 MeV/cm and 2 m.i.p. at 4.4 MeV/cm. The fitting function is a modified gaussian to take into account showers already started in the first 2.5 cm: the chi2 is 78.5 with 70 dof.

Figure 8.4 shows dE/dx distribution for electromagnetic showers from manually scanned events from ν_μ CC CNGS data. Two clear peaks are visible. The 2 m.i.p. is fitted with an Exponentially Modified Gaussian (EMG, a gaussian convoluted with an exponential), to take into account the higher dE/dx of events already showering in the first 2.5 cm (while for the lower peak, given the low statistics, a simple gaussian fit was used). The dE/dx values of 2.31 ± 0.04 MeV/cm and 4.40 ± 0.04 MeV/cm, were obtained for 1 and 2 m.i.p., respectively. The result for 2 m.i.p. with EMG is compatible with a gaussian fit in the region below 5 MeV/cm. The ratio between the two peaks is around $4 \pm 2\%$, compatible with the Compton/pair production

cross-sections in the energy range of interest (few hundreds of MeV).

The extended fit (with the exponential tail) is useful to estimate the e^-/γ discrimination in LAr TPC. In ICARUS the extraction of ν_e CC signal events from ν_μ NC background with π^0 production is based on the correct identification of e^-. Single γ's coming from π^0 decay (where the second photon escaped the detector or two γ's overlap) can be misidentified for e^- leading to the wrong classification of the event.

In Figure 8.5 the cumulative curves for electron and gamma distributions are shown as function of dE/dx: the model used for the quantile generation is based on the best fit values from Figure 8.4.

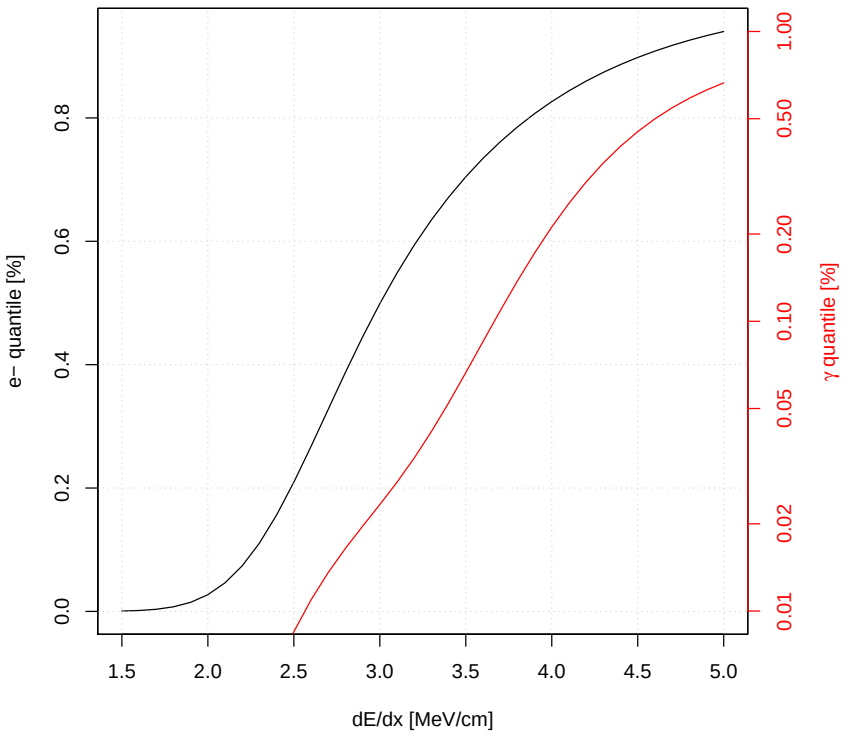

Figure 8.5: Cumulative curves of dE/dx for electrons (black) and gammas (red): the quantiles were generated from exponentially modified gaussian using the best fit parameters obtained from Figure 8.4. The γ quantile is plotted in a logarithmic scale to show the contamination of the pure e^- sample; the 4% 1 m.i.p. contamination of Compton interaction is the cause of the small kink at about 3.5 MeV/cm.

Moreover, the same exponential tail found for the 2 m.i.p. peak is applied to the 1 m.i.p. distribution (which is probably an overestimation). From the plot it can be seen that selecting events with $dE/dx \leq 3.4$ MeV/cm the remaining gamma events are less than 5% preserving a cut efficiency bigger than 65% for electrons.

Chapter 9

Analysis on Neutral Pions

In this chapter, the neutral pion analysis will be described. A sample of ν_μ CC CNGS data collected by ICARUS T600 detector in 2011-2012 campaigns was used. A typical ν_μ CC CNGS event with a π^0 decay is shown in Figure 9.1.

Neutral pion decays into $\gamma\gamma$ in 98.8% of the cases, and only 1.2% follows the Dalitz decay into $e^+e^-\gamma$. The mass of π^0 particle is equal to 134.9766 $\pm$ 0.0006 MeV/c^2 [18]. Another neutral meson, η, with the mass of 547.862 $\pm$ 0.018 MeV/c^2 [18] decays in the $\gamma\gamma$ channel with a branching ratio of 39.2%.

To find the π^0 events, the author of this thesis performed a visual scanning of the data (1287 ν_μ CC events, see Table 8.1 for details) looking for [53], [54]:

- three clearly visible vertices: one indicating the meson decay and at least two vertices from the pair production, each in at least two views,
- at least two two electromagnetic showers pointing to the same vertex in at least two views,
- visible spatial separation from other ionizing tracks within 150 mrad in the immediate vicinity of the conversion vertices in at least one of the two transverse views ($\pm 60^\circ$), except for short proton like recoils due to nuclear interactions,
- energy clusters of electromagnetic showers clearly separated from each other and other tracks in Collection view.

In the following sections invariant mass reconstruction method and results obtained from the studies of T600 are presented.

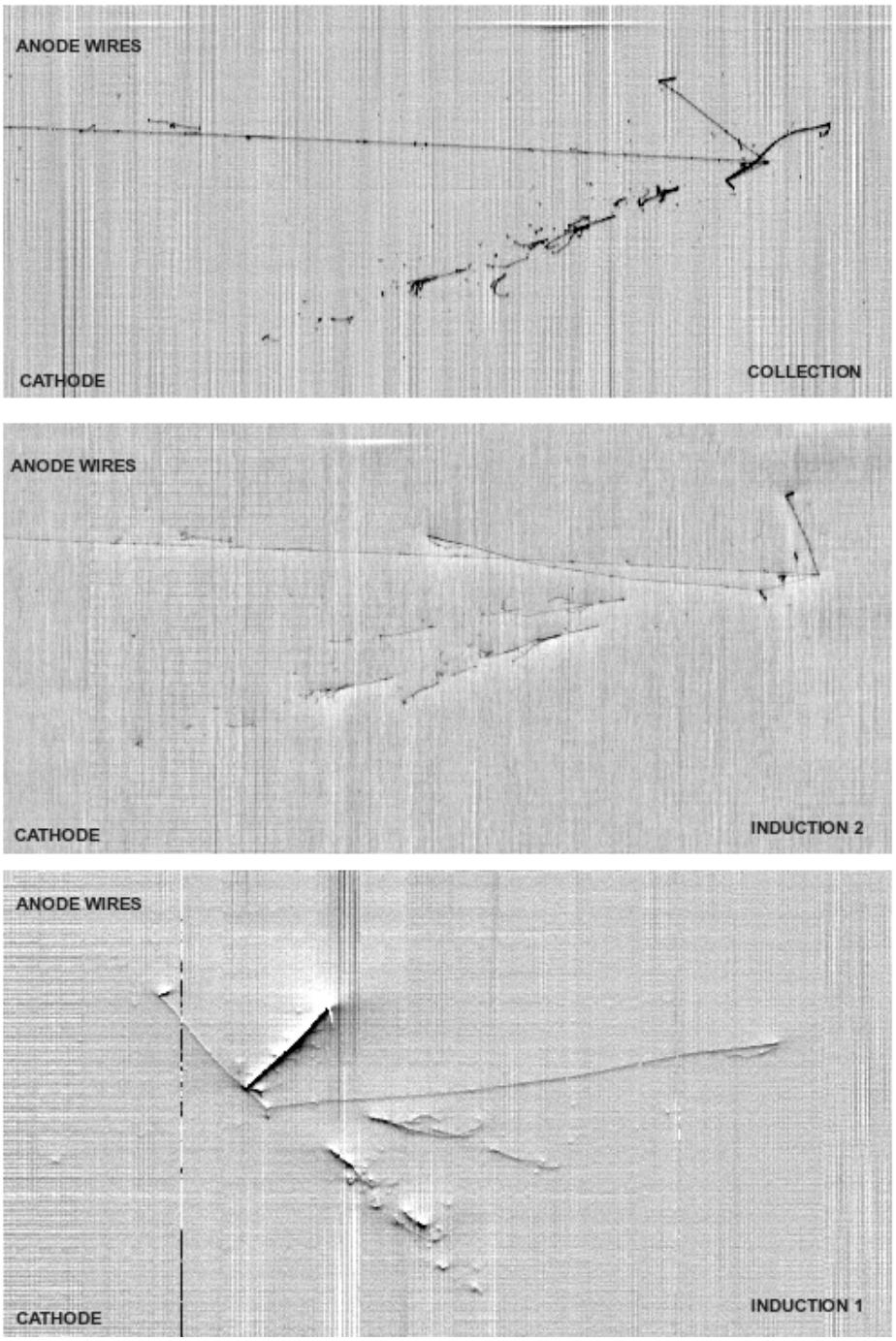

Figure 9.1: Typical ν_μ CC CNGS event with π^0 decaying into $\gamma\gamma$. Two electromagnetic showers pointing to the decay vertex are clearly visible in Induction views.

9.1 Reconstruction Method

The invariant mass is determined from quantities which are conserved during a decay. Using the energy and momentum of the decay products of a single particle, the invariant mass is equal to the mass of the particle that decayed:

$$M^2 = \Big(\sum_i E_i\Big)^2 - \Big(\sum_i \mathbf{p}_i\Big)^2, \tag{9.1}$$

where M is the invariant mass of the system, $\sum_i E_i$ and $\sum_i \mathbf{p}_i$ are the sum of the energies and of the momenta of the particles, respectively. In the case of a two body decay eq. (9.1) becomes

$$M^2 = m_1^2 + m_2^2 + 2(E_1E_2 - \mathbf{p}_1\mathbf{p}_2), \tag{9.2}$$

where m_1 and m_2 are the masses of the two particles produced in the decay. For a system of two massless particles (like in $\pi^0 \to \gamma\gamma$ or $\eta \to \gamma\gamma$) whose momenta form an opening angle θ, the invariant mass formula is reduced to the convenient expression

$$M = \sqrt{2E_1E_2(1 - cos\theta)}. \tag{9.3}$$

The accurate reconstruction of electromagnetic showers, both in energy and angle, is the key to the precise measurement of π^0/η invariant mass. The reconstruction procedures of electromagnetic showers position/direction and energy reconstruction were described in earlier chapters.

9.1.1 Effects of γ Shower Resolution

In order to study how hit loss, hit misidentification and miscalculation of θ affect reconstructed π^0 mass, a simple *toy Monte Carlo* was written. The goal was to estimate the stability of the results for the resolution effects of the detector.

A sample of π^0 events from CNGS Monte Carlo ν_μ CC was used. Three different effects, that can affect the π^0/η mass reconstruction, were simulated: energy resolution for the gamma shower, energy misidentification between the showers and resolution for the opening angle θ. All contributions were added as normally distributed noise.

For the first three plots (energy resolution and charge misidentification) the smearing has a sigma of 10 MeV that should be compared to the average hit energy equal to ∼1.6 MeV. From the plots in Figure 9.2 it can be seen that the π^0 mass expectation versus the

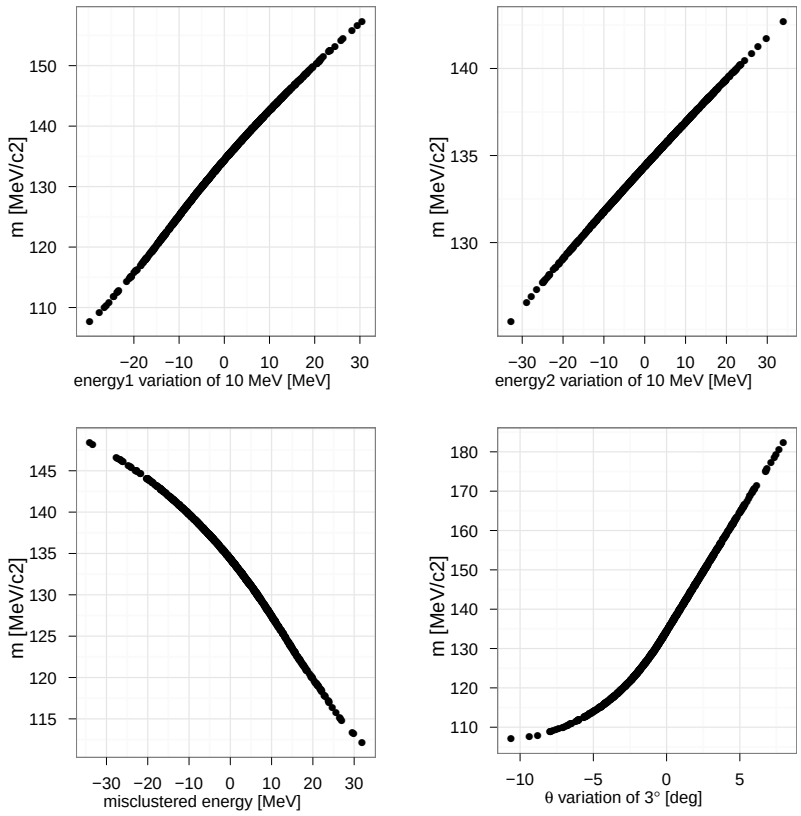

Figure 9.2: Reconstructed π^0 invariant mass dependency on variations of the physical observables. Energy 1 (2) indicates the energy of the least (most) energetic gamma shower in the π^0 decay: for each of them the plot was generated adding gaussian smearing with standard deviation of 10 MeV to the corresponding electromagnetic shower from the original data sample (CC CNGS from FLUKA).
Misclustered energy indicates a misreconstruction process, for which part of the energy from one electromagnetic shower is wrongly attributed to the other. The plot was generated by adding gaussian smearing with standard deviation of 10 MeV to the highest energy electromagnetic shower and subtracting the same quantity from the other.
The last panel shows the effect of the misreconstruction of the opening angle θ; the plot was generated by adding gaussian smearing with standard deviation of 3° to the original sample.

smearing is approximately linear. Therefore no bias is expected by the energy resolution of the γ showers reconstruction.

On the fourth plot, regarding opening angle resolution effect, a sigma of 3° was used: this uncertainty corresponds to the conversion distance of about 2.5 cm (Figure 6.4). The related plot in Figure 9.2 shows a significant nonlinearity, that can lead to an overestimation of the π^0 mass of several MeV/c^2. Therefore, it is important, in the π^0 mass fit, to verify a possible bias from short (< 5 cm) conversion distance events.

9.2 Results from T600

In this section the results of π^0 invariant mass reconstruction from data collected by the ICARUS detector during 2011-2012 campaigns

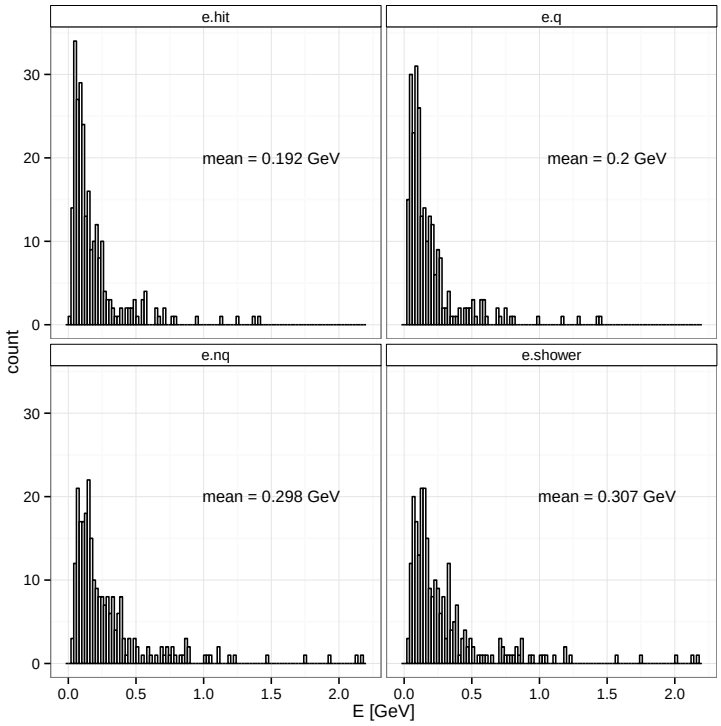

Figure 9.3: Energy distributions of gammas from π^0 decay before and after different corrections discussed in section 6.3. *e.hit* is the energy reconstructed by the ICARUS analysis software, *e.q* is an energy after applying hit finding correction, *e.nq* is the energy after recombination correction, *e.shower* is the energy including shower containment correction.

are presented.

9.2.1 Electromagnetic Showers

As discussed in previous chapters, the energy reconstruction of electromagnetic showers in ICARUS T600 is structured in a ladder of corrections (see Figure 6.5). In Figure 9.3 the energy spectrum of γ's coming from the π^0 decay in ν_μ CC CNGS is shown at the different steps of the correction. The mean value of the photon energies is ∼300 MeV, in a range between 16 MeV and 2.2 GeV. The final reconstructed value for the photon shower (E_{shower}) includes the hit corrections for the hit finding inefficiency, the ionization charge quenching, and the shower containment. In Figures 9.4 and 9.5 the effect of the shower containment correction can be seen. The changes in energy values are visible for short directional distances K. The corrections become negligible for showers fully contained in the detector. In Figure 9.5, a zoomed range 0-100 cm of K is shown.

9.2.2 Invariant Mass

During the visual scanning procedure of ν_μ CC CNGS events, 143 $\gamma\gamma$ candidates were accepted by the cuts described at the beginning of this chapter. Their reconstructed invariant mass is shown in Figure 9.6. Two clear peaks are identified.

In Figure 9.7 a gaussian fit of the π^0 peak is performed for different approaches to shower containment correction. M_x is defined as the π^0 invariant mass reconstructed with the corresponding E_x corrected energy (with x = nq, corr, shower as defined in chapter 7).

In Figure 9.8 a quantile to quantile (qq) plot[1] is shown. In the data the presence of non gaussian tails is visible. The effects of the different containment approaches on the π^0 mass reconstruction are shown in the qq plots.

As discussed in chapter 7, the E_{shower} approach produces the most symmetric and least biased results with the minimum spread of the data. The good performance of the E_{shower} approach is evident, as well, for the reconstruction of the π^0 invariant mass. In fact the qq plots for M_{shower} present the smallest deviation from the straight line,

[1] A quantile to quantile plot is an indication of how well data are described by a theoretical distribution (gaussian in this case). The theoretical quantile is estimated as the integral of a gaussian distribution with mean and sigma extracted by a unbinned maximum likelihood fit on the data, while the experimental quantile is the normalized accumulation of the statistical sample. If the null hypothesis is verified the qq plot should be a straight line.

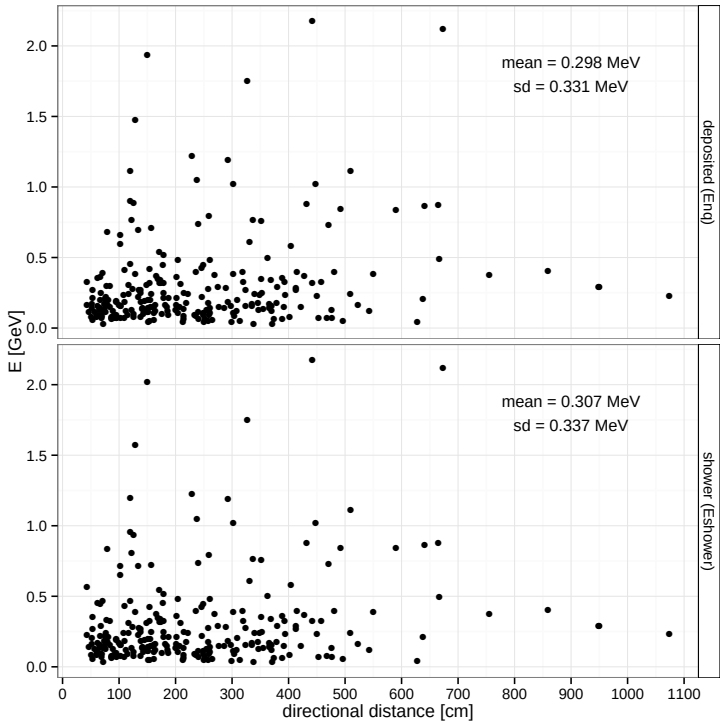

Figure 9.4: Scatter plots of photon energy for uncorrected E_{nq} and corrected E_{shower} values in a function of the directional distance K. The mean values and standard deviations (sd) are indicated.

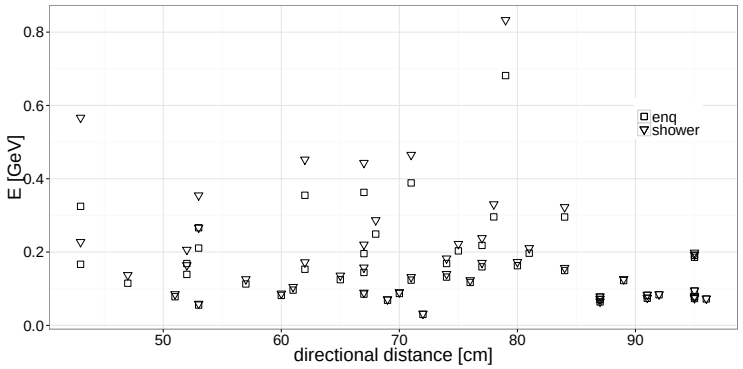

Figure 9.5: Zoom view of scatter plot in Figure 9.4 in a range of directional distance K between 0 and 100 cm.

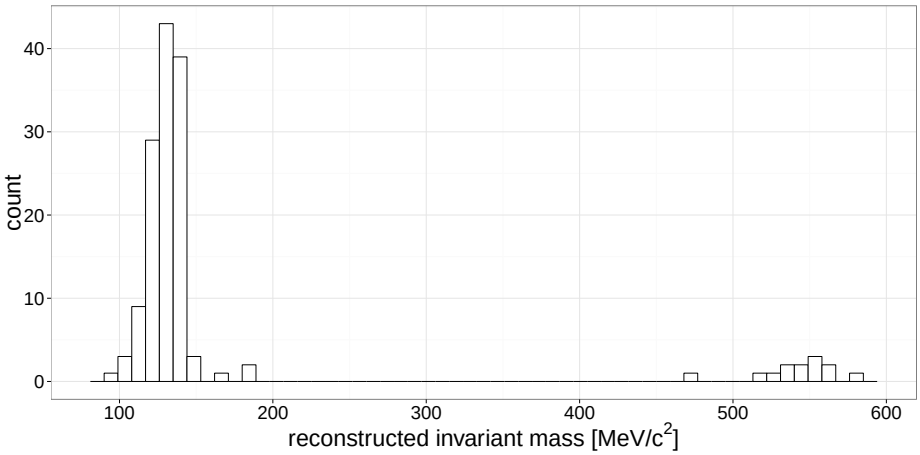

Figure 9.6: Invariant mass distribution for a particles decaying into $\gamma\gamma$.

not only on the tails but on the bulk of the events too (see for example the small kink in M_{nq} qq plot at about -0.3). Therefore, the author of this thesis decided to use M_{shower} as the most accurate estimation of the π^0 mass.

The resulting π^0 invariant mass is 134.5 ± 1.3 MeV/c^2 with $\chi^2 = 108$ (dof=102).

The RMS of the reconstructed π^0 invariant mass was found to be equal to 12.8 ± 0.8 MeV/c^2.

The fit on the η sample is affected by the limited number of 13 events. The resulting invariant mass is equal to 558 ± 23 MeV/c^2.

9.2.3 Systematic errors for reconstructed π^0 invariant mass

The definition of the systematic errors includes several contributions that include the assumptions made in the analysis or the precision of the FLUKA description of the detector.

Non gaussian tails

As discussed earlier the presence of non gaussian tails for the reconstructed π^0 invariant mass is evident from the qq plot for M_{nq} (Figure 9.8). The shower containment correction reduces the distance of

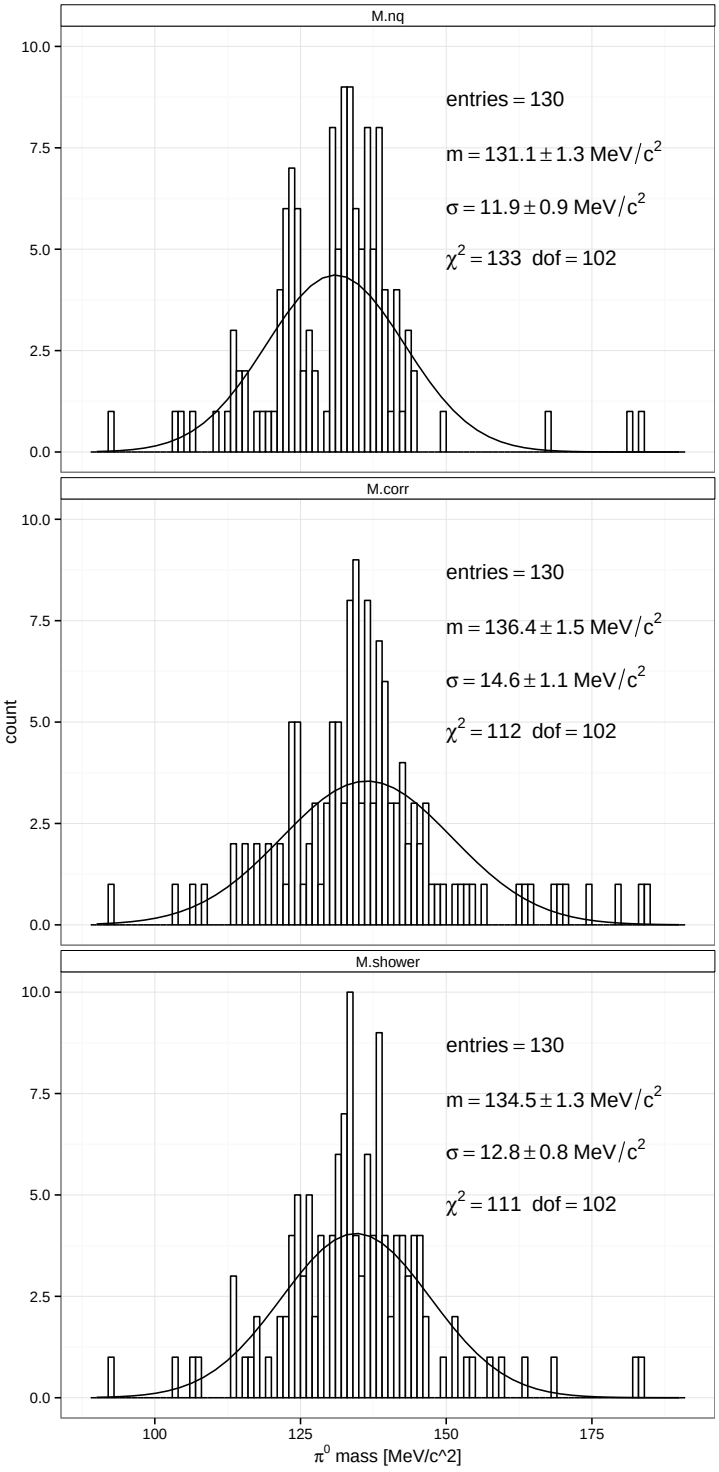

Figure 9.7: Distributions of π^0 mass reconstructed for different containment estimators. $M.x$ where x=nq, corr, shower, is the π^0 mass reconstructed with E_x energy containment corrections.

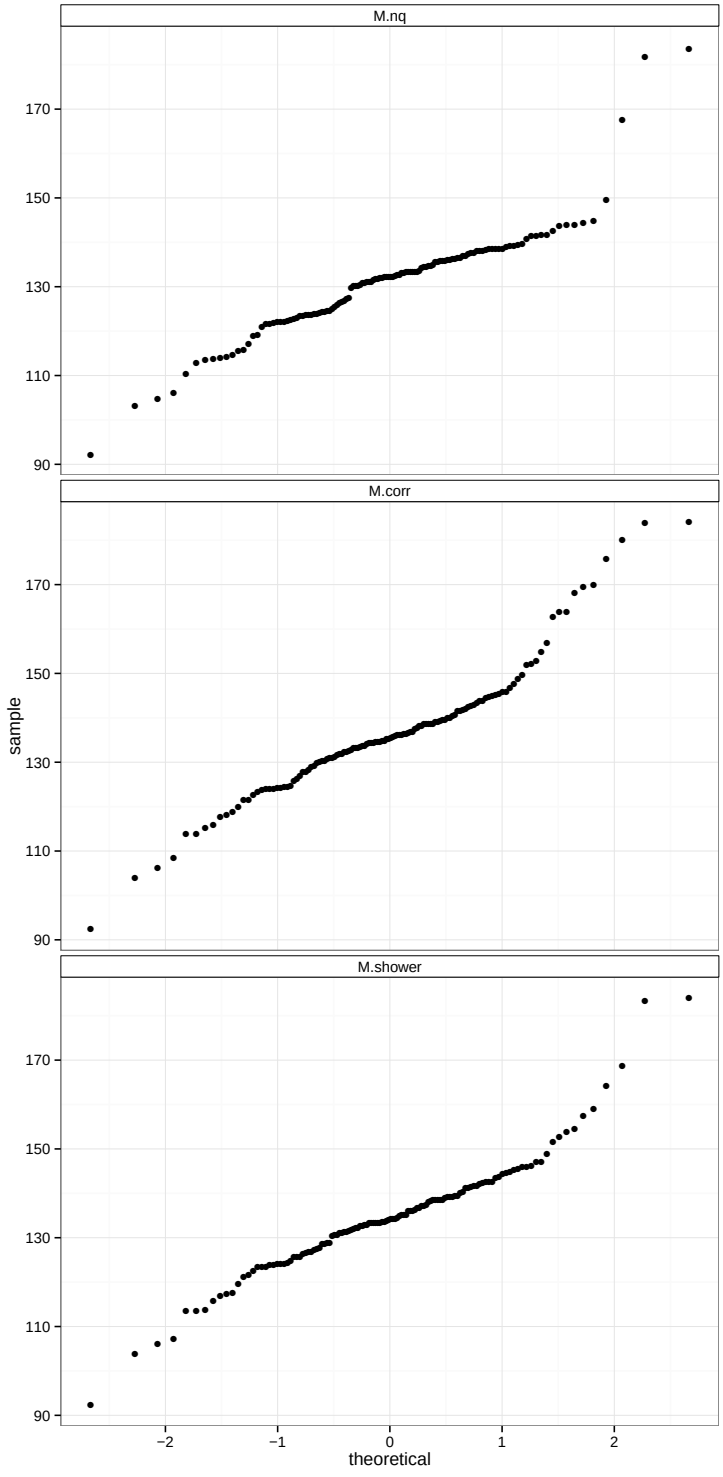

Figure 9.8: Quantile-quantile plot for reconstructed π^0 mass with or without energy correction for shower containment included. *M.x* where x=nq, corr, shower, is the π^0 mass reconstructed with E_x energy containment corrections.

these point from the theoretical quantile, instead of introducing new spread. Considering the events with M_{nq} above 150 MeV/c^2 or below 100 MeV/c^2, the following points are found (masses are in units of MeV/c^2):

M_{nq}	ξ_1	ξ_2	M_{corr}	M_{shower}
183	0.994	0.999	184	184
92	0.996	1.000	92	92
182	0.984	0.992	184	183
167	0.987	0.990	169	169

As it can be seen the containment for these events is very high, resulting in very small corrections. Excluding the four tails events the data are perfectly described by a gaussian distribution with a p-value better than 60%; the best fit for the π^0 invariant mass without these four points is at 133.7 $\pm$ 0.6 MeV/c^2 (where the smaller statistical error is due to the reduced spread of the data, 10 instead of 12 MeV/c^2).

Therefore a systematic uncertainty 0.3 MeV/c^2 (1 σ) is attributed to the deviation of the data from the gaussian model.

Short conversion distances

As discussed earlier (section 9.1.1) the reconstruction of the invariant mass can be strongly biased by the incorrect estimation of the opening angle theta: as shown in chapter 6.2.1 the uncertainty of the opening angle is related to the shortest conversion distance. In Figure 9.9, a plot of the π^0 mass is shown as function of the shortest conversion distance in a subset of the data.

As it can be seen, a dependence on the conversion distance is present: the systematic uncertainty of 1 MeV/c^2 (1 σ) is accounted for this effect.

FLUKA simulation

The biggest source of uncertainty comes from the FLUKA simulation that was used along this thesis to estimate several corrections: among them some are small (like the hit finding term described in section 6.3) and other contribute significantly to the result. In particular the ion recombination corrections accounts for a factor 33% and even small deviations of the simulation code from the detector behavior can introduce significant bias in the results. On the other hand it is not possible to estimate the quality of the FLUKA model for the ion recombination by independent measurement in ICARUS.

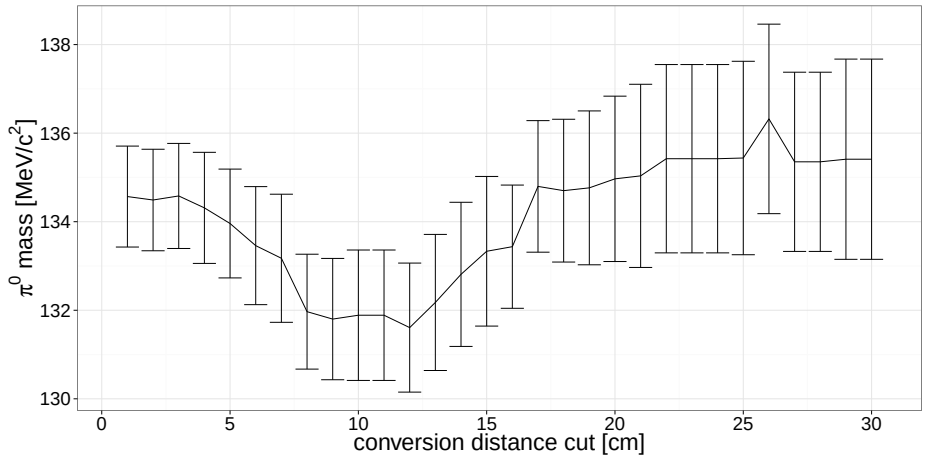

Figure 9.9: Reconstructed π^0 invariant mass as function of the minimal conversion distance: each point represent the mass (and it's standard error) for a subset of data all with conversion distances longer than the value in x axis.

In [4] the collaboration quotes a systematic error of 3% due to the Monte Carlo calibration of the detector; the other contributions from FLUKA are considered negligible.

Considering the systematic terms uncorrelated, the total systematic uncertainty is estimated to be 4.3 MeV/c^2 (1 σ). Therefore the best value for the π^0 mass is:

$$M_{\pi^0} = 134.5 \pm 1.5(stat) \pm 4.2(sys) \ MeV/c^2 \qquad (9.4)$$

9.2.4 Opening Angle

The distribution of reconstructed opening angle θ from $\pi^0 \to \gamma\gamma$ events is plotted in Figure 9.10. The smallest value of the reconstructed angle is 6° and the biggest one 151° with the mean value equal to ∼53°.

In Figure 9.11 a plot of a decaying particle (π^0 or η) momentum versus the opening angle θ is shown. The momentum is defined as

$$p = \sqrt{(E+m)^2 - m^2}, \qquad (9.5)$$

where E is energy of the particle and m its mass. The separation between π^0 and η is clear.

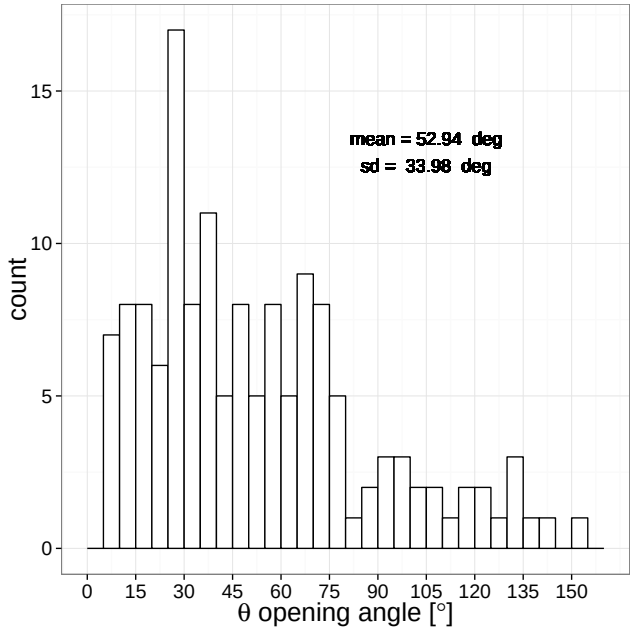

Figure 9.10: Distribution of opening angle θ for reconstructed π^0 events. Values of mean and standard deviation (sd) are indicated.

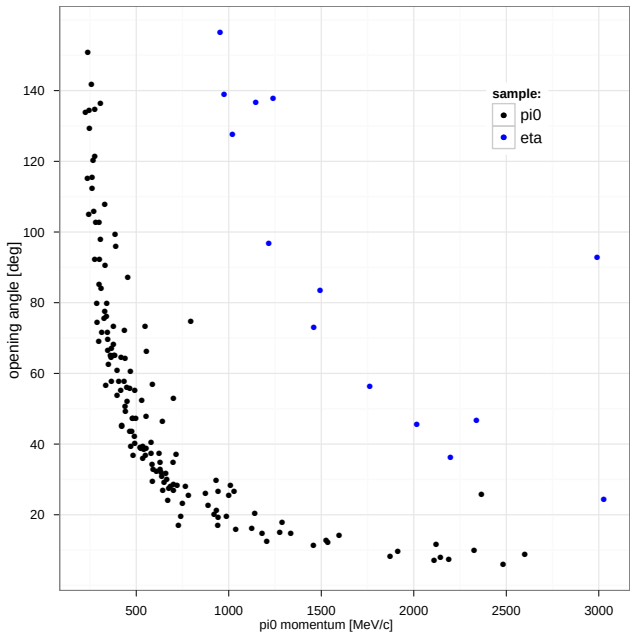

Figure 9.11: Momentum of particle decaying into $\gamma\gamma$ versus opening angle θ

Chapter 10

Summary and conclusions

The goal of this thesis was the precise study of electromagnetic showers in the ICARUS T600 detector. This, in turn, lead to the identification and reconstruction of neutral mesons, like π^0 and η decaying in the fiducial volume. The accurate reconstruction of the mesons invariant mass provides an intrinsic energy calibration for the detector. Moreover, the tagging of π^0 allows to suppress a background to electron identification required in ν_e CC studies.

To calculate the invariant mass of a particle decaying into $\gamma\gamma$, only three quantities are needed: the two photon energies and the opening angle θ between them. The opening angle reconstruction is a result of precise reconstruction of three vertices, corresponding to π^0 decay and the pair production initiated by the γ. It was proven that the position reconstruction accuracy is better than 5 mm (in three dimensions). The corresponding angular resolution depends on the conversion distances of the interacting γ's. The result of a toy Monte Carlo based on the FLUKA simulations indicates that for events with conversion distances greater than 2.5 cm, the opening angle accuracy is better than 3°.

The accurate energy reconstruction of γ's involves different corrections to the collected charge from the electromagnetic showers. While several corrections are already included in the official ICARUS reconstruction software, it was found that some of them are not tuned for electromagnetic showers reconstruction. Moreover, the other corrections absent in the ICARUS software that improve the accuracy of the energy reconstruction of electromagnetic showers were introduced. The extensive studies on the electromagnetic shower profile in LAr based on FLUKA simulations have been performed. As a result, the corrections to the electromagnetic showers contained within the fiducial volume of the detector were applied. The understanding of the shower containment influences the energy reconstruction

of not fully contained γ showers and more accurate measurement of the π^0 invariant mass. As a result of applying all these different corrections, the reconstructed π^0 invariant mass was found to be equal $134.5 \pm 1.5 \pm 4.2$ MeV/c^2.

During the analysis of the γ showers, two other properties were also studied. First, the discrimination between e^-/γ can be provided taking into account the energy loss in the first few centimeters of a shower. For electrons, dE/dx is equal to 2.1 MeV/cm (1 m.i.p.), while for photons it is, in most cases, 2 m.i.p.'s. The extensive studies of dE/dx in first 2.5 cm of the shower, providing to a convincing evidence of e^-/γ discrimination has been performed. This analysis was used for the selection of ν_e CC interactions in a search for sterile neutrinos.

A combined, Monte Carlo and real data, analysis was necessary to understand the distribution of conversion distances found during the manual scanning of ν_μ CC CNGS data. It was found that only for γ's with energies above 400 MeV, the conversion distance approaches the nominal value of 18 cm.

List of Figures

List of Tables

Acknowledgments

I would like to express my gratitude to Professor Jan Kisiel, my research supervisor, for his guidance and useful critiques. I would like to thank the staff of the LNGS for their hospitality. I would also like to extend my thanks to the ICARUS analysis group, coordinated by Paola Sala, for their useful and precious suggestions on the analysis. The completion of this thesis would have not been possible without the support of Maddalena Antonello and Chiara Vignoli.

Finally, I wish to thank my parents and sister for their support and encouragement throughout my study. I am also undoubtedly grateful to my husband, Alessandro, who supported me through this journey.

I also place on record, my sense of gratitude to one and all, who directly or indirectly, contribute in this venture.

Bibliography

[1] F. Reines and C. Cowan, *Detection of the free neutrino*, Phys.Rev. **92** (1953) 830.

[2] G. Danby et al., *Observation of High-Energy Neutrino Reactions and the Existence of Two Kinds of Neutrinos*, Phys.Rev.Lett. **9** (1962) 36.

[3] K. Kodama et al., *Observation of tau neutrino interactions*, DONUT, Phys.Lett. **B504** (2001) 218, hep-ex/0012035.

[4] A. Ankowski et al., *Energy reconstruction of electromagnetic showers from $\pi 0$ decays with the ICARUS T600 Liquid Argon TPC*, ICARUS Collaboration, Acta Phys.Polon. **B41** (2010) 103, 0812.2373.

[5] M. Antonello et al., *A Proposal for a Three Detector Short-Baseline Neutrino Oscillation Program in the Fermilab Booster Neutrino Beam*, MicroBooNE, LAr1-ND, ICARUS-WA104, (2015), 1503.01520.

[6] M. Antonello et al., *Experimental search for the "LSND anomaly" with the ICARUS detector in the CNGS neutrino beam*, Eur.Phys.J. **C73** (2013) 2345, 1209.0122.

[7] M. Antonello et al., *Search for anomalies in the ν_e appearance from a ν_μ beam*, ICARUS, Eur.Phys.J. **C73** (2013) 2599, 1307.4699.

[8] C. Rubbia, *The Liquid Argon Time Projection Chamber: A New Concept for Neutrino Detectors*, (1977).

[9] S. Amerio et al., *Design, construction and tests of the ICARUS T600 detector*, ICARUS Collaboration, Nucl.Instrum.Meth. **A527** (2004) 329.

[10] C. Rubbia et al., *Underground operation of the ICARUS T600 LAr-TPC: first results*, JINST **6** (2011) P07011, 1106.0975.

[11] S. Amoruso et al., *Analysis of the liquid argon purity in the ICARUS T600 TPC*, Nucl.Instrum.Meth. **A516** (2004) 68.

[12] M. Antonello et al., *Operation and performance of the ICARUS-T600 cryogenic plant at Gran Sasso underground Laboratory*, (2015), 1504.01556.

[13] M. Antonello et al., *Experimental observation of an extremely high electron lifetime with the ICARUS-T600 LAr-TPC*, JINST **9** (2014) P12006, 1409.5592.

[14] M. Dracos, *Neutrinos from CERN to Gran Sasso: The CNGS project*, J.Phys.Conf.Ser. **203** (2010) 012013.

[15] M. Antonello et al., *The trigger system of the ICARUS experiment for the CNGS beam*, Journal of Instrumentation **9** (2014) P08003.

[16] B. Pontecorvo, *Mesonium and anti-mesonium*, Sov.Phys.JETP **6** (1957) 429.

[17] Z. Maki, M. Nakagawa and S. Sakata, *Remarks on the unified model of elementary particles*, Prog.Theor.Phys. **28** (1962) 870.

[18] K. Olive et al., *Review of Particle Physics*, Particle Data Group, Chin.Phys. **C38** (2014) 090001.

[19] N. Agafonova et al., *The detection of neutrino interactions in the emulsion/lead target of the OPERA experiment*, OPERA, JINST **4** (2009) P06020, 0903.2973.

[20] O. Sato, *Observation of a first ν_τ candidate event in the OPERA experiment in the CNGS beam*, OPERA Collaboration, Nucl.Phys.Proc.Suppl. **229-232** (2012) 38.

[21] N. Agafonova et al., *New results on $\nu_\mu \to \nu_\tau$ appearance with the OPERA experiment in the CNGS beam*, OPERA Collaboration, JHEP **1311** (2013) 036, 1308.2553.

[22] N. Agafonova et al., *Evidence for $\nu_\mu \to \nu_\tau$ appearance in the CNGS neutrino beam with the OPERA experiment*, OPERA Collaboration, Phys.Rev. **D89** (2014) 051102, 1401.2079.

[23] N. Agafonova et al., *Observation of ν_τ appearance in the CNGS beam with the OPERA experiment*, OPERA Collaboration, (2014), 1407.3513.

[24] A. Aguilar-Arevalo et al., *Evidence for neutrino oscillations from the observation of anti-neutrino(electron) appearance in a anti-neutrino(muon) beam*, LSND, Phys.Rev. **D64** (2001) 112007, hep-ex/0104049.

[25] A. Aguilar-Arevalo et al., *Improved Search for* $\bar{\nu}_\mu \to \bar{\nu}_e$ *Oscillations in the MiniBooNE Experiment*, MiniBooNE, Phys.Rev.Lett. **110** (2013) 161801, 1207.4809.

[26] Y. Fukuda et al., *Evidence for oscillation of atmospheric neutrinos*, Super-Kamiokande, Phys.Rev.Lett. **81** (1998) 1562, hep-ex/9807003.

[27] G. Battistoni et al., *Atmospheric neutrinos in a large Liquid Argon detector*, ICARUS, Technical Note **06-01** (2006).

[28] T. Adam et al., *Measurement of the neutrino velocity with the OPERA detector in the CNGS beam*, OPERA, JHEP **1210** (2012) 093, 1109.4897.

[29] A.G. Cohen and S.L. Glashow, *Pair Creation Constrains Superluminal Neutrino Propagation*, Phys.Rev.Lett. **107** (2011) 181803, 1109.6562.

[30] M. Antonello et al., *A Search for the analogue to Cherenkov radiation by high energy neutrinos at superluminal speeds in ICARUS*, ICARUS Collaboration, Phys.Lett. **B711** (2012) 270, 1110.3763.

[31] M. Antonello et al., *Measurement of the neutrino velocity with the ICARUS detector at the CNGS beam*, ICARUS Collaboration, Phys.Lett. **B713** (2012) 17, 1203.3433.

[32] M. Antonello et al., *Precision measurement of the neutrino velocity with the ICARUS detector in the CNGS beam*, JHEP **1211** (2012) 049, 1208.2629.

[33] F. Arneodo et al., *The ICARUS experiment: A Second generation proton decay experiment and neutrino observatory at the Gran Sasso Laboratory*, ICARUS collaboration, (2001), hep-ex/0103008.

[34] K.S. Hirata et al., *Experimental limits on nucleon lifetime for lepton + meson decay modes*, Kamiokande, Phys. Lett. **B220** (1989) 308.

[35] K. Hirata et al., *Observation in the Kamiokande-II Detector of the Neutrino Burst from Supernova SN 1987a*, Phys.Rev. **D38** (1988) 448.

[36] K. Hirata et al., *Observation of a neutrino burst from the supernova SN1987a*, Kamiokande, Phys. Rev. Lett. **58** (1987) 1490.

[37] R. Bionta et al., *Observation of a Neutrino Burst in Coincidence with Supernova SN 1987a in the Large Magellanic Cloud*, Phys.Rev.Lett. **58** (1987) 1494.

[38] A. Chudakov, Y. Elensky and S. Mikheev, *Characteristics of the Neutrino Emission From Supernova SN1987A*, JETP Lett. **46** (1987) 373.

[39] W. Leo, Techniques for Nuclear and Particle Physics Experiments: A How to Approach (Springer-Verlag, 1993).

[40] G. Knoll, Radiation Detection and Measurement (Wiley, 2000).

[41] H. Bethe, *Zur Theorie des Durchgangs schneller Korpuskularstrahlen durch Materie*, Annalen der Physik **397** (1930) 325.

[42] J. Beringer et al., *Review of Particle Physics*, Particle Data Group, Phys. Rev. D **86** (2012) 010001.

[43] E. Longo and I. Sestili, *Monte Carlo Calculation of Photon Initiated Electromagnetic Showers in Lead Glass*, Nucl.Instrum.Meth. **128** (1975) 283.

[44] M. Antonello et al., *Precise 3D track reconstruction algorithm for the ICARUS T600 liquid argon time projection chamber detector*, Adv.High Energy Phys. **2013** (2013) 260820, 1210.5089.

[45] A.K. Balazs, Kegl, T. Linder and K. Zeger, *Learning and Design of Principal Curves*, IEEE Transactions on Pattern Analysis and Machine Intelligence **22** (2000) 281.

[46] A. Ferrari et al., *FLUKA: A multi-particle transport code (Program version 2005)*, (2005).

[47] T. Bohlen et al., *The FLUKA Code: Developments and Challenges for High Energy and Medical Applications*, Nuclear Data Sheets **120** (2014) 211 .

[48] J. Birks, The Theory and Practice of Scintillation Counting (Pergamon Press, Oxford, 1964).

[49] S. Amoruso et al., *Study of electron recombination in liquid argon with the ICARUS TPC*, ICARUS, Nucl.Instrum.Meth. **A523** (2004) 275.

[50] F. Cavanna et al., *LArIAT: Liquid Argon In A Testbeam*, LArIAT, (2014), 1406.5560.

[51] W.H. Press et al., Numerical Recipes 3rd Edition: The Art of Scientific Computing, 3 ed. (Cambridge University Press, New York, NY, USA, 2007).

[52] A.R. Y. Ge, P. Sala, e^-/π^0 *Separation in ICARUS Liquid Argon Time Projection Chamber*, ICARUS, Technical Note **03-05** (2003).

[53] R. Brunetti et al., *Detection and reconstruction of* π^0 *mesons with the ICARUS T600 liquid argon TPC*, ICARUS, Technical Note **07-01** (2007).

[54] G. Battistoni et al., *ICARUS T600: Preliminary analysis of cosmic ray induced interactions with* π^0 *and* η^0 *production*, ICARUS, Technical Note **04-14** (2004).